Lagrange multiplier based vs micromorphic gradient-enhanced rate-(in)dependent crystal plasticity modelling and simulation

Jean-Michel Scherer, Vikram Phalke, Jacques Besson, Samuel Forest, Jeremy Hure, Benoît Tanguy

Lagrange multiplier based vs micromorphic gradient-enhanced rate-(in)dependent crystal plasticity modeling and simulation

Jean-Michel Scherer[a,b,*], Vikram Phalke[b], Jacques Besson[b], Samuel Forest[b], Jeremy Hure[a], Benoît Tanguy[a]

[a] *Université Paris-Saclay, CEA, Service d'Etude des Matériaux Irradiés, 91191, Gif-sur-Yvette, France*
[b] *MINES ParisTech, PSL University, MAT – Centre des matériaux, CNRS UMR 7633, BP 87 91003 Evry, France*

Abstract

A reduced strain gradient crystal plasticity theory which involves the gradient of a single scalar field is presented. Rate-dependent and rate-independent crystal plasticity settings are considered. The theory is then reformulated following first the micromorphic approach and second a Lagrange multiplier approach. The finite element implementation of the latter is detailed. Computational efficiency of the Lagrange multiplier approach is highlighted in an example involving regularization of strain localization. The numerical performance improvement is shown to reach up to two orders of magnitude in computation time speedup. Then, size effects predicted by micromorphic and Lagrange multiplier based formulations of strain gradient plasticity are assessed. First of all numerical comparisons are performed on single crystal wires in torsion. Saturation of the size effects induced by the micromorphic approach and absence of saturation with the Lagrange multiplier approach when sample size is decreased are demonstrated. The Lagrange multiplier based formulation is finally applied to characterize size effects predicted for the ductile growth of porous unit-cells at imposed stress triaxiality. Excellent agreement with micromorphic results is obtained.

Keywords: Strain gradient plasticity, Micromorphic approach, Lagrange multiplier approach, Crystal plasticity, Finite elements

1. Introduction

The anisotropic elasto-plastic deformation of crystalline aggregates including shape change, crystallographic texture, and strain hardening can be predicted by classical continuum crystal plasticity (Cailletaud et al., 2003; Roters et al., 2010). The classical continuum crystal plasticity formulation can be enhanced in order to predict experimentally observed size effects such as precipitate or grain size effects, for instance based on the introduction of the dislocation density tensor and associated constitutive length scales (Fleck and Hutchinson, 1997; Forest, 1998; Gurtin, 2000).

Experimental evidence of size effects can be found in different mechanical tests such as micro-torsion (Fleck and Hutchinson, 1997; Gao and Huang, 2001; Liu et al., 2012; Guo et al., 2017), micro-compression (Uchic et al., 2004; Greer et al., 2005), micro-bending (Stölken and Evans, 1998; Gao and

*Corresponding author.
Email address: jean-michel.scherer@mines-paristech.fr (Jean-Michel Scherer)

Huang, 2001; Haque and Saif, 2003) and micro-indentation (Nix and Gao, 1998; Gao and Huang, 2001; Liu and Ngan, 2001) of crystalline materials. Size–dependent crystal plasticity modeling is required when the specimen or grain size becomes comparable to the intrinsic lengths of the underlying plastic deformation mechanisms (Fleck and Hutchinson, 1997; Kocks and Mecking, 2003). The gradient of shear strain results in the development of the dislocation density tensor which can be described in terms of the storage of geometrically necessary dislocations (GND) (Ashby, 1970; Acharya and Bassani, 2000; Gurtin, 2002; Bardella, 2006; Cordero et al., 2012a). The GND density controls the material strain hardening together with the usual scalar dislocation densities, also called statistically stored dislocations (SSD).

The strain gradient plasticity approach can also be used to regularize the simulation of shear band formation in crystalline solids. Strain softening results in a narrow band of intense shearing. The possible loss of ellipticity of partial differential equations in strain softening materials results in an ill-posed boundary value problem and classically shows dependency on mesh size or density. The shear band dependency on the mesh size or density can be overcome by introducing intrinsic material length scale in conventional plasticity (Needleman, 1988; Voyiadjis and Al-Rub, 2005; Anand et al., 2012; Peerlings et al., 2002; Vignjevic et al., 2018; Kaiser and Menzel, 2019b) and in crystal plasticity (Petryk and Stupkiewicz, 2016; Ling et al., 2018; Kaiser and Menzel, 2019a). Furthermore, the difficulties in assessment of active slip systems within the crystal plasticity framework can be overcome by rate-dependent (Busso and Cailletaud, 2005) or rate-independent (Forest and Rubin, 2016; Kaiser and Menzel, 2019a) formulations.

Implementation of strain gradient crystal plasticity in a finite element code is a challenging task that has been performed for example by Shu (1998); Borg et al. (2008a); Yalcinkaya et al. (2012); Bardella et al. (2013); Nellemann et al. (2017, 2018); Panteghini and Bardella (2016) at small strains and by Niordson and Kysar (2014); Lewandowski and Stupkiewicz (2018); Ling et al. (2018); Kaiser and Menzel (2019a) at finite deformations. An efficient method to implement strain gradient plasticity models is to resort to the micromorphic approach proposed by Forest (2009) at small strains and Forest (2016) at finite deformation, as demonstrated by Anand et al. (2012); Brepols et al. (2017) for conventional plasticity and by Cordero et al. (2010); Aslan et al. (2011); Ryś et al. (2020) for crystal plasticity based on the dislocation density tensor. According to this approach, additional plastic microdeformation degrees of freedom, in the sense of Eringen and Suhubi (1964), are introduced at each node and the curl part of the microdeformation tensor is assumed to expend work with a conjugate couple stress tensor. A penalty parameter, which can be interpreted as a higher order elasticity modulus, is used to constrain the plastic microdeformation to be as close as possible to the usual plastic deformation. As a consequence, the curl of the microdeformation tensor almost coincides with the dislocation density tensor.

The computational cost of finite element simulation based on strain gradient or micromorphic crystal plasticity is rather high due to the number of additional degrees of freedom and the strong nonlinearities of the problem. A reduced micromorphic crystal plasticity model was proposed by

(Wulfinghoff and Böhlke, 2012; Wulfinghoff et al., 2013; Erdle and Böhlke, 2017; Ling et al., 2018; Scherer et al., 2019). It is limited to a single scalar additional degree of freedom, called microslip variable which is bounded to remain close to the cumulative plastic slip by means of the penalty parameter. The gradient of the microslip is then assumed to be an argument of the Helmholtz free energy density function. This approach can be compared to the relaxation of the strain gradient plasticity model by a Lagrange multiplier based formulation recently proposed by (Zhang et al., 2018) for isotropic materials. As in the micromorphic approach, one hardening variable is duplicated in two separate instances. One instance of the variable is dedicated to nonlocality and the other to nonlinearity, see (Zhang et al., 2018). The equivalence between both variables is weakly enforced by a Lagrange multiplier, instead of a penalty term. The Lagrange term is added to the free energy function and treated as an additional field variable. This strong coupling scheme was shown to reduce the computational cost drastically compared to previous algorithms. Details of finite element implementation of micromorphic strain gradient rate-dependent crystal plasticity based on Newton-Raphson method to integrate the differential equations can be found in (Ling et al., 2018). The numerical implementation of a Lagrange multiplier based strain gradient isotropic plasticity model was presented in (Zhang et al., 2018).

The objective of the present work is to compare the computational performance and predictions of reduced micromorphic crystal plasticity and a new Lagrange multiplier based implementation of strain gradient plasticity. The novelty of the work lies, first, in this new formulation of strain gradient plasticity with a Lagrangian function and, second, in the comparison of the predictions of the two models. The computational performance and physical relevance of both models are also assessed. Three distinct physical situations are considered. First, regularization of strain localization in a periodic bar undergoing strain-softening is investigated. Then, the size and orientation dependent torsion of FCC single crystal wires is investigated showing that both models coincide at intermediate wire diameters but differ in their asymptotic behaviour. Further, the numerically efficient Lagrange multiplier based constitutive framework is used to study the ductile growth and coalescence of voids in porous unit-cells. The results are compared to data obtained with the micromorphic approach that are already available in the literature.

The outline of the paper is as follows. In section 2, a thermodynamically consistent formulation of reduced strain gradient crystal plasticity is presented in the rate-dependent and rate-independent cases. In section 3 the constitutive framework of reduced micromorphic and Lagrange multiplier approaches are described. The numerical implementation of the latter is presented in section 4. Numerical examples of a sheared periodic bar, a cylinder in torsion and a porous unit-cell under axisymmetric triaxial loading are provided in section 5. Concluding remarks follow in section 6.

The notations used in the paper are as follows. Underlined bold $\underline{\boldsymbol{a}}$ and under-wave bold $\underset{\sim}{\boldsymbol{A}}$ stand respectively for first and second rank tensors. The transpose, inverse, transpose of inverse and time derivative are denoted by $\underset{\sim}{\boldsymbol{A}}^T$, $\underset{\sim}{\boldsymbol{A}}^{-1}$, $\underset{\sim}{\boldsymbol{A}}^{-T}$ and $\dot{\underset{\sim}{\boldsymbol{A}}}$ respectively. The single and double contractions are written as $\underset{\sim}{\boldsymbol{A}}.\underline{\boldsymbol{b}} = A_{ij}b_j\underline{\boldsymbol{e}}_i$ and $\underset{\approx}{\boldsymbol{A}} : \underset{\sim}{\boldsymbol{B}} = A_{ijkl}B_{kl}\underline{\boldsymbol{e}}_i \otimes \underline{\boldsymbol{e}}_j$ respectively. The following tensor products

are used: $\underline{\boldsymbol{a}} \otimes \underline{\boldsymbol{b}} = a_i b_j \underline{\boldsymbol{e}}_i \otimes \underline{\boldsymbol{e}}_j$, $\underset{\sim}{\boldsymbol{A}} \otimes \underset{\sim}{\boldsymbol{B}} = A_{ij} B_{kl} \underline{\boldsymbol{e}}_i \otimes \underline{\boldsymbol{e}}_j \otimes \underline{\boldsymbol{e}}_k \otimes \underline{\boldsymbol{e}}_l$, $\underset{\sim}{\boldsymbol{A}} \underline{\otimes} \underset{\sim}{\boldsymbol{B}} = A_{ik} B_{jl} \underline{\boldsymbol{e}}_i \otimes \underline{\boldsymbol{e}}_j \otimes \underline{\boldsymbol{e}}_k \otimes \underline{\boldsymbol{e}}_l$ and $\underset{\sim}{\boldsymbol{A}} \overline{\otimes} \underset{\sim}{\boldsymbol{B}} = A_{il} B_{jk} \underline{\boldsymbol{e}}_i \otimes \underline{\boldsymbol{e}}_j \otimes \underline{\boldsymbol{e}}_k \otimes \underline{\boldsymbol{e}}_l$, where $\underline{\boldsymbol{e}}_i$ refers to an orthonormal base vector.

2. A reduced strain gradient crystal plasticity theory

2.1. Thermodynamical formulation

A reduced strain gradient crystal plasticity theory is adopted in which only the gradient of a scalar effective quantity is considered in keeping with (Aifantis, 1984). Based on the work by Wulfinghoff and Böhlke (2012) the cumulated plastic slip γ_{cum}, defined as

$$\gamma_{cum} = \int_0^t \sum_{s=1}^{N} |\dot{\gamma}^s| \, \mathrm{d}t \tag{1}$$

is chosen to be the thermodynamic variable carrying gradient effects. $\dot{\gamma}^s$ denotes the plastic slip rate on the $s-$th slip system. In the finite strain setting, the deformation gradient $\underset{\sim}{\boldsymbol{F}}$, with components $F_{ij} = \partial x_i / \partial X_j$, is multiplicatively split into an elastic part $\underset{\sim}{\boldsymbol{E}}$ and a plastic part $\underset{\sim}{\boldsymbol{P}}$ such that $\underset{\sim}{\boldsymbol{F}} = \underset{\sim}{\boldsymbol{E}}.\underset{\sim}{\boldsymbol{P}}$. The plastic velocity gradient $\underset{\sim}{\boldsymbol{L}}^p$ is related to the slip rates on each slip system by

$$\underset{\sim}{\boldsymbol{L}}^p = \dot{\underset{\sim}{\boldsymbol{P}}}.\underset{\sim}{\boldsymbol{P}}^{-1} = \sum_{s=1}^{N} \dot{\gamma}^s (\underline{\boldsymbol{m}}^s \otimes \underline{\boldsymbol{n}}^s) \quad \text{with} \quad \underset{\sim}{\boldsymbol{L}} = \dot{\underset{\sim}{\boldsymbol{F}}}.\underset{\sim}{\boldsymbol{F}}^{-1} = \dot{\underset{\sim}{\boldsymbol{E}}}.\underset{\sim}{\boldsymbol{E}}^{-1} + \underset{\sim}{\boldsymbol{E}}.\underset{\sim}{\boldsymbol{L}}^p.\underset{\sim}{\boldsymbol{E}}^{-1} \tag{2}$$

where $\underline{\boldsymbol{m}}^s$ and $\underline{\boldsymbol{n}}^s$ refer to the gliding direction and direction normal to the slip plane respectively. In the reference configuration, upon neglecting body forces, following (Fleck and Hutchinson, 1997; Gurtin and Anand, 2009) the principle of virtual power, for all material subsets D_0 of the body, can be written as

$$\int_{D_0} \left(\underset{\sim}{\boldsymbol{S}} : \dot{\underset{\sim}{\boldsymbol{F}}} + S \dot{\gamma}_{cum} + \underline{\boldsymbol{M}} . \dot{\underline{\boldsymbol{K}}} \right) \mathrm{d}V_0 = \int_{\partial D_0} (\underline{\boldsymbol{T}} . \dot{\underline{\boldsymbol{u}}} + M \dot{\gamma}_{cum}) \, \mathrm{d}S_0 \qquad \forall \dot{\underline{\boldsymbol{u}}}, \quad \forall \dot{\gamma}_{cum}, \quad \forall D_0 \tag{3}$$

where $\underset{\sim}{\boldsymbol{S}}$ is the Boussinesq (or nominal 1-st Piola-Kirchhoff) stress tensor related to the Cauchy stress tensor $\underset{\sim}{\boldsymbol{\sigma}}$ by $\underset{\sim}{\boldsymbol{S}} = (\rho_0/\rho) \underset{\sim}{\boldsymbol{\sigma}}.\underset{\sim}{\boldsymbol{F}}^{-T}$ with ρ_0 (respect. ρ) the volumetric mass density in the reference configuration (respect. current configuration). Vector $\underline{\boldsymbol{T}}$ is the traction vector and $\dot{\underline{\boldsymbol{u}}}$ is an arbitrary velocity field. S and $\underline{\boldsymbol{M}}$ are higher order stresses and M a higher order traction scalar. $\underline{\boldsymbol{K}}$ is the Lagrangian gradient of the cumulated plastic slip, $\underline{\boldsymbol{K}} = \mathrm{Grad}\, \gamma_{cum}$. From Eq. (3) it can be derived that, within any subset D_0 of the body, the stresses satisfy the equilibrium relations

$$\mathrm{Div}\, \underset{\sim}{\boldsymbol{S}} = \underline{\boldsymbol{0}} \quad \forall \underline{\boldsymbol{X}} \in D_0 \tag{4}$$

$$\mathrm{Div}\, \underline{\boldsymbol{M}} - S = 0 \quad \forall \underline{\boldsymbol{X}} \in D_0 \tag{5}$$

in the absence of body forces and in the static case. As a result of Eq. (3), on the surface of the subset ∂D_0 the stresses $\underset{\sim}{\boldsymbol{S}}$ and $\underline{\boldsymbol{M}}$ are in equilibrium with the traction vector $\underline{\boldsymbol{T}}$ and scalar M according to

$$\underline{\boldsymbol{T}} = \underset{\sim}{\boldsymbol{S}}.\underline{\boldsymbol{n}}_0 \quad \forall \underline{\boldsymbol{X}} \in \partial D_0, \tag{6}$$

$$M = \underline{\boldsymbol{M}} . \underline{\boldsymbol{n}}_0 \quad \forall \underline{\boldsymbol{X}} \in \partial D_0 \tag{7}$$

where $\underline{\boldsymbol{n}}_0$ refers to the outward unit surface normal. In order to formulate a complete thermodynamic theory of reduced strain gradient crystal plasticity a free energy potential ψ needs to be defined. The specific free energy potential ψ is chosen to depend on the elastic Green-Lagrange strain measure $\underset{\sim}{\boldsymbol{E}}^e_{GL} = (1/2)\left(\underset{\sim}{\boldsymbol{E}}^T.\underset{\sim}{\boldsymbol{E}} - \underset{\sim}{\mathbf{1}}\right)$, the cumulated plastic slip γ_{cum}, its Lagrangian gradient $\underline{\boldsymbol{K}}$ and hardening variables r^s left to be defined.

$$\psi\left(\underset{\sim}{\boldsymbol{E}}^e_{GL}, \gamma_{cum}, r^s, \underline{\boldsymbol{K}}\right) = \frac{1}{2\rho_\sharp}\underset{\sim}{\boldsymbol{E}}^e_{GL} : \underset{\approx}{\boldsymbol{C}} : \underset{\sim}{\boldsymbol{E}}^e_{GL} + \psi_h(r^s, \gamma_{cum}) + \frac{A}{2\rho_0}\underline{\boldsymbol{K}}.\underline{\boldsymbol{K}} \tag{8}$$

where $\rho_\sharp$ refers to the volumetric mass density in the intermediate configuration (*i.e.* the configuration resulting from the transport of the reference configuration by $\underset{\sim}{\boldsymbol{P}}$). The contribution of the cumulated plastic slip gradient is weighed by the strictly positive material parameter, so called higher order modulus, A. The Clausius-Duhem inequality (isothermal case) resulting from 1-st and 2-nd principles of thermodynamics enforces

$$\frac{\underset{\sim}{\boldsymbol{S}}}{\rho_0} : \dot{\underset{\sim}{\boldsymbol{F}}} + \frac{S}{\rho_0}\dot{\gamma}_{cum} + \frac{\underline{\boldsymbol{M}}}{\rho_0}.\dot{\underline{\boldsymbol{K}}} - \dot{\psi} \geq 0 \tag{9}$$

The first term on left-hand side of Eq. (9) can be decomposed into an elastic contribution and a plastic contribution

$$\frac{\underset{\sim}{\boldsymbol{S}}}{\rho_0} : \dot{\underset{\sim}{\boldsymbol{F}}} = \frac{\underset{\sim}{\boldsymbol{\Pi}}^e}{\rho_\sharp} : \dot{\underset{\sim}{\boldsymbol{E}}}^e_{GL} + \frac{\underset{\sim}{\boldsymbol{\Pi}}^M}{\rho_\sharp} : \left(\dot{\underset{\sim}{\boldsymbol{P}}}.\underset{\sim}{\boldsymbol{P}}^{-1}\right) \tag{10}$$

where $\underset{\sim}{\boldsymbol{\Pi}}^e$ is the second Piola-Kirchhoff stress tensor defined by $\underset{\sim}{\boldsymbol{\Pi}}^e = (\rho_\sharp/\rho)\underset{\sim}{\boldsymbol{E}}^{-1}.\underset{\sim}{\boldsymbol{\sigma}}.\underset{\sim}{\boldsymbol{E}}^{-T} = (\rho_\sharp/\rho_0)\underset{\sim}{\boldsymbol{E}}^{-1}.\underset{\sim}{\boldsymbol{S}}.\underset{\sim}{\boldsymbol{P}}^T$ with respect to the intermediate configuration and $\underset{\sim}{\boldsymbol{\Pi}}^M$ is the Mandel stress tensor defined by $\underset{\sim}{\boldsymbol{\Pi}}^M = \underset{\sim}{\boldsymbol{E}}^T.\underset{\sim}{\boldsymbol{E}}.\underset{\sim}{\boldsymbol{\Pi}}^e$. The residual dissipation in Eq. (9) then writes

$$\begin{aligned}\left(\frac{\underset{\sim}{\boldsymbol{\Pi}}^e}{\rho_\sharp} - \frac{\partial\psi}{\partial\underset{\sim}{\boldsymbol{E}}^e_{GL}}\right) : \dot{\underset{\sim}{\boldsymbol{E}}}^e_{GL} + \frac{\underset{\sim}{\boldsymbol{\Pi}}^M}{\rho_\sharp} : \left(\dot{\underset{\sim}{\boldsymbol{P}}}.\underset{\sim}{\boldsymbol{P}}^{-1}\right) + \left(\frac{S}{\rho_0} - \frac{\partial\psi_h}{\partial\gamma_{cum}}\right)\dot{\gamma}_{cum} \\ + \left(\frac{\underline{\boldsymbol{M}}}{\rho_0} - \frac{A}{\rho_0}\underline{\boldsymbol{K}}\right).\dot{\underline{\boldsymbol{K}}} - \sum_{s=1}^{N}\frac{\partial\psi_h}{\partial r^s}\dot{r}^s \geq 0\end{aligned} \tag{11}$$

Here we assume that the higher order stress S has a dissipative part which will be denoted $-\overline{H}$, while $\underline{\boldsymbol{M}}$ is assumed to be non-dissipative. As discussed by Forest and Bertram (2011) it is the most simple assumption to derive Aifantis' model. We then postulate the state laws

$$\underset{\sim}{\boldsymbol{\Pi}}^e = \rho_\sharp\frac{\partial\psi}{\partial\underset{\sim}{\boldsymbol{E}}^e_{GL}} = \underset{\approx}{\boldsymbol{C}} : \underset{\sim}{\boldsymbol{E}}^e_{GL} \tag{12}$$

$$S = \rho_0\frac{\partial\psi_h}{\partial\gamma_{cum}} - \overline{H} \tag{13}$$

$$\underline{\boldsymbol{M}} = \rho_0\frac{\partial\psi}{\partial\underline{\boldsymbol{K}}} = A\underline{\boldsymbol{K}} \tag{14}$$

Finally the residual dissipation reduces to

$$\frac{\underset{\sim}{\boldsymbol{\Pi}}^M}{\rho_\sharp} : \left(\dot{\underset{\sim}{\boldsymbol{P}}}.\underset{\sim}{\boldsymbol{P}}^{-1}\right) - \frac{\overline{H}}{\rho_0}\dot{\gamma}_{cum} - \sum_{s=1}^{N}\frac{\partial\psi_h}{\partial r^s}\dot{r}^s \geq 0 \tag{15}$$

The resolved shear stress τ^s is the energetic counterpart of $\dot{\gamma}^s$ and from Eq. (2) it can be deduced that it is related to Mandel stress $\underset{\sim}{\boldsymbol{\Pi}}^M$ by $\tau^s = \underset{\sim}{\boldsymbol{\Pi}}^M : \underset{\sim}{\boldsymbol{N}}^s$ where $\underset{\sim}{\boldsymbol{N}}^s = \underline{\boldsymbol{m}}^s \otimes \underline{\boldsymbol{n}}^s$ is the Schmid tensor.

Assuming that the rate of hardening variable r^s is proportional to the slip rate $\dot{\gamma}^s$ (e.g. $\dot{r}^s = g_s(r_s)|\dot{\gamma}^s|$) leads to the following expression of the residual dissipation

$$\sum_{s=1}^{N} \left[|\tau^s| - \frac{\rho_\sharp}{\rho_0} \overline{H} - \rho_\sharp \frac{\partial \psi_h}{\partial r^s} g_s(r_s) \right] |\dot{\gamma}^s| \geq 0 \tag{16}$$

where it has been assumed that sign $(\tau^s) =$ sign $(\dot{\gamma}^s)$. Eq. (16) motivates the introduction of the yield function of each system defined by

$$f^s = |\tau^s| - \left(\tau_0^s + \frac{\rho_\sharp}{\rho_0} \overline{H} + \rho_\sharp \frac{\partial \psi_h}{\partial r^s} g_s(r_s) \right) = |\tau^s| - \left(\tau_c^s - \frac{\rho_\sharp}{\rho_0} S \right) \tag{17}$$

where τ_0^s is the initial critical resolved shear stress of s-th system. We here introduce the critical resolved shear stress $\tau_c^s = \tau_0^s + \rho_\sharp \partial \psi_h / \partial r^s g_s(r_s) + \rho_\sharp \partial \psi_h / \partial \gamma_{cum}$. By combining Eq. (5) and Eq. (14) one obtains

$$S = \text{Div}\, \underline{\boldsymbol{M}} = \text{Div}\, (A \underline{\boldsymbol{K}}) \tag{18}$$

As it can be seen from yield criterion Eq. (17), the divergence term induces a coupling between constitutive nonlinearity and spatial nonlocality. Therefore pointwise integration of the differential equation governing the material behaviour over a given domain is precluded. Two different relaxation approaches to deal with this coupling are presented in section 3 and compared in terms of computational performance and physical predictions in section 5.

2.2. Rate-dependent and rate-independent formulations

A rate-dependent (viscoplastic) and a rate-independent formulation of crystal plasticity are presented here and used in the next sections.

2.2.1. Rate-dependent crystal plasticity

As emphasized in (Busso and Cailletaud, 2005) (and references therein) most rate-independent crystal plasticity theories lead to an ill-conditioned problem regarding the selection of active slip systems. Different methods exist to ensure uniqueness, but their numerical implementation may also play a crucial role in the active slip system selection. One possible way to overcome these issues is to work within a rate-dependent setting. In this framework the slip rates are no longer defined by a rate-independent yield surface, but are governed by a rate-dependent potential surface. Smoothness of viscous potential functions allows one to obtain the direction of the strain increment by the normality rule. Evolution of the plastic slip variables γ^s can for example be obtained by considering Norton-type flow rules:

$$\dot{\gamma}^s = \dot{\gamma}_0 \left\langle \frac{f^s}{\tau_0^s} \right\rangle^n \text{sign}\,(\tau^s) = \dot{\gamma}_0 \Phi_{RD}^s(f^s) \text{sign}\,(\tau^s) \tag{19}$$

where $\dot{\gamma}_0$ and n are material parameters which control the rate sensitivity of the material response. Macauley brackets of a scalar x, written $\langle x \rangle$, denote the positive part of x and Φ_{RD}^s denotes the rate-dependent flow function. High values of the power exponent n and of the reference rate $\dot{\gamma}_0$ lead to a low strain rate sensitivity in a given strain rate range.

2.2.2. Rate-independent crystal plasticity

Another possible way to select the active slip systems is to use the rate-independent formulation proposed by Forest and Rubin (2016) and intensively used by Farooq et al. (2020) (later referred to as RubiX formulation). It is characterized by a smooth elastic-plastic transition with no slip indeterminacy. It is based on a strictly rate-independent overstress allowing to remove ill-conditioning of the selection of activated slip systems. The main idea consists in replacing Eq. (19) by:

$$\dot{\gamma}^s \quad = \quad \dot{\varepsilon}_{eq} \left\langle \frac{f^s}{R} \right\rangle \text{sign}\left(\tau^s\right) = \dot{\varepsilon}_{eq} \Phi^s_{RI}(f^s) \text{sign}\left(\tau^s\right) \tag{20}$$

where $\dot{\varepsilon}_{eq}$ is a non-negative homogeneous function of degree one in the total velocity gradient $\underset{\sim}{\boldsymbol{L}}$. The rate–independent flow function is noted Φ^s_{RI} and $\dot{\varepsilon}_{eq}$ is taken here as the total equivalent distortional strain rate:

$$\dot{\varepsilon}_{eq} = \sqrt{\frac{2}{3} \underset{\sim}{\boldsymbol{D}}' : \underset{\sim}{\boldsymbol{D}}'} \qquad \underset{\sim}{\boldsymbol{D}}' = \frac{1}{2}\left(\underset{\sim}{\boldsymbol{L}} + \underset{\sim}{\boldsymbol{L}}^T\right) - \frac{1}{3}(\text{trace}\, \underset{\sim}{\boldsymbol{L}})\underset{\sim}{\boldsymbol{1}} \tag{21}$$

R is a positive constant having the unit of a stress and which controls the amplitude of the rate-independent overstress. As this work proceeds $\dot{\Gamma}$ (resp. Φ^s) will be used indistinguishably to represent either $\dot{\gamma}_0$ or $\dot{\varepsilon}_{eq}$ (resp. Φ^s_{RD} or Φ^s_{RI}).

2.3. Summary of constitutive equations

Equilibrium equations, state laws and evolution equations are summarized in Table 1.

Table 1: Summary of equilibrium equations, state laws and evolutions equations.

equilibrium equations	state laws	evolution equations
$\text{Div}\, \underset{\sim}{\boldsymbol{S}} = \underline{\boldsymbol{0}} \quad \forall \underline{\boldsymbol{X}} \in D_0$	$\underset{\sim}{\boldsymbol{\Pi}}^e = \underset{\approx}{\boldsymbol{C}} : \underset{\sim}{\boldsymbol{E}}^e_{GL}$	$\dot{\underset{\sim}{\boldsymbol{E}}} = \dot{\underset{\sim}{\boldsymbol{F}}}.\underset{\sim}{\boldsymbol{F}}^{-1}.\underset{\sim}{\boldsymbol{E}} - \underset{\sim}{\boldsymbol{E}}.\left(\sum_{s=1}^{N} \dot{\gamma}^s \underset{\sim}{\boldsymbol{N}}^s\right)$
$\text{Div}\, \underline{\boldsymbol{M}} - S = 0 \quad \forall \underline{\boldsymbol{X}} \in D_0$	$\underline{\boldsymbol{M}} = A\underline{\boldsymbol{K}}$	$\dot{\gamma}^s = \dot{\Gamma}\Phi^s\left(\left\lvert\tau^s\right\rvert - \left(\tau^s_c - \frac{\rho_\sharp}{\rho_0} S\right)\right) \text{sign}\left(\tau^s\right)$
$\underline{\boldsymbol{T}} = \underset{\sim}{\boldsymbol{S}}.\underline{\boldsymbol{n}}_0 \quad \forall \underline{\boldsymbol{X}} \in \partial D_0$	$S = \rho_0 \dfrac{\partial \psi_h}{\partial \gamma_{cum}} - \overline{H}$	$\dot{r}^s = g_s(r_s)\lvert\dot{\gamma}^s\rvert$
$M = \underline{\boldsymbol{M}}.\underline{\boldsymbol{n}}_0 \quad \forall \underline{\boldsymbol{X}} \in \partial D_0$		$\dot{\gamma}_{cum} = \sum_{s=1}^{N} \lvert\dot{\gamma}^s\rvert$

3. Relaxations of strain gradient plasticity theory

3.1. Micromorphic approach

Wulfinghoff and Böhlke (2012) and Ling et al. (2018) used the micromorphic approach (Forest, 2009) to tackle the issue of nonlocality and nonlinearity coupling. Their approach is based on the

introduction of an additional degree of freedom, denoted γ_χ, enriching the kinematic description of the material behaviour. γ_χ is the micromorphic (nonlocal) counterpart of γ_{cum}, and, therefore it bears the same physical interpretation. However γ_{cum} and γ_χ are treated independently in the resolution of the equations governing the material behaviour. In this context the principle of virtual power Eq. (3) is extended to higher order contributions:

$$\int_{D_0} \left(\underset{\sim}{\boldsymbol{S}} : \dot{\underset{\sim}{\boldsymbol{F}}} + S\dot{\gamma}_\chi + \underline{\boldsymbol{M}} . \mathrm{Grad}\, \dot{\gamma}_\chi \right) \mathrm{d}V_0 = \int_{\partial D_0} \left(\underline{\boldsymbol{T}} . \underline{\dot{\boldsymbol{u}}} + M\dot{\gamma}_\chi \right) \mathrm{d}S_0 \quad \forall \underline{\dot{\boldsymbol{u}}}, \quad \forall \dot{\gamma}_\chi, \quad \forall D_0 \tag{22}$$

Using the divergence theorem one can again derive the balance laws in the reference configuration , namely Eq. (4) and (5), while on the surface ∂D_0 stresses are in equilibrium with the traction vector and scalar as in Eq. (6) and (7). In order to ensure quasi-equality between γ_{cum} and γ_χ, a penalty term is introduced in the free energy potential penalizing their difference $\gamma_{cum} - \gamma_\chi$, where H_χ is a penalty modulus which is usually taken large enough so that the results obtained with the model do not depend on the chosen value (typically $H_\chi \sim 10^4 - 10^5\,\mathrm{MPa}$). With this method the specific free energy density Eq. (8) now writes

$$\begin{aligned} \psi \left(\underset{\sim}{\boldsymbol{E}}^e_{GL}, r^s, \gamma_{cum}, \gamma_\chi, \underline{\boldsymbol{K}}_\chi \right) = & \frac{1}{2\rho_\sharp} \underset{\sim}{\boldsymbol{E}}^e_{GL} : \underset{\approx}{\boldsymbol{C}} : \underset{\sim}{\boldsymbol{E}}^e_{GL} + \psi_h(r^s, \gamma_{cum}) \\ & + \frac{A}{2\rho_0} \underline{\boldsymbol{K}}_\chi . \underline{\boldsymbol{K}}_\chi + \frac{H_\chi}{2\rho_0} (\gamma_{cum} - \gamma_\chi)^2 \end{aligned} \tag{23}$$

where $\underline{\boldsymbol{K}}_\chi = \mathrm{Grad}\, \gamma_\chi$. The 1-st and 2-nd principles of thermodynamics now enforce

$$\frac{\underset{\sim}{\boldsymbol{S}}}{\rho_0} : \dot{\underset{\sim}{\boldsymbol{F}}} + \frac{S}{\rho_0}\dot{\gamma}_\chi + \frac{\underline{\boldsymbol{M}}}{\rho_0} . \underline{\dot{\boldsymbol{K}}}_\chi - \dot{\psi} \geq 0 \tag{24}$$

The mechanical dissipation therefore becomes

$$\begin{aligned} & \left(\frac{\underset{\sim}{\boldsymbol{\Pi}}^e}{\rho_\sharp} - \frac{\partial \psi}{\partial \underset{\sim}{\boldsymbol{E}}^e_{GL}} \right) : \dot{\underset{\sim}{\boldsymbol{E}}}^e_{GL} + \frac{\underset{\sim}{\boldsymbol{\Pi}}^M}{\rho_\sharp} : \left(\dot{\underset{\sim}{\boldsymbol{P}}} . \underset{\sim}{\boldsymbol{P}}^{-1} \right) + \left(\frac{S}{\rho_0} - \frac{\partial \psi}{\partial \gamma_\chi} \right) \dot{\gamma}_\chi - \frac{\partial \psi}{\partial \gamma_{cum}} \dot{\gamma}_{cum} \\ & + \left(\frac{\underline{\boldsymbol{M}}}{\rho_0} - \frac{A}{\rho_0} \underline{\boldsymbol{K}}_\chi \right) . \underline{\dot{\boldsymbol{K}}}_\chi - \sum_{s=1}^{N} \frac{\partial \psi_h}{\partial r^s} \dot{r}^s \geq 0 \end{aligned} \tag{25}$$

After selecting non–dissipative contributions, the following state laws are adopted

$$\underset{\sim}{\boldsymbol{\Pi}}^e = \rho_\sharp \frac{\partial \psi}{\partial \underset{\sim}{\boldsymbol{E}}^e_{GL}} \tag{26}$$

$$S = \rho_0 \frac{\partial \psi}{\partial \gamma_\chi} = -H_\chi (\gamma_{cum} - \gamma_\chi) \tag{27}$$

$$\underline{\boldsymbol{M}} = \rho_0 \frac{\partial \psi}{\partial \underline{\boldsymbol{K}}_\chi} = A \underline{\boldsymbol{K}}_\chi \tag{28}$$

In contrast to the previous section, the constitutive assumption that S is non-dissipative is made here. Therefore the energy dissipated with $\dot{\gamma}_\chi$ vanishes. Yet, a term involving the higher order stress S and conjugate to $\dot{\gamma}_{cum}$ remains. The residual dissipation now writes

$$\frac{\underset{\sim}{\boldsymbol{\Pi}}^M}{\rho_\sharp} : \left(\dot{\underset{\sim}{\boldsymbol{P}}} . \underset{\sim}{\boldsymbol{P}}^{-1} \right) - \sum_{s=1}^{N} \frac{\partial \psi_h}{\partial r^s} \dot{r}^s - \left(\frac{H_\chi}{\rho_0} (\gamma_{cum} - \gamma_\chi) + \frac{\partial \psi_h}{\partial \gamma_{cum}} \right) \dot{\gamma}_{cum} \geq 0 \tag{29}$$

which can also be written

$$\sum_{s=1}^{N} \left[|\tau^s| - \frac{\rho_\sharp}{\rho_0} H_\chi (\gamma_{cum} - \gamma_\chi) - \rho_\sharp \frac{\partial \psi_h}{\partial \gamma_{cum}} - \rho_\sharp \frac{\partial \psi_h}{\partial r^s} g_s(r_s) \right] |\dot{\gamma}^s| \geq 0 \tag{30}$$

By combining state law Eq. (27), equilibrium equation Eq. (5) and state law Eq. (28) it comes $S = -H_\chi(\gamma_{cum} - \gamma_\chi) = \mathrm{Div}\,\underline{\boldsymbol{M}} = \mathrm{Div}\,(A\underline{\boldsymbol{K}}_\chi)$. Therefore the micromorphic approach is a relaxation[1] of the strict strain gradient formulation from section 2 in the sense that no spatial derivatives are explicitly involved for the non-local contribution in Eq. (30). The plastic slip rates now are

$$\dot{\gamma}^s = \dot{\Gamma}\Phi^s\left(|\tau^s| - \left(\tau_c^s + \tfrac{\rho_\sharp}{\rho_0}H_\chi(\gamma_{cum} - \gamma_\chi)\right)\right)\mathrm{sign}\,(\tau^s) \tag{31}$$

The main drawback of this method, in the context of viscoplasticity, lies in the necessity of taking a large value for H_χ in order to assure quasi-equality between γ_χ and γ_{cum}. In the limit case of almost rate insensitivity the viscoplastic parameters n and $\dot{\gamma}_0$ are such that the nonlinear system of equation governing activation of slip systems is very stiff and thus extremely sensitive to the errors that are made during the iterative process (typically an Euler-backward scheme) used to solve them. As a consequence small time steps are necessary in order to achieve convergence. One possible way to tackle this issue and allow the use of large time steps with the micromorphic approach is to use a rate-independent crystal plasticity setting such as the one proposed by Forest and Rubin (2016) and presented in section 2.2.2.

3.2. Lagrange multiplier approach

Alternatively, the Lagrange multiplier method proposed by Fortin and Glowinski (1983) and successfully applied in (Zhang et al., 2018) can be used. This approach is described here for relaxing the theory presented in section 2.1. The main ideas of the method are first to duplicate the variable upon which the nonlinear-nonlocal coupling is acting and second to enforce equality between both variables through a Lagrangian function. In the context of the model presented in section 2.1 the nonlocal instance of the coupling variable will be denoted γ_χ while its local instance is γ_{cum}. Similarly to the micromorphic approach, $\underline{\boldsymbol{K}}_\chi = \mathrm{Grad}\,\gamma_\chi$ is regarded as a state variable. Enforcing equality between γ_χ and γ_{cum} is achieved using a Lagrange multiplier λ. It turns out that the previous free energy density in Eq. (8) becomes a Lagrangian function

$$\begin{aligned}\mathcal{L}\left(\underset{\sim}{\boldsymbol{E}}^e_{GL}, \gamma_{cum}, r^s, \gamma_\chi, \underline{\boldsymbol{K}}_\chi, \lambda\right) = {} & \frac{1}{2\rho_\sharp}\underset{\sim}{\boldsymbol{E}}^e_{GL} : \underset{\approx}{\boldsymbol{C}} : \underset{\sim}{\boldsymbol{E}}^e_{GL} + \psi_h(r^s, \gamma_{cum}) \\ & + \frac{A}{2\rho_0}\underline{\boldsymbol{K}}_\chi.\underline{\boldsymbol{K}}_\chi + \frac{\lambda}{\rho_0}(\gamma_\chi - \gamma_{cum}) + \frac{\mu_\chi}{2\rho_0}(\gamma_\chi - \gamma_{cum})^2\end{aligned} \tag{32}$$

where μ_χ is a Lagrangian penalization modulus. The 1-st and 2-nd principles of thermodynamics still require to verify Eq. (24), where $\dot{\psi}$ is now replaced by $\dot{\mathcal{L}}$, and the mechanical dissipation is written as

[1] Relaxation is meant here in a sense different from Neff et al. (2014), where this terminology was used to describe a "linear micromorphic model with symmetric Cauchy force stresses" which is put in contrast to "the classical Mindlin-Eringen model for micromorphic media with intrinsically non-symmetric force stresses".

in Eq. (25). The postulated state laws are now

$$\underset{\sim}{\boldsymbol{\Pi}}^{e} = \rho_\sharp \frac{\partial \psi}{\partial \underset{\sim}{\boldsymbol{E}}^{e}_{GL}} \tag{33}$$

$$S = \rho_0 \frac{\partial \psi}{\partial \gamma_\chi} = \lambda + \mu_\chi(\gamma_\chi - \gamma_{cum}) = \Delta_\chi - \mu_\chi \gamma_{cum} \tag{34}$$

$$\underline{\boldsymbol{M}} = \rho_0 \frac{\partial \psi}{\partial \underline{\boldsymbol{K}}_\chi} = A \underline{\boldsymbol{K}}_\chi \tag{35}$$

Similarly to the micromorphic approach, the constitutive assumption that S is non-dissipative is made. Therefore the energy dissipated with $\dot{\gamma_\chi}$ vanishes. Yet, a term involving the higher order stress S and conjugate to $\dot{\gamma}_{cum}$ remains. For convenience we introduce the scalar stress $\Delta_\chi = \lambda + \mu_\chi \gamma_\chi$. By definition $\partial \mathcal{L}/\partial \lambda$ must vanish when the constraint $\gamma_{cum} = \gamma_\chi$ is met

$$\frac{\partial \mathcal{L}}{\partial \lambda} \dot{\lambda} = (\gamma_\chi - \gamma_{cum}) \frac{\dot{\lambda}}{\rho_0} = 0 \tag{36}$$

and therefore the residual mechanical dissipation becomes

$$\frac{\underset{\sim}{\boldsymbol{\Pi}}^{M}}{\rho_\sharp} : \left(\dot{\underset{\sim}{\boldsymbol{P}}} \underset{\sim}{\boldsymbol{P}}^{-1} \right) - \sum_{s=1}^{N} \frac{\partial \psi_h}{\partial r^s} \dot{r}^s - \left(\frac{\mu_\chi \gamma_{cum} - \Delta_\chi}{\rho_0} + \frac{\partial \psi_h}{\partial \gamma_{cum}} \right) \dot{\gamma}_{cum} \geq 0 \tag{37}$$

which can also be written

$$\sum_{s=1}^{N} \left[|\tau^s| - \frac{\rho_\sharp}{\rho_0} \left(\mu_\chi \gamma_{cum} - \Delta_\chi \right) - \rho_\sharp \frac{\partial \psi_h}{\partial \gamma_{cum}} - \rho_\sharp \frac{\partial \psi_h}{\partial r^s} g_s(r_s) \right] |\dot{\gamma}^s| \geq 0 \tag{38}$$

By combining state law Eq. (34), equilibrium Eq. (5) and state law Eq. (35) it comes $S = \Delta_\chi - \mu_\chi \gamma_{cum} = \mathrm{Div}\, \underline{\boldsymbol{M}} = \mathrm{Div}\,(A \underline{\boldsymbol{K}}_\chi)$. Therefore the Lagrange multiplier approach is a relaxation of the strict strain gradient formulation from section 2 in the sense that no spatial derivative is explicitly involved in the non-local contribution in Eq. (38). The plastic slip rates now are

$$\dot{\gamma}^s = \dot{\Gamma} \Phi^s \left(|\tau^s| - \left(\tau_c^s + \frac{\rho_\sharp}{\rho_0} \left(\mu_\chi \gamma_{cum} - \Delta_\chi \right) \right) \right) \mathrm{sign}\,(\tau^s) \tag{39}$$

4. Numerical implementation

The numerical implementation in a finite element setting of the Lagrange multiplier approach is described. Details on the implementation of the micromorphic formulation can be found in (Ling et al., 2018).

4.1. Integration of constitutive equations

The sets of degrees of freedom (DOF), input variables (IN), output variables (OUT) and integration variables (INT) are:

$$\text{DOF: } \{\underline{\boldsymbol{u}}, \gamma_\chi, \lambda\} \qquad \text{IN: } \{\underset{\sim}{\boldsymbol{F}}, \Delta_\chi\} \qquad \text{OUT: } \{\underset{\sim}{\boldsymbol{S}}, \gamma_M\} \qquad \text{INT: } \{\underset{\sim}{\boldsymbol{E}}, \gamma^s, r^s, \gamma_{cum}\} \tag{40}$$

where γ_M is merely a copy of γ_{cum} obtained at the end of the constitutive integration. Integrating the constitutive equations consists, for known values of all variables at a given time step n, in computing

the evolution of the output and internal variables at next time step $n+1$ knowing the evolution laws of the input variables. At the global level the output variables need to satisfy the weak form of the balance equations Eqs. (4), (5), (6) and Eq. (7). It can be noted that

$$\underset{\sim}{\boldsymbol{S}} = J\underset{\sim}{\boldsymbol{\sigma}}.\underset{\sim}{\boldsymbol{F}}^{-T} = \frac{1}{2}\frac{J}{J_e}\underset{\sim}{\boldsymbol{E}}.\left(\underset{\approx}{\boldsymbol{C}} : \left(\underset{\sim}{\boldsymbol{E}}^{T}.\underset{\sim}{\boldsymbol{E}} - \underset{\sim}{\mathbf{1}}\right)\right).\underset{\sim}{\boldsymbol{E}}^{T}.\underset{\sim}{\boldsymbol{F}}^{-T} \tag{41}$$

where state law Eq. (26) has been used along with the elastic free energy used in Eq. (32) and $J = \det\left(\underset{\sim}{\boldsymbol{F}}\right)$ and $J_e = \det\left(\underset{\sim}{\boldsymbol{E}}\right)$. The evolution of $\underset{\sim}{\boldsymbol{S}}$ depends on evolutions of $\underset{\sim}{\boldsymbol{E}}$ and $\underset{\sim}{\boldsymbol{F}}$. Within the Lagrange multiplier approach the set of equations to be solved at the local level are similar to evolution equations in Table 1 and can be reformulated incrementally as the problem of finding the solution of the following system of equations $\mathcal{R}(\Delta\underset{\sim}{\boldsymbol{E}}, \Delta\gamma^s, \Delta r^s, \Delta\gamma_{cum})$:

$$\mathcal{R} = \begin{cases} \mathcal{R}_{\underset{\sim}{\boldsymbol{E}}} = \Delta\underset{\sim}{\boldsymbol{E}} - \Delta\underset{\sim}{\boldsymbol{F}}.\underset{\sim}{\boldsymbol{F}}^{-1}.\underset{\sim}{\boldsymbol{E}} - \underset{\sim}{\boldsymbol{E}}.\left(\sum_{s=1}^{N}\Delta\gamma^s\underset{\sim}{\boldsymbol{N}}^s\right) = 0 \\ \mathcal{R}_{\gamma^s} = \Delta\gamma^s - \Delta\Gamma\Phi^s\left(|\tau^s| - \left\langle \tau_c^s - \dfrac{\rho_\sharp}{\rho_0}\left(\Delta_\chi - \mu_\chi\gamma_{cum}\right)\right\rangle\right)\mathrm{sign}\left(\tau^s\right) = 0 \\ \mathcal{R}_{r^s} = \Delta r^s - g_s(r_s)|\Delta\gamma^s| = 0 \\ \mathcal{R}_{\gamma_{cum}} = \Delta\gamma_{cum} - \sum_{s=1}^{N}|\Delta\gamma^s| = 0 \end{cases} \tag{42}$$

where $\Delta\Gamma = \Delta\varepsilon_{eq}$ in the rate-independent formulation and $\Delta\Gamma = \dot{\gamma}_0\Delta t$ in the rate-dependent formulation. Note that it may happen that $\tau_c^s - (\rho_\sharp/\rho_0)\left(\Delta_\chi - \mu_\chi\gamma_{cum}\right) < 0$. In that case this value is replaced by 0 in the computation. Note also that Eq. (42) does not guarantee that plastic incompressibility is satisfied. In order to fulfill this condition, the tensor $\underset{\sim}{\boldsymbol{E}}$ is corrected at the beginning of each iteration of the Newton algorithm used to solve Eq. (42). This correction amounts to replace $\underset{\sim}{\boldsymbol{E}}$ by $(J/J_e)^{1/3}\underset{\sim}{\boldsymbol{E}}$. As a result, the corrected tensor $\underset{\sim}{\boldsymbol{P}}$ verifies $\det\left(\underset{\sim}{\boldsymbol{P}}\right) = 1$, which corresponds to the plastic incompressibility condition. Solving $\mathcal{R}(\Delta\underset{\sim}{\boldsymbol{E}}, \Delta\gamma^s, \Delta r^s, \Delta\gamma_{cum}) = 0$ is performed using a Newton algorithm with an Euler backward (implicit) scheme which requires computation of the Jacobian matrix $\mathcal{J} = \partial\mathcal{R}/\partial\Delta v_{\mathrm{int}}$ (or some approximation of it). The analytical Jacobian matrix for the resolution of Eq. (42) is given in Appendix A.

4.2. Finite element formulation

The model is implemented in the finite element software `Z-set` using a 3D total Lagrangian formulation following (Besson and Foerch, 1998; Z–set package, 2020). The principle of virtual power in the context of the Lagrange multiplier method combines Eqs. (4), (5), (6), (7), and in addition Eq. (36) must be satisfied

$$\begin{cases} \forall\underline{\dot{\boldsymbol{u}}} & \displaystyle\int_{D_0}\underset{\sim}{\boldsymbol{S}} : \dot{\underset{\sim}{\boldsymbol{F}}}\mathrm{d}V_0 = \int_{\partial D_0}\underline{\boldsymbol{T}}.\underline{\dot{\boldsymbol{u}}}\,\mathrm{d}S_0 & (43) \\ \forall\dot{\gamma}_\chi & \displaystyle\int_{D_0} A\underline{\boldsymbol{K}}_\chi.\underline{\dot{\boldsymbol{K}}}_\chi + (\Delta_\chi - \mu_\chi\gamma_M)\dot{\gamma}_\chi\mathrm{d}V_0 = \int_{\partial D_0} M\dot{\gamma}_\chi\mathrm{d}S_0 & (44) \\ \forall\dot{\lambda} & \displaystyle\int_{D_0}(\gamma_\chi - \gamma_M)\dot{\lambda}\mathrm{d}V_0 = 0 & (45) \end{cases}$$

The finite element problem is solved by a monolithic iterative method. The material body occupies the domain D_0 in its reference configuration, the decomposition of this body in n finite elements raises

$$\begin{cases} \forall \underline{\dot{\boldsymbol{u}}} & \displaystyle\sum_{e=1}^{n} \int_{D_0^e} \underset{\sim}{\boldsymbol{S}} : \dot{\underset{\sim}{\boldsymbol{F}}} \mathrm{d}V_0^e = \sum_{e=1}^{n_S} \int_{\partial D_0^e} \underline{\boldsymbol{T}} . \underline{\dot{\boldsymbol{u}}} \, \mathrm{d}S_0^e & (46) \\ \forall \dot{\gamma}_\chi & \displaystyle\sum_{e=1}^{n} \int_{D_0^e} A \underline{\boldsymbol{K}}_\chi . \underline{\dot{\boldsymbol{K}}}_\chi + (\Delta_\chi - \mu_\chi \gamma_M) \dot{\gamma}_\chi \mathrm{d}V_0^e = \sum_{e=1}^{n_S} \int_{\partial D_0^e} M \dot{\gamma}_\chi \mathrm{d}S_0^e & (47) \\ \forall \dot{\lambda} & \displaystyle\sum_{e=1}^{n} \int_{D_0^e} (\gamma_\chi - \gamma_M) \dot{\lambda} \mathrm{d}V_0^e = 0 & (48) \end{cases}$$

The boundary ∂D_0 is discretized into n_S surface elements ∂D_0^e for the application of surface tractions. As this section proceeds tensors are written with index notations. Within the volume of each element the degrees of freedom u_i, γ_χ and λ are interpolated by their values at p nodes for the displacements ($\tilde{u}_i^a$ for $a \in [1;p]$) and q nodes for Lagrange multiplier λ and the microslip γ_χ ($\widetilde{\lambda}^b$ and $\tilde{\gamma}_\chi^b$ for $b \in [1;q]$)

$$u_i = \sum_{a=1}^{p} {}^u N^a \widetilde{u}_i^a \qquad \gamma_\chi = \sum_{b=1}^{q} {}^\chi N^b \widetilde{\gamma}_\chi^b \qquad \lambda = \sum_{b=1}^{q} {}^\chi N^b \widetilde{\lambda}^b \quad \text{thus} \quad \Delta_\chi = \sum_{b=1}^{q} {}^\chi N^b \left(\widetilde{\lambda}^b + \mu_\chi \widetilde{\gamma}_\chi^b \right) \tag{49}$$

where ${}^u N^a$ and ${}^\chi N^b$ are shape functions, the superscripts denoting the element node number. The deformation gradient F_{ij} and the Lagrangian gradient of microslip K_i are given by

$$F_{ij} = \sum_{a=1}^{p} {}^u B_j^a \widetilde{u}_i^a \qquad K_{\chi i} = \sum_{b=1}^{q} {}^\chi B_i^b \widetilde{\gamma}_\chi^b \tag{50}$$

with ${}^u B_j^a = \partial {}^u N^a / \partial X_j$ and ${}^\chi B_i^b = \partial {}^\chi N^b / \partial X_i$. Using these relations in Eqs. (46), (47) and (48) leads to

$$\begin{cases} \displaystyle\sum_{e=1}^{n} \int_{D_0^e} S_{ij} \sum_{a=1}^{p} {}^u B_j^a \dot{\tilde{u}}_i^a \mathrm{d}V_0^e = \sum_{e=1}^{n_S} \int_{\partial D_0^e} T_i \sum_{a=1}^{p} {}^u N^a \dot{\tilde{u}}_i^a \mathrm{d}S_0^e & (51) \\ \displaystyle\sum_{e=1}^{n} \int_{D_0^e} A \sum_{b=1}^{q} {}^\chi B_i^b \widetilde{\gamma}_\chi^b \sum_{b=1}^{q} {}^\chi B_i^b \dot{\tilde{\gamma}}_\chi^b + \left(\sum_{b=1}^{q} {}^\chi N^b \left(\widetilde{\lambda}^b + \mu_\chi \widetilde{\gamma}_\chi^b \right) - \mu_\chi \gamma_M \right) \sum_{b=1}^{q} {}^\chi N^b \dot{\tilde{\gamma}}_\chi^b \mathrm{d}V_0^e = & (52) \\ \displaystyle\sum_{e=1}^{n_S} \int_{\partial D_0^e} M \sum_{b=1}^{q} {}^\chi N^b \dot{\tilde{\gamma}}_\chi^b \mathrm{d}S_0^e & \\ \displaystyle\sum_{e=1}^{n} \int_{D_0^e} \left(\sum_{b=1}^{q} {}^\chi N^b \widetilde{\gamma}_\chi^b - \gamma_M \right) \sum_{b=1}^{q} {}^\chi N^b \dot{\tilde{\lambda}}^b \mathrm{d}V_0^e = 0 & (53) \end{cases}$$

which can be reformulated as

$$\begin{cases} \displaystyle\sum_{e=1}^{n} \sum_{a=1}^{p} \left[\int_{D_0^e} S_{ij} \, {}^u B_j^a \mathrm{d}V_0^e \right] \dot{\tilde{u}}_i^a = \sum_{e=1}^{n_S} \sum_{a=1}^{p} \left[\int_{\partial D_0^e} T_i \, {}^u N^a \mathrm{d}S_0^e \right] \dot{\tilde{u}}_i^a & (54) \\ \displaystyle\sum_{e=1}^{n} \sum_{b=1}^{q} \left[\int_{D_0^e} A \sum_{k=1}^{q} {}^\chi B_i^k \widetilde{\gamma}_\chi^k \, {}^\chi B_i^b + \left(\sum_{k=1}^{q} {}^\chi N^k \left(\widetilde{\lambda}^k + \mu_\chi \widetilde{\gamma}_\chi^k \right) - \mu_\chi \gamma_M \right) {}^\chi N^b \mathrm{d}V_0^e \right] \dot{\tilde{\gamma}}_\chi^b = & (55) \\ \displaystyle\sum_{e=1}^{n_S} \sum_{b=1}^{q} \left[\int_{\partial D_0^e} M \, {}^\chi N^b \mathrm{d}S_0^e \right] \dot{\tilde{\gamma}}_\chi^b & \\ \displaystyle\sum_{e=1}^{n} \sum_{b=1}^{q} \left[\int_{D_0^e} \left(\sum_{k=1}^{q} {}^\chi N^k \widetilde{\gamma}_\chi^b - \gamma_M \right) {}^\chi N^b \mathrm{d}V_0^e \right] \dot{\tilde{\lambda}}^b = 0 & (56) \end{cases}$$

According to Eqs. (54), (55), (56) an internal reaction is associated with each degree-of-freedom. We thus refer to $R^a_{\text{int}(u_i,e)}$ as the internal reaction related to u_i on node a of element e

$$R^a_{\text{int}(u_i,e)} = \int_{D^e_0} S_{ij}{}^u B^a_j \mathrm{d}V^e_0 \tag{57}$$

and to $R^b_{\text{int}(\gamma_\chi,\text{e})}$ (resp. $R^b_{\text{int}(\lambda,e)}$) as the internal reaction related to γ_χ (resp. λ) on node b of element e

$$R^b_{\text{int}(\gamma_\chi,\text{e})} = \int_{D^e_0} A \sum_{k=1}^{q} {}^\chi B^k_i \widetilde{\gamma}^k_\chi {}^\chi B^b_i + \left(\sum_{k=1}^{q} {}^\chi N^k \left(\widetilde{\lambda}^k + \mu_\chi \widetilde{\gamma}^k_\chi \right) - \mu_\chi \gamma_M \right) {}^\chi N^b \mathrm{d}V^e_0 \tag{58}$$

$$R^b_{\text{int}(\lambda,e)} = \int_{D^e_0} \left(\sum_{k=1}^{q} {}^\chi N^k \widetilde{\gamma}^b_\chi - \gamma_M \right) {}^\chi N^b \mathrm{d}V^e_0 \tag{59}$$

Analogously, an external reaction is associated to each degree of freedom. We refer to $R^a_{\text{ext}(u_i,e)}$, $R^b_{\text{ext}(\gamma_\chi,e)}$, $R^b_{\text{ext}(\lambda,e)}$ as the external reactions related to u_i on node a, γ_χ and λ on node b of element e

$$R^a_{\text{ext}(u_i,e)} = \int_{\partial D^e_0} T_i{}^u N^a \mathrm{d}S^e_0 \qquad R^b_{\text{ext}(\gamma_\chi,e)} = \int_{\partial D^e_0} M^\chi N^b \mathrm{d}S^e_0 \qquad R^b_{\text{ext}(\lambda,e)} = 0 \tag{60}$$

With these expressions Eqs. (54), (55), (56) write

$$\begin{cases} \displaystyle\sum_{e=1}^{n} \sum_{a=1}^{p} R^a_{\text{int}(u_i,e)} \dot{\widetilde{u}}^a_i = \sum_{e=1}^{n_S} \sum_{a=1}^{p} R^a_{\text{ext}(u_i,e)} \dot{\widetilde{u}}^a_i & (61) \\ \displaystyle\sum_{e=1}^{n} \sum_{b=1}^{q} R^b_{\text{int}(\gamma_\chi,\text{e})} \dot{\widetilde{\gamma}}^b_\chi = \sum_{e=1}^{n_S} \sum_{b=1}^{q} R^b_{\text{ext}(\gamma_\chi,e)} \dot{\widetilde{\gamma}}^b_\chi & (62) \\ \displaystyle\sum_{e=1}^{n} \sum_{b=1}^{q} R^b_{\text{int}(\lambda,e)} \dot{\widetilde{\lambda}}^b = \sum_{e=1}^{n_S} \sum_{b=1}^{q} R^b_{\text{ext}(\lambda,e)} \dot{\widetilde{\lambda}}^b & (63) \end{cases}$$

This system of equations is solved using Newton's method. The details of the numerical implementation are given in Appendix B and Appendix C. As this work proceeds, quadratic (resp. linear) interpolation functions are used for the displacement (resp. microslip and Lagrange multiplier) degrees of freedom.

5. Numerical examples

5.1. 1D localization band formation

5.1.1. Validation of the Lagrange multiplier implementation

Validation of the implementation is done by solving the problem of a periodic bar of length L along $\underline{\boldsymbol{X}}_2$ (see Figure 1a) in simple shear with a single slip system and a linear softening behavior ($H < 0$)

$$\tau_c(\gamma) = \tau_0 + H\gamma \tag{64}$$

Such a hardening behaviour corresponds to a hardening free energy potential $\psi_h = H\gamma^2/2$. In the reference configuration, the gliding direction $\underline{\boldsymbol{m}}$ is aligned with $\underline{\boldsymbol{X}}_1$, the normal to the slip plane $\underline{\boldsymbol{n}}$ is aligned with $\underline{\boldsymbol{X}}_2$. A macroscopic shear deformation $\overline{\underset{\sim}{\boldsymbol{F}}} = \underset{\sim}{\mathbf{1}} + \overline{F}_{12} \underline{\boldsymbol{m}} \otimes \underline{\boldsymbol{n}}$ is imposed such that the

displacement field is given by $\underline{\boldsymbol{u}} = (\underset{\sim}{\overline{\boldsymbol{F}}} - \underset{\sim}{\mathbf{1}}).\underline{\boldsymbol{X}} + \underline{\boldsymbol{v}}(\underline{\boldsymbol{X}})$. Periodic boundary conditions are imposed on the displacement fluctuation $\underline{\boldsymbol{v}}$, micro-slip variable γ_χ and Lagrange multiplier λ. As discussed in (Scherer et al., 2019) the analytical solution to this problem, in terms of plastic slip, is a localization band following a sine shape within the $[-\lambda_0/2; \lambda_0/2]$ region and no slip elsewhere

$$\gamma(X_2, \overline{F}_{12}) = \begin{cases} \dfrac{|\tau| - \tau_0}{H}\left(\cos\left(2\pi\dfrac{X_2}{\lambda_0}\right) + 1\right) & \text{if} \quad X_2 \in \left[-\dfrac{\lambda_0}{2}; \dfrac{\lambda_0}{2}\right] \\ 0 & \text{if} \quad X_2 \in \left[-\dfrac{L}{2}; -\dfrac{\lambda_0}{2}\right] \cup \left[\dfrac{\lambda_0}{2}; \dfrac{L}{2}\right] \end{cases} \tag{65}$$

with the wavelength $\lambda_0 = 2\pi\sqrt{A/|H|}$, where H is the slope of linear softening and A the higher order modulus. It is important to notice that in the context of the Lagrange multiplier approach, when the penalty factor $\mu_\chi = 0$, the Lagrange multiplier λ, which is a degree of freedom, coincides with the Laplacian of γ in this elementary problem. Yet, it can be noted from Eq. (65) that the Laplacian of γ takes the form

$$\Delta\gamma(X_2, \overline{F}_{12}) = \begin{cases} -\left(\dfrac{2\pi}{\lambda_0}\right)^2 \dfrac{|\tau| - \tau_0}{H}\cos\left(2\pi\dfrac{X_2}{\lambda_0}\right) & \text{if} \quad X_2 \in \left[-\dfrac{\lambda_0}{2}; \dfrac{\lambda_0}{2}\right] \\ 0 & \text{if} \quad X_2 \in \left[-\dfrac{L}{2}; -\dfrac{\lambda_0}{2}\right] \cup \left[\dfrac{\lambda_0}{2}; \dfrac{L}{2}\right] \end{cases} \tag{66}$$

which is discontinuous in $\pm\lambda_0/2$. Therefore solving numerically this problem by finite elements with standard continuous shape functions might lead to difficulties. Figure 1b and 1c show the finite element solutions to this problem in case $\mu_\chi = 0$, for discretizations of respectively $n = 51$ and $n = 201$ elements along the $\underline{\boldsymbol{X}}_2$ direction of the bar and a wavelength $\lambda_0 = L/2$. It is observed that strong oscillations of plastic slip (solid red line) occur around the analytical solution (dashed black line) for both finite element discretizations. These oscillations are caused by abnormal fluctuations of the Lagrange multiplier (solid blue line) also plotted on the same figures. Fluctuations are probably due to poor approximations of the Lagrange multiplier degree of freedom at the discontinuity. This issue can be solved by using the Lagrangian penalization term in Eq. (32). The additional penalty term is very similar to the micromorphic penalization, but it bears a completely different meaning. While in the micromorphic approach H_χ has to be large in order to ensure quasi-equality between γ_{cum} and γ_χ, in the Lagrange multiplier approach μ_χ only helps to provide additional coercivity and can take much lower values in practice. Figure 1d and 1e show the finite element solution of the periodic bar in simple shear when $\mu_\chi = 50\,\text{MPa}$ for $n = 51$ and $n = 201$. It can be observed that the oscillations almost vanish everywhere, except at $\pm\lambda_0/2$ where their amplitude is much lower and that a smooth solution coinciding with the analytical solution is obtained everywhere else. Another possible alternative to properly account for the discontinuity of the Lagrange multiplier could be to use a discontinuous Galerkin finite element formulation (Hughes et al., 2006; Cockburn et al., 2012).

Another observation can be made on the interdependence between mesh density and the value of μ_χ which yields a smooth profile of Δ_χ. The profiles of Δ_χ in a reduced region of the bar for several values of μ_χ and the two different mesh densities $n = 51$ and $n = 201$ are plotted in Figure 2. It can

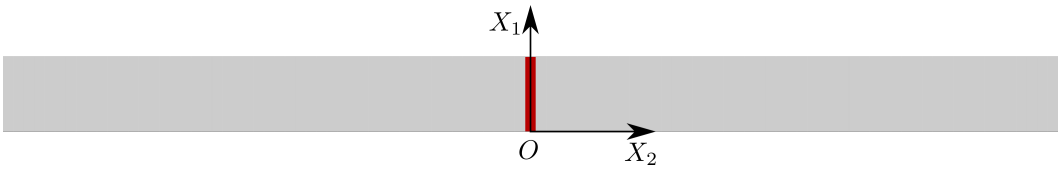

(a)

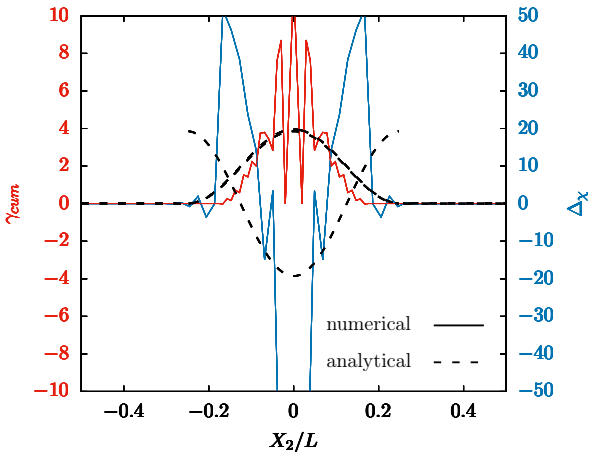

(b) $n = 51$ and $\mu_\chi = 0\,\mathrm{MPa}$

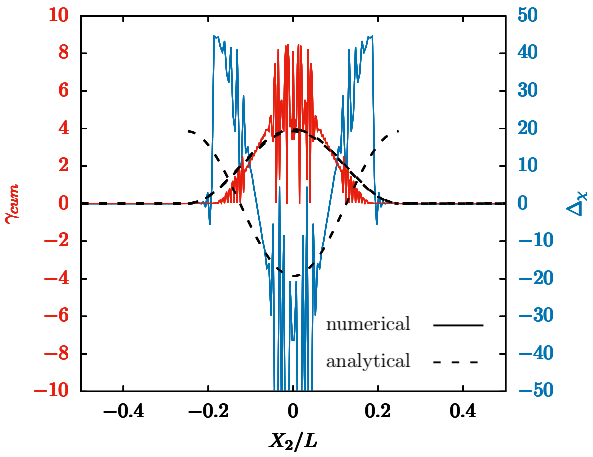

(c) $n = 201$ and $\mu_\chi = 0\,\mathrm{MPa}$

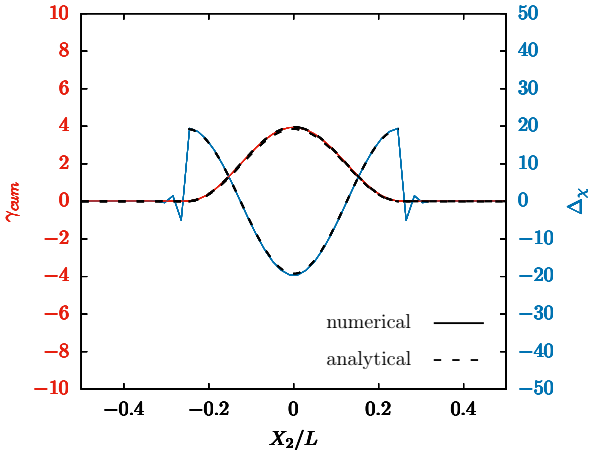

(d) $n = 51$ and $\mu_\chi = 50\,\mathrm{MPa}$

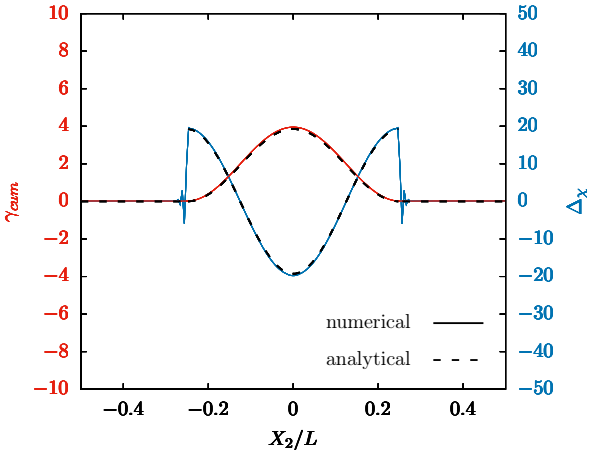

(e) $n = 201$ and $\mu_\chi = 50\,\mathrm{MPa}$

Fig. 1: (a) Geometry of the periodic bar. (b-e) Analytical (dashed black lines) and numerical (solid blue and red lines) solutions of cumulated plastic slip γ_χ (red) and Laplacian term Δ_χ (blue) along a periodic strip in simple shear for a linear softening behaviour (For interpretation of the references to color in this figure caption, the reader is referred to the web version of this paper).

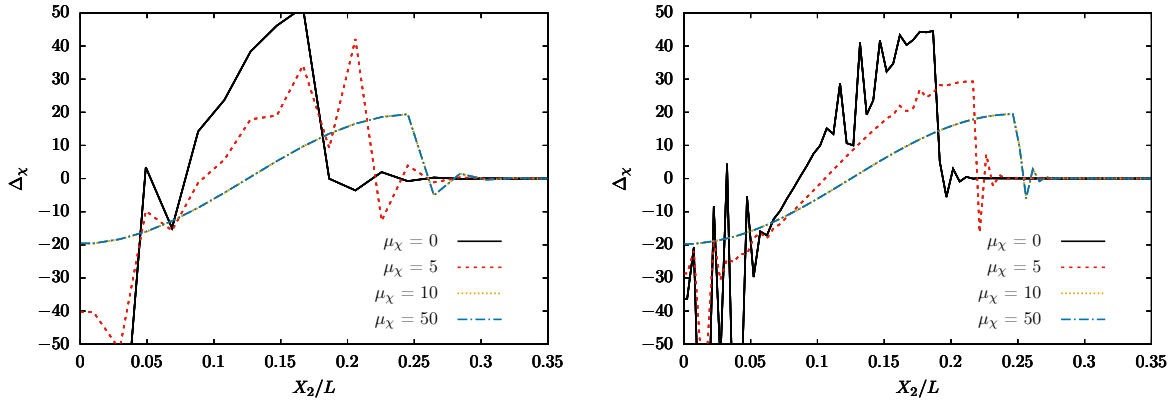

(a) $n = 51$ (b) $n = 201$

Fig. 2: Numerical solutions of the Laplacian term Δ_χ profile along a periodic strip in simple shear for several values of μ_χ. The discretization is $n = 51$ elements in (a) and $n = 201$ elements in (b).

be seen that if the value of μ_χ is not large enough, oscillations of Δ_χ are still observed even if $\mu_\chi \neq 0$. Increasing the value of μ_χ tends to smooth out the profile of Δ_χ. In this example, no clear evolution of the profile can be observed for values of μ_χ greater than or equal to 10 MPa. The results obtained with $\mu_\chi = 5$ MPa suggest that at a given value of μ_χ, a finer mesh leads to a smoother profile of the Laplacian term Δ_χ. In other words, increasing the discretization reduces the value of μ_χ required to obtain a smooth profile of Δ_χ.

5.1.2. Computational efficiency

The computational efficiency of both relaxed formulations for the rate-independent and viscous settings are compared in this section. The four possible variants (micromorphic or Lagrange multiplier approach and rate-dependent or rate-independent formulation) are used to solve the localization problem presented above. It can be shown that the shear stress τ is uniform. In order for the results to be comparable in terms of computational efficiency, the viscous stress $\tau_{vs} = \tau_0(\dot{\gamma}/\dot{\gamma}_0)^{1/n}$, for the rate-dependent setting, and the overstress $\tau_{os} = R(\dot{\gamma}/\dot{\varepsilon}_{eq})$, for the rate-independent setting, need to be calibrated in order for the numerical solution to be close to the rate-independent solution without overstress with a given precision. The macroscopic shear strain rate is chosen to be $\dot{\overline{F}}_{12} = 10^{-2}$ s^{-1}. From the analytical expression of $\tau = (\overline{F}_{12} + \tau_0/Z_e)/(1/C_{44} + 1/Z_e)$ with $1/Z_e = \lambda_0/HL$ derived in (Scherer et al., 2019) it follows that the maximum viscous stress is

$$\tau_{vs}^{max} = \tau_0 \left(\frac{2\dot{\overline{F}}_{12}}{\dot{\gamma}_0 H \left(\frac{1}{C_{44}} + \frac{1}{Z_e} \right)} \right)^{1/n} \tag{67}$$

while the rate-independent overstress is uniform and given by

$$\tau_{os} = \frac{\sqrt{3}R}{H \left(\frac{1}{C_{44}} + \frac{1}{Z_e} \right)} \tag{68}$$

$\dot{\gamma}_0$, n and R are chosen such that τ_{vs}^{max} and τ_{os} are less than 1% of τ_0. The material parameter used are summarized in Table 2. Four different values of A are chosen such that $\lambda_0/L = 2\pi\sqrt{A/|H|}/L$ takes

Table 2: Numerical values of material parameters for the comparison of computational efficiencies.

C_{44}	τ_0	H	H_χ	μ_χ	n	$\dot{\gamma}_0$	R
105 GPa	100 MPa	−10 MPa	5×10^4 MPa	50 MPa	15	$10^{30}\,\mathrm{s}^{-1}$	0.1 MPa

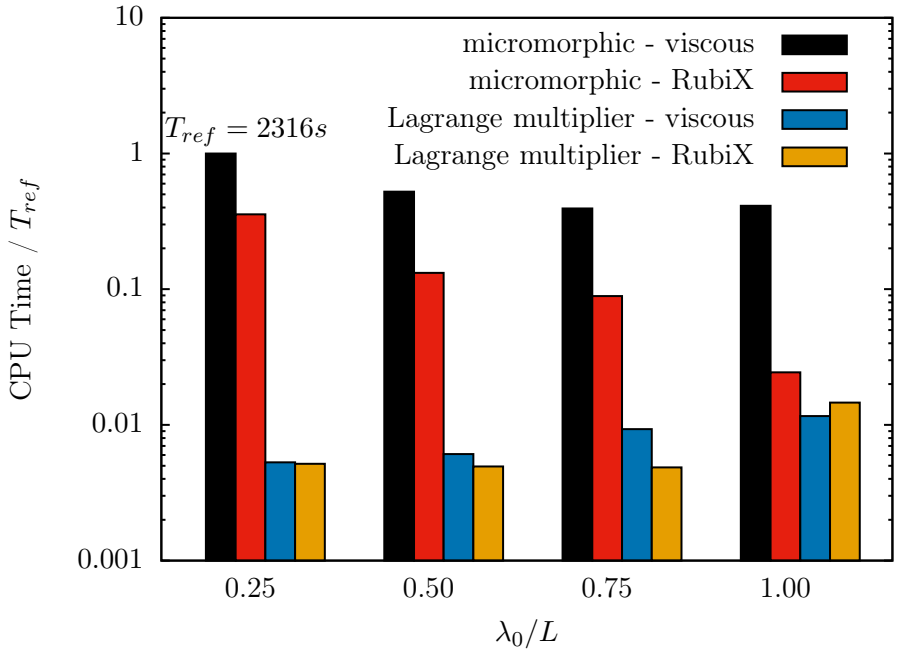

Fig. 3: Computation times for the finite element resolution of the periodic strip in simple shear and single slip for four different λ_0/L ratios and four different formulations.

the following values $[0.25; 0.5; 0.75; 1]$. The one-element thick bar is meshed with $n = 201$ quadratic elements with reduced integration (C3D20R). In the micromorphic approach each node has three displacement degrees of freedom and the linear nodes have one additional degree of freedom γ_χ. In the Lagrange multiplier approach each node has three displacement degrees of freedom and the linear nodes have two additional degrees of freedom γ_χ and λ. The number of degrees of freedom in the micromorphic simulations is $n_{DOF} = 4077$, while it is $n_{DOF} = 4485$ with the Lagrange multiplier based formulation. Results not shown here exhibit an overall discrepancy of less than 1% on the predicted numerical γ field between the four formulations after a mean shear deformation gradient of $\overline{F}_{12} = 100\%$. All simulations are also in excellent agreement with the analytical solution. Simulations were ran on a single Intel Core i7-7600U CPU. Reference computation time is $T_{ref} = 2316\,\mathrm{s}$ and corresponds to the time needed for the viscous micromorphic formulation to reach $\overline{F}_{12} = 100\%$ with $\lambda_0/L_0 = 0.25$. The relative computation times for the four different values of λ_0/L and four different formulations are displayed in Figure 3.

First, despite the slightly larger number of degrees of freedom, the computational cost reduction obtained with the Lagrange multiplier based formulation, as compared to the micromorphic

approach, is striking. In the rate-dependent setting this speedup ranges from 30 up to almost 200. In the rate-independent setting this speedup ranges between 1.5 and 70. Regarding the micromorphic implementation only, the speedup obtained with the rate-independent setting, as compared to the viscous setting, ranges from more than 2.5 to about 17 as the ratio λ_0/L increases. Furthermore, regarding the Lagrange multiplier formulation only, the rate-dependent and rate-independent settings have very similar computational performances. The rate-independent setting is slightly more efficient for the lowest λ_0/L ratios, while on the contrary the rate-dependent formulation performs better at $\lambda_0/L = 1$.

The rate of convergence in the local integration scheme was checked for the micromorphic and Lagrange multiplier approaches. Both methods display a very similar rate of convergence that is very close to the quadratic bound of a Newton scheme. The gap of performances between the two implementations is in fact attributed to the poor conditioning of the local Jacobian matrix when the penalization modulus H_χ is taken large. Pre-conditioning techniques could be applied in order to enhance the performances of the micromophic approach.

As this work proceeds, the rate-dependent setting is adopted and results obtained with micromorphic and Lagrange multiplier approaches are compared. As already discussed by (Cordero et al., 2010) micromorphic and strict strain gradient formulations, such as the Lagrange multiplier based formulation, are indeed not always strictly equivalent. Therefore the choice of the appropriate formulation should not only be motivated by the computational efficiency but also by the desired scaling law.

5.2. Size effects in torsion tests

The torsion of single and polycrystal wires has been the subject of intensive experimental and computational research. Nouailhas and Cailletaud (1995) discovered that the torsion of a single crystal bar or tube is characterized by two types of strain gradients: a radial gradient from the center to the outer surface due to the loading, but also a gradient along the outer circumference due to the anisotropic activation of slip systems. This was observed experimentally by means of strain gauges placed along the circumference (Forest et al., 1996). The transition from single to polycrystals for microwires of increasing diameters was computed using finite element crystal plasticity in (Quilici et al., 1998) and more recently in (Bayerschen, 2016). The size–dependent torsion of FCC single crystal bars is investigated below by means of the proposed micromorphic and strain gradient plasticity models.

5.2.1. Problem setup

Simulations are performed with a single crystal cylindrical microwire of diameter $D = 2R_0$ meshed with elements that are quadratic for displacements degrees of freedom and linear for γ_χ and λ. Quadratic shape function are used for displacements degrees of freedom because they are known to provide better interpolation accuracy than linear shape functions. Furthermore, quadratic elements are also known to be less subject to locking issues. However linear shape functions are used for γ_χ and λ in order to limit the number of degrees of freedom. It is in fact assumed that plastic deformations vary less rapidly than displacements, in such a way that linear shape functions give sufficient precision

to interpolate accumulated plastic slip. With the formalism developed in this work quadratic shape function for γ_χ and λ could also have been used. As reduced integration involves a lesser number of integration points than full integration, 20-node brick elements with reduced integration possessing 8 Gauss points (instead of 27 for full integration) are used. Reducing the number of integration points clearly decreases the accuracy of the integration, but it also reduces the computational cost. Furthermore, reduced integrated elements are known to be less stiff than fully integrated elements. Therefore, reduced integration is often recommended in order to avoid the problem of locking and possible oscillations. Yet, reduced integration can lead to hourglassing issues when the element stiffness matrix is zero. Several ways to address hourglassing have been proposed in literature (Belytschko et al., 1984): inserting an artificial stiffness to the hourglass deformation modes, inserting an artificial viscosity, refining the mesh, *etc.* In this work methods to prevent hourglass were not used because no significant hourglass modes could be observed in the simulations which are presented below.

The bottom face of the microwire is clamped while the top surface undergoes a rigid body rotation around the wire axis. The lateral faces are kept traction free, which means that $\underline{\boldsymbol{T}} = 0$ and $M = 0$ from Eq. (6) and (7). Two orientations of the single crystal are considered: <001> and <111> aligned with the microwire axis. The geometry and the boundary conditions are as shown in Figure 4. The Cartesian coordinate system is chosen for the two microwire single crystals (later respectively denoted <001> and <111>) such that

$$\underline{\boldsymbol{X}}_1 = [110] \quad \underline{\boldsymbol{X}}_2 = [1\bar{1}0] \quad \underline{\boldsymbol{X}}_3 = [001] \tag{69}$$

and

$$\underline{\boldsymbol{X}}_1 = [\bar{1}\bar{1}2] \quad \underline{\boldsymbol{X}}_2 = [1\bar{1}0] \quad \underline{\boldsymbol{X}}_3 = [111] \tag{70}$$

respectively.

Face-centered cubic (FCC) single crystal microwires are simulated. The hardening laws per slip system are based on the evolution of usual scalar dislocation densities. The hardening term accounts for lattice friction and dislocation interactions (Kubin et al., 2008). The critical resolved shear stress (CRSS) is taken as:

$$\tau_c^s = \tau_0 + \mu \sqrt{\sum_{u=1}^{12} a^{su} r^u} \tag{71}$$

where τ_0 is the thermal component of the CRSS due to lattice friction, r^u denotes adimensional dislocation density ($r^u/b^2 = \rho^u$ is the usual dislocation density, *i.e.* the length of dislocation lines per unit volume, b is the norm of the dislocation Burgers vector $\underline{\boldsymbol{b}}$), μ is the shear modulus, and a^{su} is a matrix describing interactions between dislocations. Such an hardening behaviour is standard in the literature, but the link to a free energy potential ψ_h remains an open question. The evolution

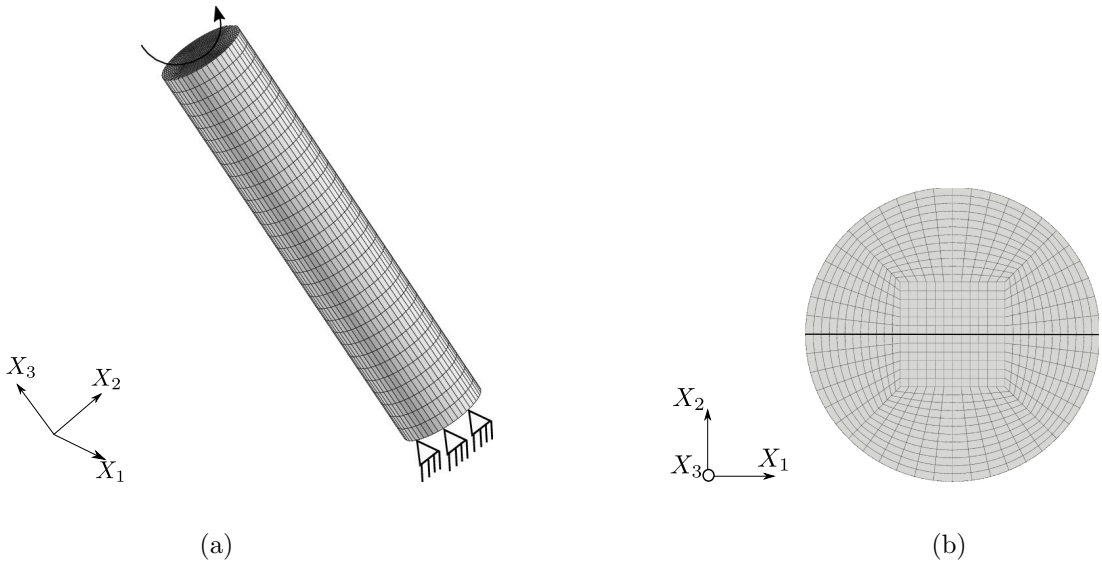

Fig. 4: Microwire torsion (a) boundary conditions (b) example mesh from the top side in which the black line represents an initial material line. For the <001> crystal orientation the black line is oriented along a <110> direction. For the <111> crystal orientation it is oriented along a $<11\bar{2}>$ direction.

Table 3: Numerical values of material parameters for the simulation of microwires in torsion.

C_{11}	C_{12}	C_{44}	τ_0	n	$\dot{\gamma}_0$	μ	G_c	κ
259.6 GPa	179 GPa	109.6 GPa	320 MPa	20	$10^{33}\,\mathrm{s}^{-1}$	77.2 GPa	10.4	42.8

r_0^s	a^{su}	b^{su} $(s \neq u)$	b^{uu}	H_χ	μ_χ
5.38×10^{-11}	0.124	1	0	10^4 MPa	10^3 MPa

equation for the adimensional dislocation density r^s

$$\dot{r}^s = |\dot{\gamma}^s| \left(\frac{\sqrt{\sum_{u=1}^{12} b^{su} r^u}}{\kappa} - G_c r^s \right) \tag{72}$$

accounts for multiplication and annihilation of dislocations. The parameter κ is proportional to the number of obstacles crossed by a dislocation before being immobilized, G_c is the critical distance controlling the annihilation of dislocations with opposite signs, and b^{su} describes the interactions between dislocations. The structures of the matrices a^{su} and b^{su} are given in (Ling et al., 2018) for FCC crystals. Cubic elasticity is considered. The wrought Inconel 718 material parameters at room temperature used for the numerical simulation are given in Table 3. r_0^s denotes the initial value of the adimensional dislocation density, which is assumed to be the same for all slip systems. The various intrinsic length scale to diameter ratios ($\ell/2R_0$) considered in the simulations are given in Table 4.

Table 4: Numerical values of $\ell/2R_0$ ratios for the simulation of microwires in torsion.

$\ell/2R_0$ <001>	0.03	0.07	0.10	0.31	0.44	0.54
$\ell/2R_0$ <111>	0.03	0.08	0.11	0.35	0.50	0.61

5.2.2. Results and discussion

Figure 5 and 6 show the accumulated plastic strain fields in the deformed configuration for FCC single crystals with wire axis parallel to <001> and <111> respectively. A cross section of each sample is illustrated in Figure 5 and 6. The radial and circumferential plastic strain gradients are clearly visible. A four-fold pattern is observed for the <001> specimen with maximum plastic strain values along <100> directions. A six-fold pattern is observed for the <111> specimen with maximum plastic strain values along $<11\bar{2}>$ directions. The overall curves are presented using normalized torque T/R_0^3 as a function of surface strain γ_R defined as

$$\gamma_R = kR_0 \tag{73}$$

where k is the applied twist per unit length (θ/L). They are given in Figure 7 for the two single crystal orientations <001> and <111> using classical crystal plasticity. The <001> crystal orientation is found to be significantly stronger than the <111> wire. The orientation of the crystal to the loading direction causes different slip activity and results in different mechanical responses. The twist angle at the cross-section of the microwire is calculated as $\theta_h = \theta h/L$, where h is the height from the bottom end. The initial material line for <001> and <111> crystal orientation is shown in Figure 4b. The rotation of material line with increasing surface strain is as shown in Figure 5 and 6. The response of the micromorphic wire is also provided in Figure 7 for comparison for a given internal length value. In the micromorphic approach, the penalty parameter H_χ is chosen sufficiently large for γ_{cum} and γ_χ to almost coincide. The chosen value of H_χ in the simulation is 10^4 MPa. The intrinsic length scale (ℓ) considered in the simulation is defined as $\ell = \sqrt{A/|H|}$ as proposed in (Ling et al., 2018), where H is the initial equivalent linear hardening modulus. H is estimated by performing uniaxial tensile test on one element as proposed in (Ling, 2017). Its value is given by the ratio of τ^s and γ^s for one activated slip system at the beginning of its activation. Thus the estimated H values for <001> and <111> crystal orientation are 2500 MPa and 2000 MPa respectively. The intrinsic length scale can be varied by varying the constitutive parameter A. The various values of A and of the intrinsic length scale to diameter ratio $(\ell/2R_0)$ of microwire are given in the Table 4. The micromorphic response in Figure 7 exhibits a linear hardening of the wire in contrast to the saturated classical crystal plasticity response. The magnitude of the slope depends on the value of the internal length as demonstrated in the following.

The effect of different ratios $\ell/2R_0$ on the size effects in torsion microwires has been studied for the two models considered in this work, namely the micromorphic and strain gradient plasticity formulations. The torque *vs* surface strain curves of the micromorphic model are compared with

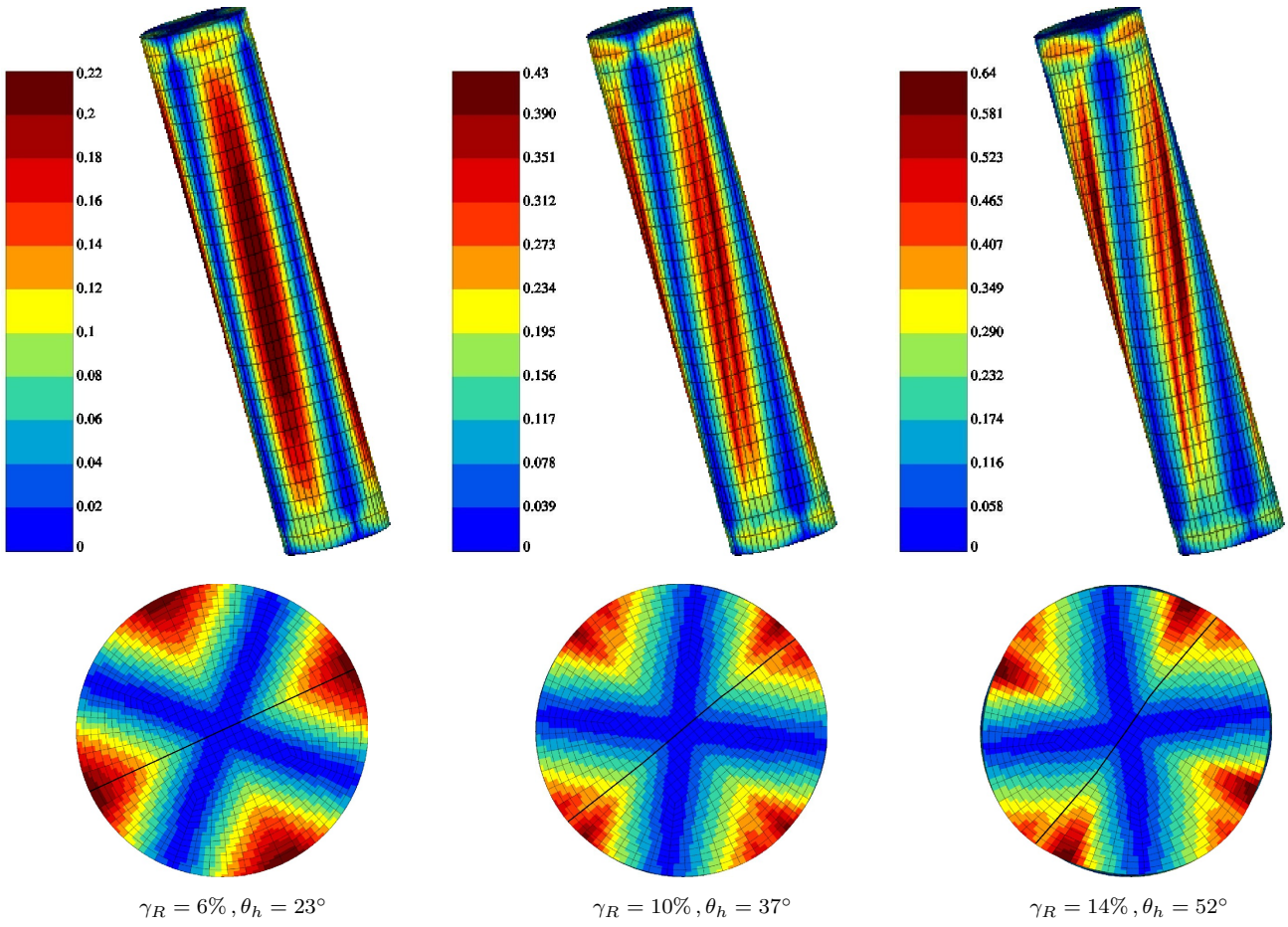

$\gamma_R = 6\%\,, \theta_h = 23^\circ$ $\gamma_R = 10\%\,, \theta_h = 37^\circ$ $\gamma_R = 14\%\,, \theta_h = 52^\circ$

Fig. 5: Cumulative plastic strain (γ_{cum}) field in FCC single crystal for <001> crystal orientation in classical crystal plasticity with respect to deformed configuration. The rotation of material line shown in Fig. 4b with increasing surface strain is shown by a black line on the cross-section.

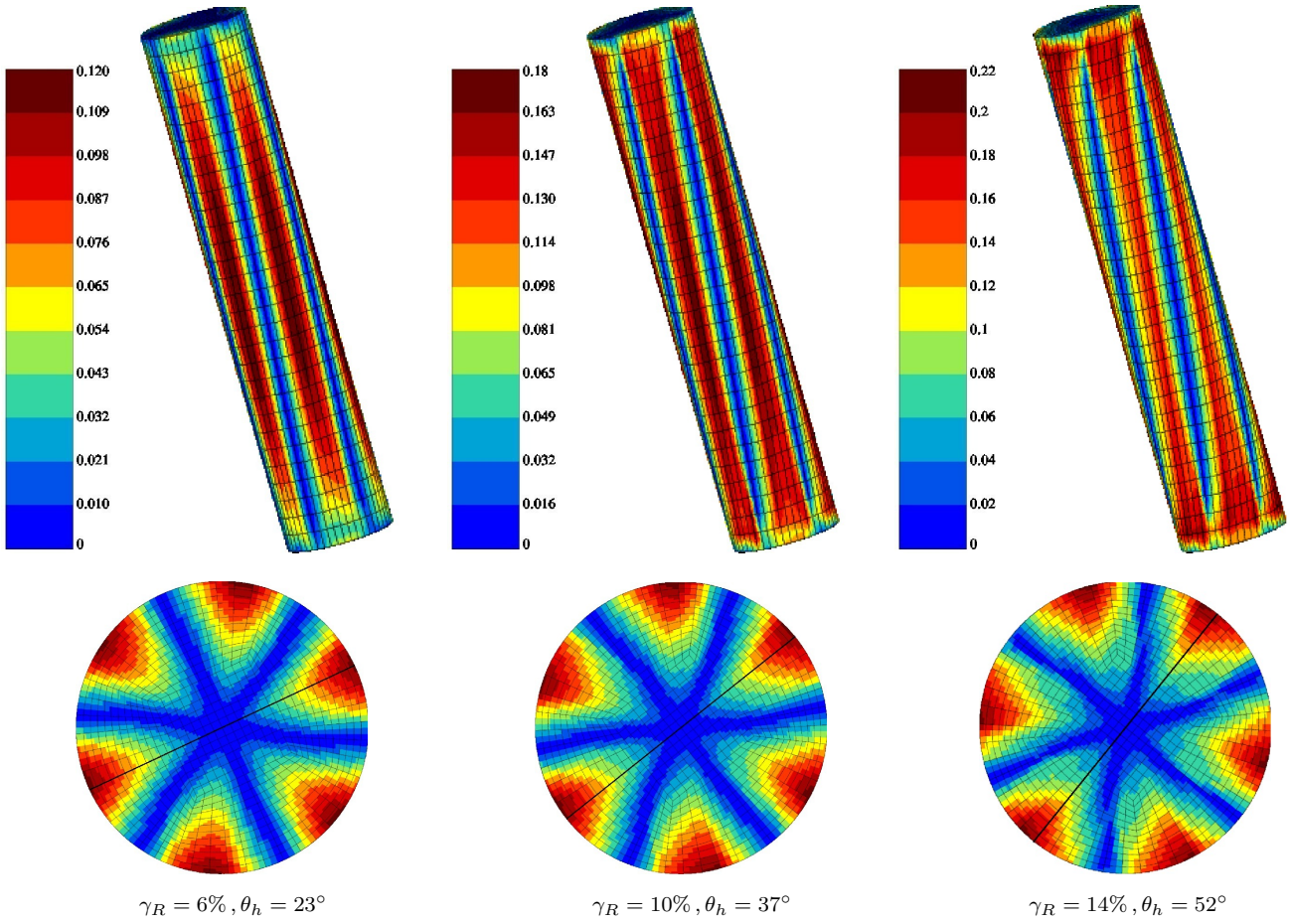

$\gamma_R = 6\%\,, \theta_h = 23^\circ$ $\gamma_R = 10\%\,, \theta_h = 37^\circ$ $\gamma_R = 14\%\,, \theta_h = 52^\circ$

Fig. 6: Cumulative plastic strain (γ_{cum}) field in FCC single crystal for <111> crystal orientation in classical crystal plasticity with respect to deformed configuration. The material line shown in Figure 4b and its rotation with increasing surface strain are shown by a black line on the cross-section.

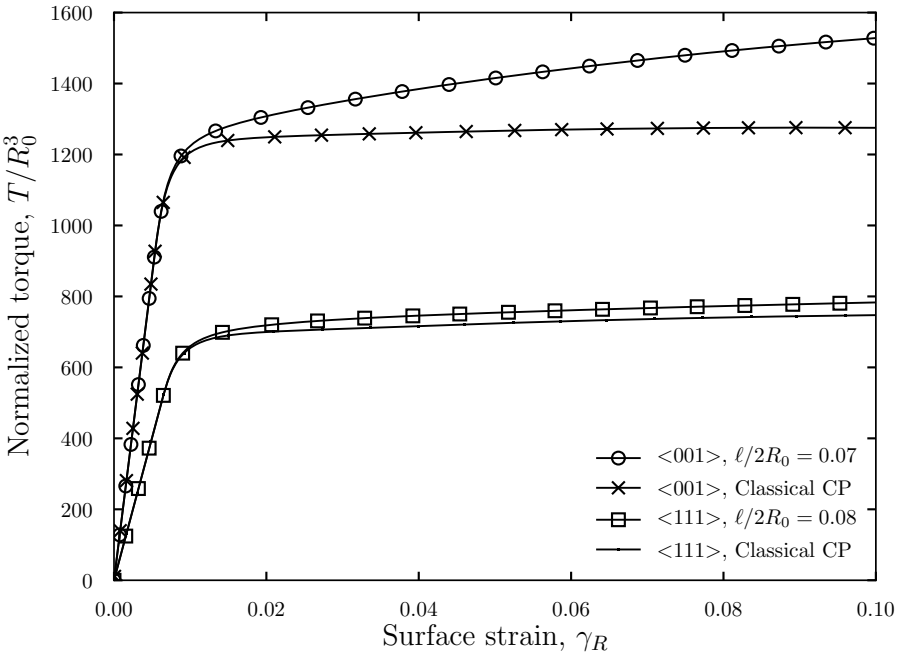

Fig. 7: Shear stress *vs* surface strain in FCC single crystal wires for <001> and <111> crystal orientation using classical crystal plasticity and micromorphic models.

the Lagrange multiplier based model. The cumulative plastic strain (γ_{cum}) fields for different $\ell/2R_0$ of microwire ($\ell/2R_0 = 0.03, 0.07, 0.10$ and 0.44 for <001> and $\ell/2R_0 = 0.03, 0.08, 0.11$ and 0.50 for <111> crystal orientation) obtained using both models are shown in Figure 8 and 9. It can be seen that, for low and intermediate values of the ratio $\ell/2R_0$, the two models predict the same accumulated plastic slip fields. In contrast, for the larger value $\ell/2R_0 = 0.31$, the circumferential gradient has almost disappeared according to the Lagrange multiplier based model whereas it is still present in the micromorphic simulation. Increasing the length scale for a fixed wire diameter leads to a strong decrease of the plastic strain gradient. This can be attributed to the fact that the energetic cost of plastic strain gradient increases with ℓ and the free energy of the sample is minimum for a limited value of the gradient. These observations are valid for both orientations <001> and <111>. It is remarkable that the four-fold and six-fold patterns disappear for large enough internal length scale values.

The corresponding torque *vs* surface strain curves are provided in Figure 10 and 11. They clearly show the size-dependent hardening effect for both models. For small and intermediate values of the internal length, the micromorphic and Lagrange multiplier models are found to deliver the same overall responses. This result is expected since the value of penalty parameter in the micromorphic model has been chosen so as to ensure such a correspondence. However, keeping the same value of the penalty parameter H_χ and increasing the internal length, or equivalently the value of the parameter A, leads to a saturation of the torque-shear strain curve for the micromorphic model. In contrast, the Lagrange multiplier based model predicts ever increasing hardening. Figure 10a and 11a show almost the same

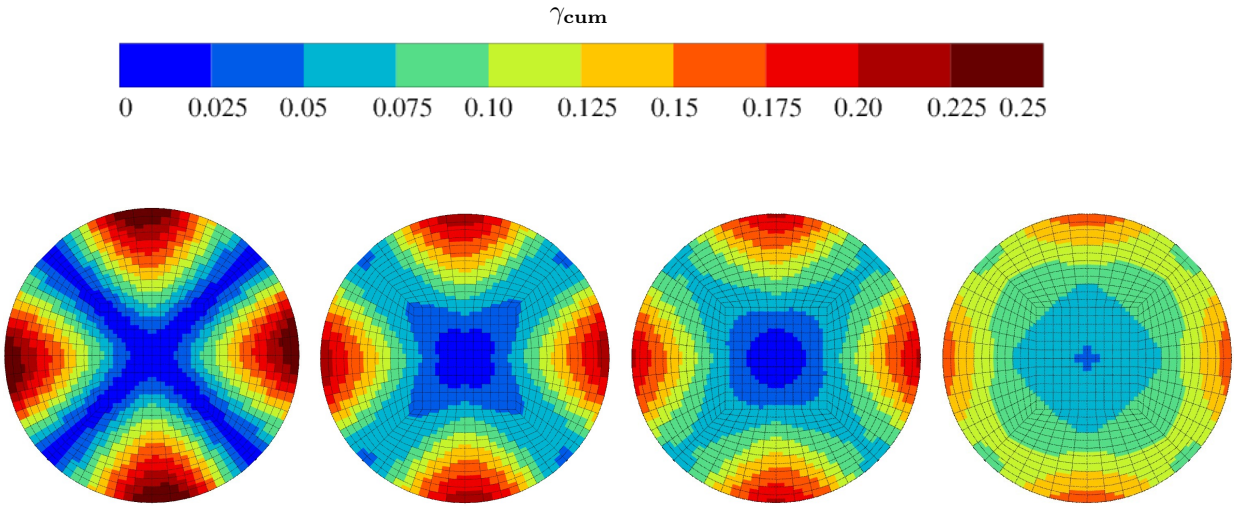

(a)

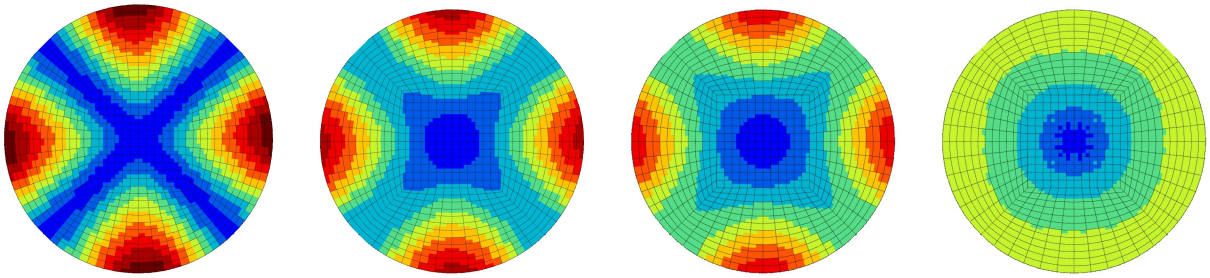

$\ell/2R_0 = 0.03$ $\ell/2R_0 = 0.07$ $\ell/2R_0 = 0.10$ $\ell/2R_0 = 0.31$

(b)

Fig. 8: Cumulative plastic strain distribution in FCC single crystal for <001> crystal orientation for different values of ratio $\ell/2R_0$ using (a) micromorphic (b) Lagrange multiplier models at surface strain of 0.08 (fields reported on the reference configuration).

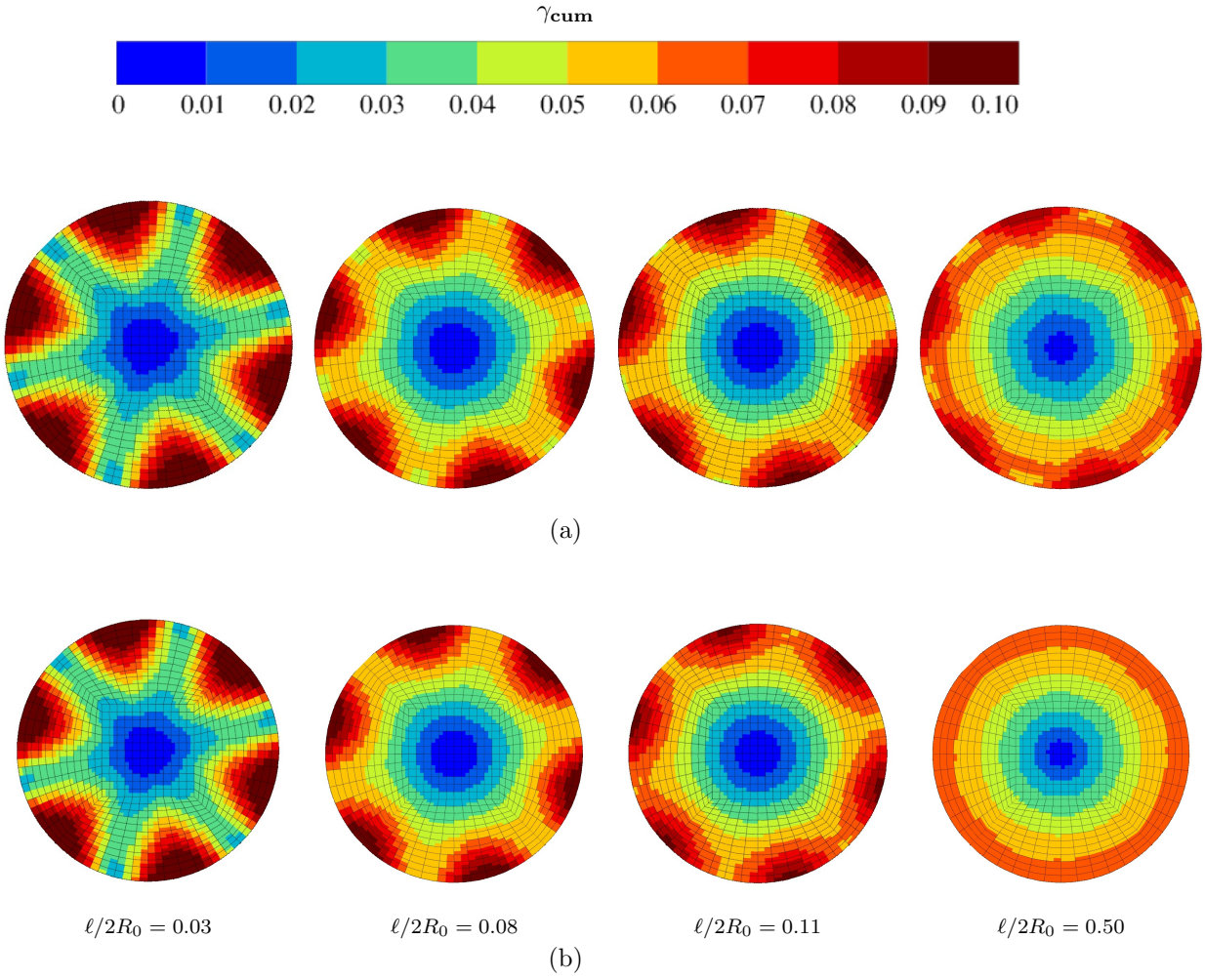

Fig. 9: Cumulative plastic strain distribution in FCC single crystal for <111> crystal orientation for different values of ratio $\ell/2R_0$ using (a) micromorphic (b) Lagrange multiplier models at surface strain of 0.08 (fields reported on the reference configuration).

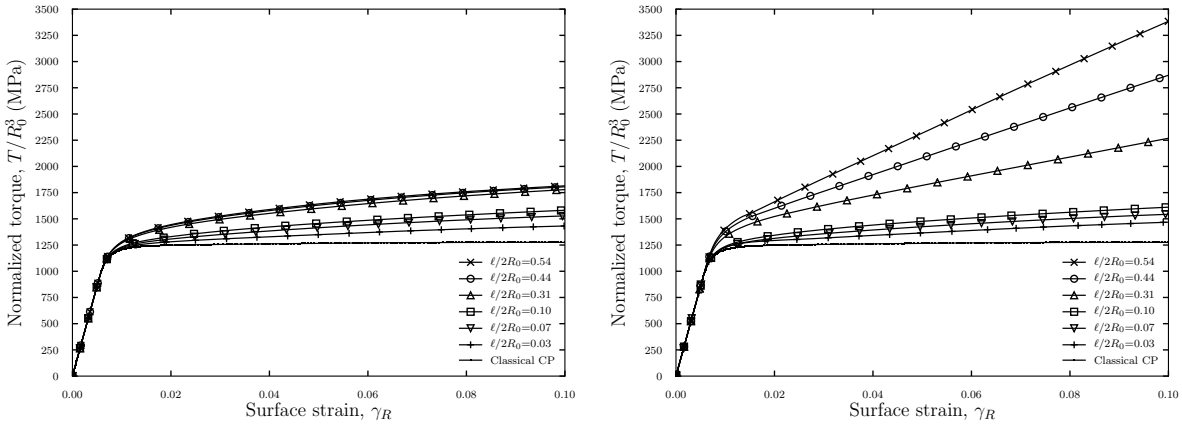

Fig. 10: Normalized torque *vs* surface strain curves for FCC <001> crystal orientation for different values of ratio $\ell/2R_0$ using (a) micromorphic (b) Lagrange multiplier models.

micromorphic response for the two largest $\ell/2R_0$ values whereas distinct curves are obtained with the Lagrange multiplier approach, see Figure 10b and 11b. This saturation of size effects predicted by a micromorphic formulation has already been demonstrated analytically for the microcurl theory by Cordero et al. (2010) in the case of periodic shearing of a laminate at small strains and small rotations. The present new results show that this feature also exists at large strains for torsion. These observations apply to both orientations <001> and <111>. The strongest additional hardening effect is obtained when the internal length takes values comparable to the wire diameter, as expected.

The predictions of the Lagrange multiplier based formulation can be considered in fact as the limit case when the penalty modulus H_χ goes to infinity in the micromorphic formulation. The predictions obtained with the micromorphic formulation for several values of H_χ are plotted in Figure 12. As H_χ rises the prediction of the micromorphic formulation goes closer to the prediction obtained with the Lagrange multiplier based formulation. However increasing H_χ builds up drastically the computation time since the penalization becomes very stiff. In practice, one could use the penalty term H_χ in the micromorphic formulation as a parameter to fit the scaling law measured in experiments. This possibility was discussed for micromorphic and Cosserat models in (Cordero et al., 2010). Such a parametrization is however not possible with the Lagrange multiplier based formulation. Nevertheless saturation of the scaling law can also be achieved, with both formulations, by using a more elaborate free energy potential associated to gradient terms. The rather simple quadratic form used in this study can indeed be modified in order to obtain more physically relevant scaling laws.

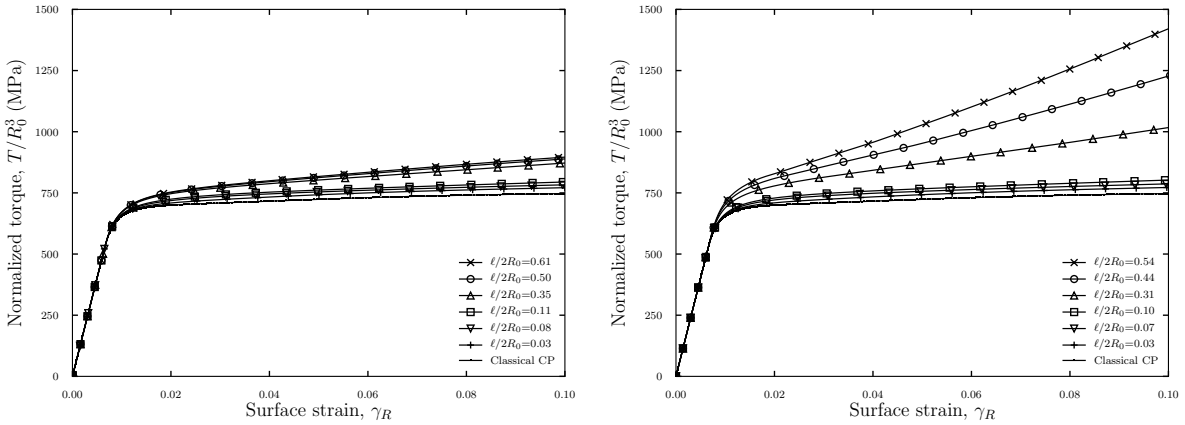

(a) (b)

Fig. 11: Normalized torque vs surface strain curves for FCC <111> crystal orientation for different values of ratio $\ell/2R_0$ using (a) micromorphic (b) Lagrange multiplier models.

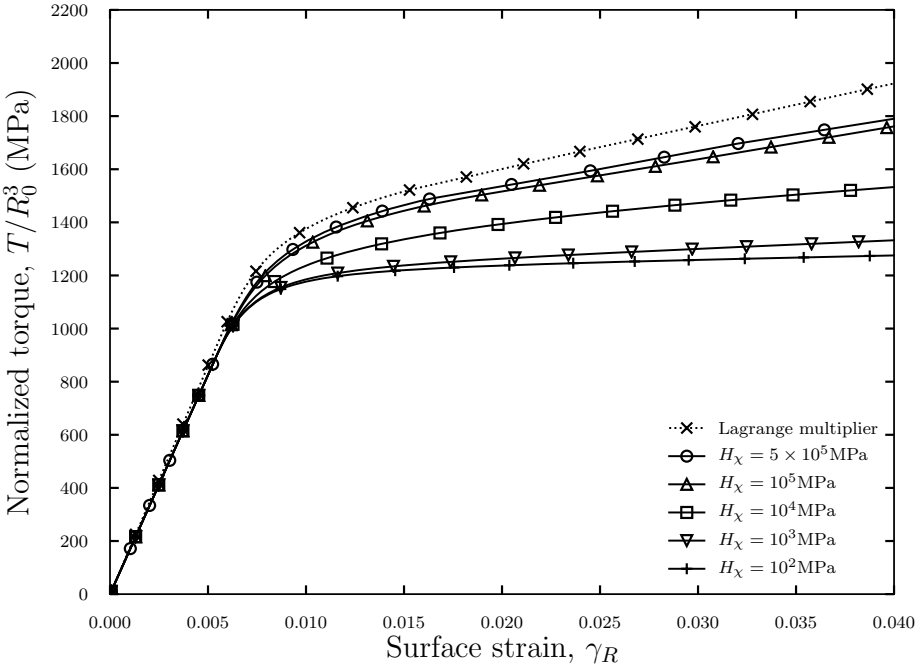

Fig. 12: Normalized torque *vs* surface strain curves for FCC <001> crystal orientation for different values of H_χ and for $\ell/2R_0 = 0.44$.

5.3. Size effects in ductile fracture: void growth and coalescence

Porous unit-cell simulations are commonly used to assess the mechanisms of void growth and void coalescence which play a major role in the ductile failure of metallic materials. Voids can nucleate at defects such as inclusions and precipitates by cracking or debonding of these defects. Voids may also be induced by other mechanisms such as irradiation in nuclear materials. In all these cases voids are sub-crystalline imperfections. Following the pioneering work of Hori and Nemat-Nasser (1988a,b) recent numerical studies have considered voids embedded in FCC (Ling et al., 2016) and HCP (Selvarajou et al., 2019) single crystals. In addition, Hussein et al. (2008); Borg et al. (2008b); Zhao et al. (2009) have analyzed the size effects predicted by strain gradient plasticity, dislocations dynamics and molecular dynamics respectively, in plates containing cylindrical holes. Recently Ling et al. (2018) performed the first size-dependent 3D porous single crystal unit-cell simulations where the micromorphic crystal plasticity formulation presented in Section 3.1 was used. Similar unit-cell simulations are reproduced with the Lagrange multiplier based formulation presented in Section 3.2 and compared to the results obtained by Ling et al. (2018).

5.3.1. Problem setup

An initially spherical void of radius R_0 is placed at the center of a cube of size L_0 as presented in Figure 13a. The matrix material surrounding the void is a FCC single crystal (later denoted <100>) such that

$$\underline{\boldsymbol{X}}_1 = [100] \quad \underline{\boldsymbol{X}}_2 = [010] \quad \underline{\boldsymbol{X}}_3 = [001] \tag{74}$$

Therefore, for symmetry reasons only one eighth of the porous unit-cell is considered. Figure 13b shows the corresponding finite element mesh for a void volume fraction $f_0 = (4/3)\pi(R_0/L_0)^3 = 1\%$. Quadratic (resp. linear) shape functions are used for the displacement (resp. micro-slip γ_χ and Lagrange multiplier λ) degrees of freedom. Elements with reduced integration are used. A triaxial axisymmetric loading is applied by prescribing displacement boundary conditions on the inner faces of the cube at $X_1 = 0$, $X_2 = 0$, $X_3 = 0$ and outer faces at $X_1 = L_0/2$, $X_2 = L_0/2$, $X_3 = L_0/2$

$$U_1(X_1 = 0, X_2, X_3) = 0 \qquad U_1(X_1 = L_0/2, X_2, X_3) = U_1(t) \tag{75}$$

$$U_2(X_1, X_2 = 0, X_3) = 0 \qquad U_2(X_1, X_2 = L_0/2, X_3) = U_2(t) \tag{76}$$

$$U_3(X_1, X_2, X_3 = 0) = 0 \qquad U_3(X_1, X_2, X_3 = L_0/2) = U_3(t) \tag{77}$$

External forces F_1, F_2 and F_3 are respectively associated to U_1, U_2 and U_3. The macroscopic Cauchy stress components Σ_{11}, Σ_{22} and Σ_{33} are defined by

$$\Sigma_{11} = \frac{4F_1}{(L_0 + 2U_2)(L_0 + 2U_3)} \qquad \Sigma_{22} = \frac{4F_2}{(L_0 + 2U_1)(L_0 + 2U_3)} \qquad \Sigma_{33} = \frac{4F_3}{(L_0 + 2U_1)(L_0 + 2U_2)} \tag{78}$$

A macroscopic strain rate $\dot{\overline{F}}_{11} = 10^{-4}$ s^{-1} is imposed along the $\underline{\boldsymbol{X}}_1$ direction. Displacements U_2 and U_3 are adjusted following the procedure described in Ling et al. (2016) in order to enforce a constant stress triaxiality T where

$$T = \frac{\Sigma_m}{\Sigma_{eq}} = \frac{1 + \eta_2 + \eta_3}{3\sqrt{1 - \eta_2 - \eta_3 - \eta_2\eta_3 + \eta_2^2 + \eta_3^2}} \tag{79}$$

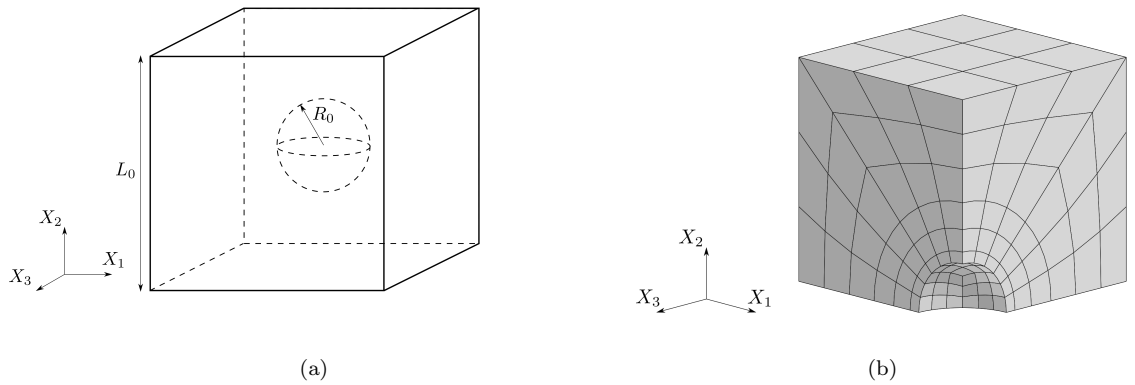

(a) (b)

Fig. 13: (a) Geometry of a cubic porous unit-cell. (b) 1/8-th of the finite element mesh for $f_0 = 1\%$. Total number of degrees of freedom is $n_{DOF} = 2767$.

with the relations $\Sigma_{22} = \eta_2 \Sigma_{11}$ and $\Sigma_{33} = \eta_3 \Sigma_{11}$. For the applied axisymmetric loading considered in this Section, the values $\eta_2 = \eta_3 = 0.625$ were chosen, corresponding to a triaxiality of 2.

The same dislocation density based hardening laws Eq. (71) and evolution equations Eq. (72) are used. Different material parameters are however considered and listed in Table 5 in order to match the material parameters used in Ling et al. (2018). Several values of A are used in order to investigate size effects. As discussed in previous section and by Ling et al. (2018) the intrinsic length scale $\ell = \sqrt{A/H}$ can be considered, where H denotes the linear hardening modulus at initiation of plastic slip in a uniaxial tensile test. The ratio ℓ/L_0 then governs the predicted size effects. For the material parameters presented in Table 5 one obtains $H = 2777\,\text{MPa}$ for the <100> crystal orientation. The numerical values of ℓ/L_0 used for the simulation of porous unit-cells are: 0, 1/300, 1/90, 1/30 and 1/3. Several values of the penalization modulus μ_χ are also considered in order to measure its impact on the macroscopic stress-strain behaviour.

5.3.2. Results and discussion

The void volume fraction f is postprocessed from the unit-cell simulations by computing the volume contained in the mesh V_{mesh} (excluding the void) and the total volume contained in the cube

Table 5: Numerical values of material parameters for the simulation of porous unit-cells.

C_{11}	C_{12}	C_{44}	τ_0	n	$\dot{\gamma}_0$	μ	G_c	κ
200 GPa	136 GPa	105 GPa	88 MPa	15	$10^{29}\,\text{s}^{-1}$	65.6 GPa	10.4	42.8

r_0^s	a_1, a_2	a_3	a_4	a_5	a_6	b_{ij} $(i \neq j)$	b_{ii}	μ_χ
5.38×10^{-11}	0.124	0.07	0.625	0.137	0.122	1	0	10^2, 10^3, 10^4 MPa

$V_{tot} = (L_0 + 2U_1)(L_0 + 2U_2)(L_0 + 2U_3)$ (including the void)

$$f = 1 - \frac{V_{mesh}}{V_{tot}} \tag{80}$$

Figure 14 plots the evolution of f with the macroscopic deformation $\overline{E}_{11} = 2U_1/L_0$ for the different ℓ/L_0 ratios considered. The results obtained with the novel Lagrange multiplier based formulation are plotted aside the results presented in (Ling et al., 2018) which were obtained with the micromorphic formulation with the same material parameters, but where the entire unit-cells were computed. It can be noted that when ℓ/L_0 vanishes, both formulations predict almost exactly the same result. Nevertheless some discrepancies become visible as ℓ/L_0 increases. This observation can be put in parallel to the discussion made in previous section. The Lagrange multiplier approach corresponds indeed to the limit case of the micromorphic formulation as H_χ approaches infinity. However in (Ling et al., 2018) for numerical efficiency reasons H_χ was taken equal to 5×10^4 MPa. Size effects obtained with both formulations are therefore in good qualitative agreement, but turn out to be more pronounced with the Lagrange multiplier setting. These effects are as follows.

With the applied loading the void volume fraction is a monotonically increasing function of $\overline{E}_{11}$. In absence of size effects (*i.e.* $\ell/L_0 = 0$) evolution of the void volume fraction does not depend on the cell size. However as ℓ/L_0 increases void volume fraction evolution becomes size-dependent. The larger the ℓ/L_0 ratio is, the slower the void volume fraction rises with macroscopic deformation. This first size effect is due to a more diffuse plastic deformation field when the intrinsic length ℓ gets closer to L_0. For the three lowest values of the ratio considered, the void volume fraction evolution displays two distinct regimes, while for the two largest ratios only one regime is visible. This two-regime evolution is characteristic of void growth and void coalescence. During the first regime, voids grow rather slowly because of overall yielding of the matrix surrounding them. At some point necking of the ligament separating voids is reached, which leads to a sudden steepening of void growth evolution. This acceleration is due to intense localization of plastic deformation inside the ligament. Onset of void coalescence by intervoid ligament necking is characterized by a transition from a triaxial to a uniaxial straining mode (Koplik and Needleman, 1988). This transition can therefore be detected by computing over time the ratio $|\Delta U_2|/|\Delta U_1|$. Coalescence can be considered to set on as soon as this ratio becomes lower than an arbitrary small critical value, say 5%. Hollow squares are plotted in Figure 14 in order to depict the macroscopic strain and void volume fraction at which coalescence begins. For the sake of clarity, coalescence onsets are only displayed for the results obtained by Ling et al. (2018). For a given characteristic length, the micromorphic and Lagrange multiplier formulations predict almost identical strain and void volume fractions at onset of coalescence. The second size effect which appears is that void growth to void coalescence transition is postponed when ℓ/L_0 is increased. This delay is due to the weaker void volume increase during the growth regime. For the two largest value of ℓ/L_0 a very flat void growth regime is observed. The quasi-absence of void growth explains why coalescence does not occur in the range of applied deformations. Necking of the intervoid ligament would indeed require larger stresses to be applied. A third size effect which can be observed is a slight increase of

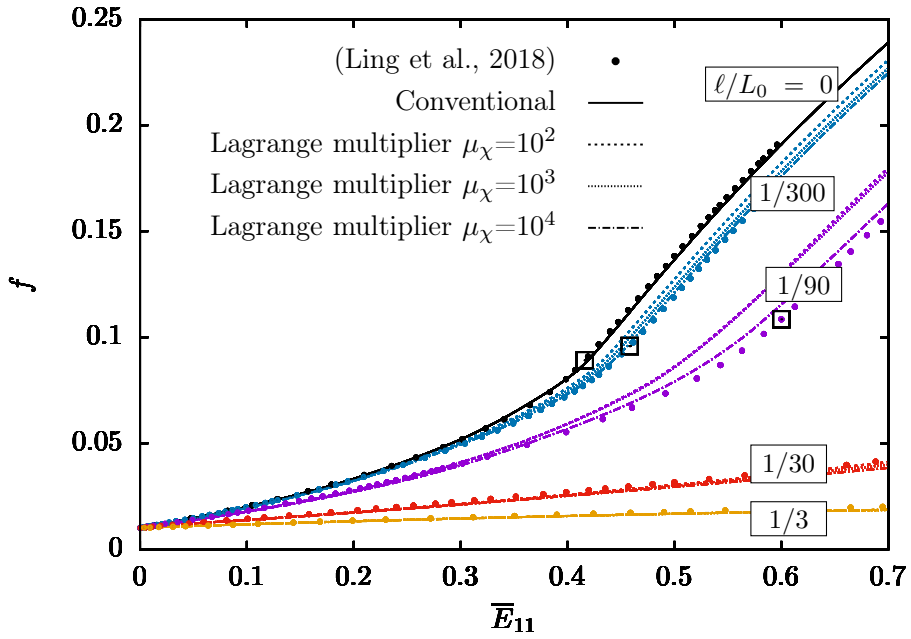

Fig. 14: Void volume fraction f evolution with respect to macroscopic deformation $\overline{E}_{11}$ for different intrinsic length to cell size ratios ℓ/L_0 obtained with the micromorphic (solid lines) and the Lagrange multiplier (dashed lines) formulations in porous unit-cell simulations with $f_0 = 0.01$ and material parameters presented in Table 5. Hollow squares denote onsets of void coalescence.

the void volume fraction at coalescence when the intrinsic length increases. This additional effect is due to the fact that size effects prevent intense localization of plastic deformation. Therefore void coalescence which occurs by localization of plastic slip in the intervoid ligament requires a larger void volume fraction in order to happen. The macroscopic stress-strain curves obtained with the Lagrange multiplier formulation are plotted in Figure 15 aside to the results obtained with the micromorphic formulation presented in Ling et al. (2018). As previously noted for void volume fraction in Figure 14, both formulations are also equivalent in terms of stress-strain behaviour when size effects are absent. However the discrepancies between both formulations observed in presence of size effects on void volume fraction evolution are also visible on the stress-strain behaviour. The void volume fraction plays indeed a detrimental role on the macroscopic stress. With low and intermediate intrinsic length scales, voids grow significantly and the material displays a two-regime stress-strain behaviour. During the first regime hardening of the matrix material dominates over softening induced by void growth. This regime is therefore characterized by an increase of the macroscopic stress despite the augmentation of f. In the second regime, softening induced by void growth overcomes the hardening capacity of the matrix leading to a macroscopic softening behaviour. However, for the largest intrinsic length, softening induced by void growth does not overcome hardening of the matrix material, thus the second stress softening regime is not observed. Hollow squares are also plotted on the stress-strain curves in order to depict onset of void coalescence. As discussed earlier, strong size effects postpone the onset of void coalescence, because of impeded void growth. As a collateral effect, it can be noted that

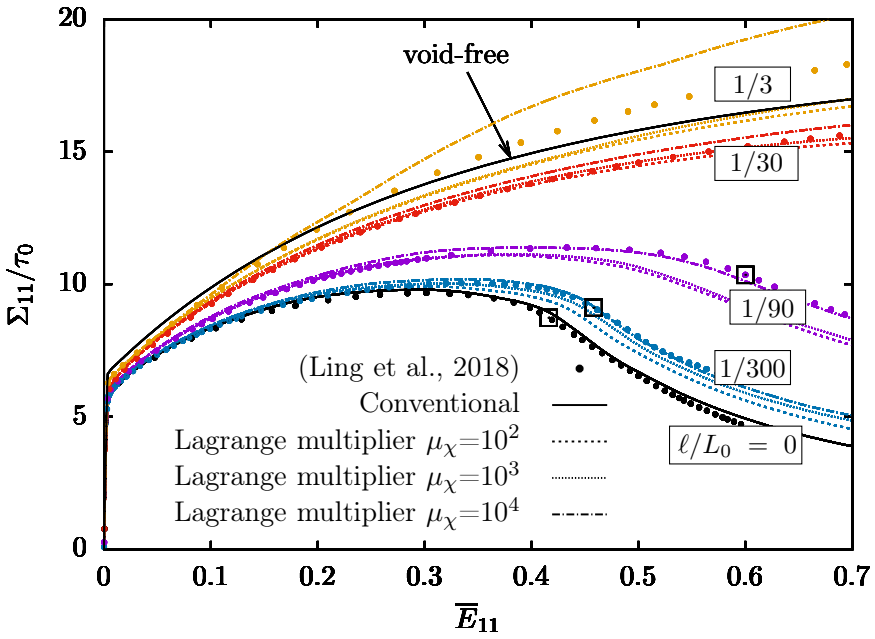

Fig. 15: Macroscopic stress-strain behaviour for different intrinsic length to cell size ratios ℓ/L_0 obtained with the micromorphic formulation (dots) by Ling et al. (2018) and the Lagrange multiplier formulation (dashed lines) in porous unit-cell simulations with $f_0 = 0.01$ and material parameters presented in Table 5. Hollow squares denote onsets of void coalescence.

the macroscopic stress at coalescence increases notably with ℓ/L_0. The influence of the penalization modulus μ_χ in the Lagrange multiplier formulation is visible in Figure 14 and 15. For the smallest characteristic length μ_χ has a rather weak impact on the void volume fraction evolution and stress behaviour. As the characteristic length increases, the importance of μ_χ rises. It can be observed that greater values of μ_χ induce a slightly slower void growth and a harder stress-strain behaviour. These effects become more visible at large strains.

The cumulated plastic strain field obtained with the Lagrange multiplier formulation with $\mu_\chi = 10^4$ MPa are displayed in Figure 16 at a macroscopic strain $\overline{E}_{11} = 0.3$ for several values of the ratio ℓ/L_0. These fields are quantitatively in excellent agreement with the results obtained by Ling et al. (2018) with the micromorphic approach. According to conventional crystal plasticity, plastic strains are predominantly localized in the vicinity of the void, in particular where the cross-section area orthogonal to the main tensile direction is minimum. Plastic anisotropy causes the presence of several soft zones, where γ_{cum} is maximum and which correspond to regions with highest Schmid factors. As the ratio ℓ/L_0 is increased the cumulated plastic slip tends to become more homogeneous across the porous unit-cell. Therefore, the maximum local value of γ_{cum} drops. In addition, the number of local maxima decreases. Three intense maxima were indeed visible with conventional crystal plasticity, while only two much less intense maxima can be observed when $\ell/L_0 = 30$.

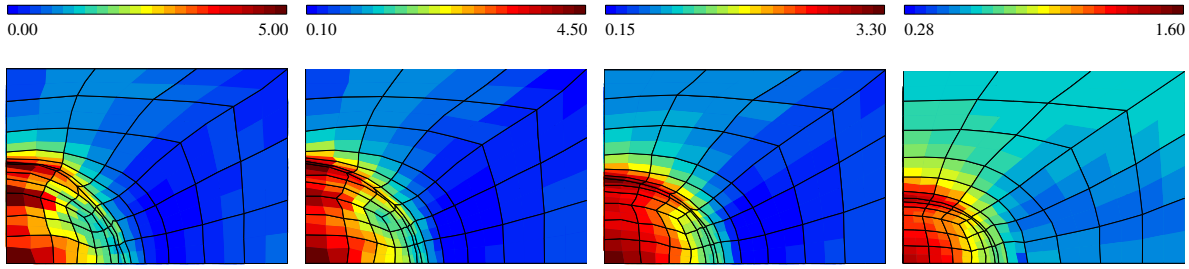

(a) Conventional (b) $\ell/L_0 = 1/300$ (c) $\ell/L_0 = 1/90$ (d) $\ell/L_0 = 30$

Fig. 16: Cumulated plastic strain fields in porous unit-cells at $\overline{E}_{11} = 0.3$ obtained with the Lagrange multiplier formulation with $\mu_\chi = 10^4$ MPa.

6. Conclusions

The major outcomes of this study can be stated as follows:

1. A Lagrange multiplier approach accounting for the nonlinearity and nonlocality coupling inherent to strain gradient plasticity was presented. It was compared to the micromorphic approach in the context of crystal plasticity. The main idea of the Lagrange multiplier approach is to enforce weakly equality between local and nonlocal variables through a Lagrange multiplier.
2. The finite element implementation of the Lagrange multiplier method was detailed. In particular tangent and Jacobian matrices were derived.
3. The computational efficiencies of the micromorphic and Lagrange multiplier formulations were compared. Rate-dependent and rate-independent crystal plasticity settings were used. A significant speedup, reaching a computational time reduction of up to a factor 200, is obtained with the Lagrange multiplier based and rate-dependent formulation compared to the micromorphic and rate-dependent formulation. Important benefits are also displayed with the rate-independent setting as compared to the viscoplastic flow rule, in particular when the micromorphic approach is considered.
4. The prediction of size effects with the micromorphic and Lagrange multiplier approaches were compared for single crystals torsion tests. It was shown that both models provide similar results for small and intermediate internal length scales. However, for larger internal length scales, the hardening due to strain gradients saturates according to the micromorphic approach. A similar saturation effect was observed on the grain size effect on the yield stress in polycrystals using the microcurl model at small strains in (Cordero et al., 2012b). The scaling law is different for the Lagrange multiplier formulation since such a saturation is not observed.
5. Advantage of the Lagrange multiplier numerical efficiency has been taken in order to perform simulations of void growth in porous unit-cells up to void coalescence. Comparison to simulations made previously with the micromorphic formulation displays a very good agreement between both formulations.

Although this model remains computationally rather expensive, the results obtained in this work suggest that simulation of structures, such as real specimens, are now within reach in more reasonable computation times. The work initiated in (Scherer et al., 2019) on the evolution of voids in a softening matrix material will be pursued by performing 3D porous unit-cell simulations by taking advantage of the enhanced computational performance of the Lagrange multiplier formulation. The advances obtained in this paper will also be coupled in a future work to recent extensions of standard crystal plasticity to ductile failure (Ling et al., 2016) and damage (Lindroos et al., 2019).

Acknowledgements

Part of the research leading to these results (in particular Section 5.2) has received funding from the European Union's Horizon 2020 research and innovation programme, Marie Sklodowska-Curie Actions, under grant agreement no. 764979, project "ENABLE", "European Network for Alloys Behaviour Law Enhancement".

7. Appendices

Appendix A. Jacobian matrix $\partial \boldsymbol{\mathcal{R}} / \partial \boldsymbol{v}_{\text{int}}$

The Jacobian matrix is needed to integrate the constitutive equations at the Gauss point level. The block form of the Jacobian matrix writes

$$\mathcal{J} = \frac{\partial \mathcal{R}}{\partial \Delta v_{\text{int}}} = \begin{pmatrix} \frac{\partial \mathcal{R}_{\underset{\sim}{\boldsymbol{E}}}}{\partial \Delta \underset{\sim}{\boldsymbol{E}}} & \frac{\partial \mathcal{R}_{\underset{\sim}{\boldsymbol{E}}}}{\partial \Delta \gamma^p} & \frac{\partial \mathcal{R}_{\underset{\sim}{\boldsymbol{E}}}}{\partial \Delta r^q} & \frac{\partial \mathcal{R}_{\underset{\sim}{\boldsymbol{E}}}}{\partial \Delta \gamma_{cum}} \\ \frac{\partial \mathcal{R}_{\gamma^s}}{\partial \Delta \underset{\sim}{\boldsymbol{E}}} & \frac{\partial \mathcal{R}_{\gamma^s}}{\partial \Delta \gamma^p} & \frac{\partial \mathcal{R}_{\gamma^s}}{\partial \Delta r^q} & \frac{\partial \mathcal{R}_{\gamma^s}}{\partial \Delta \gamma_{cum}} \\ \frac{\partial \mathcal{R}_{r^s}}{\partial \Delta \underset{\sim}{\boldsymbol{E}}} & \frac{\partial \mathcal{R}_{r^s}}{\partial \Delta \gamma^p} & \frac{\partial \mathcal{R}_{r^s}}{\partial \Delta r^q} & \frac{\partial \mathcal{R}_{r^s}}{\partial \Delta \gamma_{cum}} \\ \frac{\partial \mathcal{R}_{\gamma_{cum}}}{\partial \Delta \underset{\sim}{\boldsymbol{E}}} & \frac{\partial \mathcal{R}_{\gamma_{cum}}}{\partial \Delta \gamma^p} & \frac{\partial \mathcal{R}_{\gamma_{cum}}}{\partial \Delta r^q} & \frac{\partial \mathcal{R}_{\gamma_{cum}}}{\partial \Delta \gamma_{cum}} \end{pmatrix} \tag{A.1}$$

- Derivatives of $\mathcal{R}_{\underset{\sim}{\boldsymbol{E}}}$

$$\mathcal{R}_{\underset{\sim}{\boldsymbol{E}}} = \Delta \underset{\sim}{\boldsymbol{E}} - \Delta \underset{\sim}{\boldsymbol{F}} . \underset{\sim}{\boldsymbol{F}}^{-1} . \underset{\sim}{\boldsymbol{E}} + \underset{\sim}{\boldsymbol{E}} . \left(\sum_{s=1}^{N} \Delta \gamma^s \underset{\sim}{\boldsymbol{N}}^s \right) \tag{A.2}$$

$$\frac{\partial \mathcal{R}_{\underset{\sim}{\boldsymbol{E}}}}{\partial \Delta \underset{\sim}{\boldsymbol{E}}} = \underline{\underline{\mathbf{1}}} - (\Delta \underset{\sim}{\boldsymbol{F}} . \underset{\sim}{\boldsymbol{F}}^{-1}) \underline{\otimes} \underline{\underline{\mathbf{1}}} + \underline{\underline{\mathbf{1}}} \underline{\otimes} \left(\sum_{s=1}^{N} \Delta \gamma^s \underset{\sim}{\boldsymbol{N}}^s \right)^T \tag{A.3}$$

$$\frac{\partial \mathcal{R}_{\underset{\sim}{\boldsymbol{E}}}}{\partial \Delta \gamma^p} = \underset{\sim}{\boldsymbol{E}} . \underset{\sim}{\boldsymbol{N}}^p \qquad \frac{\partial \mathcal{R}_{\underset{\sim}{\boldsymbol{E}}}}{\partial \Delta r^q} = 0 \qquad \frac{\partial R_{\underset{\sim}{\boldsymbol{E}}}}{\partial \Delta \gamma_{cum}} = 0 \tag{A.4}$$

- Derivatives of $\mathcal{R}_{\gamma^s}$

$$\mathcal{R}_{\gamma^s} \quad = \Delta\gamma^s - \Delta\Gamma\Phi^s\left(|\tau^s| - \left\langle \tau_c^s - \tfrac{\rho_{\sharp}}{\rho_0}\left(\Delta_\chi - \mu_\chi\gamma_{cum}\right)\right\rangle\right)\mathrm{sign}\left(\tau^s\right) \tag{A.5}$$

$$\frac{\partial\mathcal{R}_{\gamma^s}}{\partial\Delta\underset{\sim}{\boldsymbol{E}}} = -\Delta\Gamma\frac{\partial\Phi^s}{\partial\tau^s}\frac{\partial\tau^s}{\partial\underset{\sim}{\boldsymbol{\Pi}}^M} : \frac{\partial\underset{\sim}{\boldsymbol{\Pi}}^M}{\partial\underset{\sim}{\boldsymbol{C}}^e} : \frac{\partial\underset{\sim}{\boldsymbol{C}}^e}{\partial\underset{\sim}{\boldsymbol{E}}} : \frac{\partial\underset{\sim}{\boldsymbol{E}}}{\partial\Delta\underset{\sim}{\boldsymbol{E}}}\mathrm{sign}\left(\tau^s\right) \qquad \underset{\sim}{\boldsymbol{C}}^e = \underset{\sim}{\boldsymbol{E}}^T.\underset{\sim}{\boldsymbol{E}} \tag{A.6}$$

with

$$\frac{\partial\Phi^s}{\partial\tau^s} = \frac{\partial\Phi^s}{\partial f^s}\frac{\partial f^s}{\partial\tau^s} = \mathrm{sign}\left(\tau^s\right)\Phi^{s'} \qquad \Phi^{s'} = \begin{cases} \Phi_{RD}^{s'} = \dfrac{n}{\tau_0^n}\left\langle\dfrac{f^s}{\tau_0}\right\rangle^{n-1} \\ \Phi_{RI}^{s'} = 1/R \end{cases} \qquad \frac{\partial\tau^s}{\partial\underset{\sim}{\boldsymbol{\Pi}}^M} = \underset{\sim}{\boldsymbol{N}}^s \tag{A.7}$$

$$\frac{\partial\underset{\sim}{\boldsymbol{\Pi}}^M}{\partial\underset{\sim}{\boldsymbol{C}}^e} = \frac{\partial\left[\underset{\sim}{\boldsymbol{C}}^e.\left(\underset{\approx}{\boldsymbol{C}} : \frac{1}{2}(\underset{\sim}{\boldsymbol{C}}^e - 1)\right)\right]}{\partial\underset{\sim}{\boldsymbol{C}}^e} = (\underset{\sim}{\mathbf{1}}\underline{\otimes}\underset{\sim}{\boldsymbol{\Pi}}^{eT}) + \frac{1}{2}(\underset{\sim}{\boldsymbol{C}}^e\underline{\otimes}\underset{\sim}{\mathbf{1}}) : \underset{\approx}{\boldsymbol{C}} \tag{A.8}$$

$$\frac{\partial\underset{\sim}{\boldsymbol{C}}^e}{\partial\underset{\sim}{\boldsymbol{E}}} = \underset{\sim}{\mathbf{1}}\overline{\otimes}\underset{\sim}{\boldsymbol{E}}^T + \underset{\sim}{\boldsymbol{E}}^T\underline{\otimes}\underset{\sim}{\mathbf{1}} \qquad \frac{\partial\underset{\sim}{\boldsymbol{E}}}{\partial\Delta\underset{\sim}{\boldsymbol{E}}} = \underset{\approx}{\mathbf{1}} \tag{A.9}$$

$$\frac{\partial\mathcal{R}_{\gamma^s}}{\partial\Delta\underset{\sim}{\boldsymbol{E}}} = -\Delta\Gamma\Phi^{s'}\underset{\sim}{\boldsymbol{N}}^s : \left[(\underset{\sim}{\mathbf{1}}\underline{\otimes}\underset{\sim}{\boldsymbol{\Pi}}^e) + \frac{1}{2}(\underset{\sim}{\boldsymbol{C}}^e\underline{\otimes}\underset{\sim}{\mathbf{1}}) : \underset{\approx}{\boldsymbol{C}}\right] : (\underset{\sim}{\mathbf{1}}\overline{\otimes}\underset{\sim}{\boldsymbol{E}}^T + \underset{\sim}{\boldsymbol{E}}^T\underline{\otimes}\underset{\sim}{\mathbf{1}}) \tag{A.10}$$

$$\frac{\partial\mathcal{R}_{\gamma^s}}{\partial\Delta\gamma^p} \quad = \quad \delta_{sp} \tag{A.11}$$

$$\frac{\partial\mathcal{R}_{\gamma^s}}{\partial\Delta r^q} = -\Delta\Gamma\frac{\partial\Phi^s}{\partial f^s}\frac{\partial f^s}{\partial\tau_c^s}\frac{\partial\tau_c^s}{\partial\Delta r^q}\mathrm{sign}\left(\tau^s\right) = \mathrm{sign}\left(\tau^s\right)\Delta\Gamma\Phi^{s'}\frac{1}{2}\mu\left(\sum_{u=1}^{N}a^{su}r^u\right)^{-\frac{1}{2}}a^{sq} \tag{A.12}$$

$$\frac{\partial\mathcal{R}_{\gamma^s}}{\partial\Delta\gamma_{cum}} = -\Delta\Gamma\frac{\partial\Phi^s}{\partial f^s}\frac{\partial f^s}{\partial\gamma_{cum}}\mathrm{sign}\left(\tau^s\right) = \Delta\Gamma\Phi^{s'}\mu_\chi\mathrm{sign}\left(\tau^s\right) \tag{A.13}$$

- Derivatives of $\mathcal{R}_{r^s}$

$$\mathcal{R}_{r^s} = \Delta r^s - |\Delta\gamma^s|\left(\frac{\sqrt{\sum_{u=1}^{N}b^{su}r^u}}{\kappa} - G_c r^s\right) \tag{A.14}$$

$$\frac{\partial\mathcal{R}_{r^s}}{\partial\Delta\underset{\sim}{\boldsymbol{E}}} = 0 \qquad \frac{\partial\mathcal{R}_{r^s}}{\partial\Delta\gamma^p} = -\mathrm{sign}\left(\Delta\gamma^s\right)\delta_{sp}\left(\frac{\sqrt{\sum_{u=1}^{N}b^{su}r^u}}{\kappa} - G_c r^s\right) \tag{A.15}$$

$$\frac{\partial\mathcal{R}_{r^s}}{\partial\Delta r^q} = \delta_{sq} - |\Delta\gamma^s|\left(\frac{1}{2}\frac{\left(\sum_{u=1}^{N}b^{su}r^u\right)^{-\frac{1}{2}}b^{sq}}{\kappa} - G_c\delta_{sq}\right) \qquad \frac{\partial\mathcal{R}_{r^s}}{\partial\Delta\gamma_{cum}} = 0 \tag{A.16}$$

- Derivatives of $R_{\gamma_{cum}}$

$$R_{\gamma_{cum}} = \Delta\gamma_{cum} - \sum_{s=1}^{N} |\Delta\gamma^s| \tag{A.17}$$

$$\frac{\partial \mathcal{R}_{\gamma_{cum}}}{\partial \Delta \underset{\sim}{\boldsymbol{E}}} = 0 \qquad \frac{\partial \mathcal{R}_{\gamma_{cum}}}{\partial \Delta\gamma^p} = -\text{sign}\left(\Delta\gamma^p\right) \qquad \frac{\partial \mathcal{R}_{\gamma_{cum}}}{\partial \Delta r^q} = 0 \qquad \frac{\partial \mathcal{R}_{\gamma_{cum}}}{\partial \Delta\gamma_{cum}} = 1 \tag{A.18}$$

Appendix B. Details on the finite element implementation

In order to facilitate the numerical implementation in finite element code, the previous equations are written in vector and matrix form. The rates of nodal degrees of freedom $\dot{\tilde{u}}^a$, $\dot{\tilde{\gamma}}^b_\chi$ and $\dot{\tilde{\lambda}}^b$ are arranged in vector form as

$$\{\dot{\tilde{u}}^a_i\} = \{\dot{\tilde{\mathbf{u}}}^e\} = \begin{Bmatrix} \dot{\tilde{u}}^1_1 \\ \dot{\tilde{u}}^1_2 \\ \dot{\tilde{u}}^1_3 \\ \vdots \\ \dot{\tilde{u}}^p_1 \\ \dot{\tilde{u}}^p_2 \\ \dot{\tilde{u}}^p_3 \end{Bmatrix} \qquad \{\dot{\tilde{\gamma}}^b_\chi\} = \{\dot{\tilde{\boldsymbol{\gamma}}}^e_{\boldsymbol{\chi}}\} = \begin{Bmatrix} \dot{\tilde{\gamma}}^1_\chi \\ \dot{\tilde{\gamma}}^2_\chi \\ \vdots \\ \dot{\tilde{\gamma}}^q_\chi \end{Bmatrix} \qquad \{\dot{\tilde{\lambda}}^b\} = \{\dot{\tilde{\boldsymbol{\lambda}}}^e\} = \begin{Bmatrix} \dot{\tilde{\lambda}}^1 \\ \dot{\tilde{\lambda}}^2 \\ \vdots \\ \dot{\tilde{\lambda}}^q \end{Bmatrix} \tag{B.1}$$

Here, we drop the superscripts a and b used for summation over the nodes of one element and add a superscript label e, in order to indicate that the vector is for one individual element and to distinguish it from vectors for the entire finite element mesh. Recall that p is the number of nodes possessing displacement degrees of freedom and q is that for Δ_χ and microslip γ_χ. Voigt's notation is used for writing tensors in the form of vectors and matrices. Especially, the second-order non-symmetric tensor $\underset{\sim}{\boldsymbol{F}}$ is arranged in the form:

$$\{\underset{\sim}{\boldsymbol{F}}\} = \begin{Bmatrix} F_{11} \\ F_{22} \\ F_{33} \\ F_{12} \\ F_{23} \\ F_{31} \\ F_{21} \\ F_{32} \\ F_{13} \end{Bmatrix} \tag{B.2}$$

Thus, shape functions ${}^{u}N_i^a$ and ${}^{\chi}N^b$ can be written as

$$[{}^{\mathbf{u}}\mathbf{N}] = \begin{bmatrix} {}^{u}N^1 & 0 & 0 & \cdots & {}^{u}N^p & 0 & 0 \\ 0 & {}^{u}N^1 & 0 & \cdots & 0 & {}^{u}N^p & 0 \\ 0 & 0 & {}^{u}N^1 & \cdots & 0 & 0 & {}^{u}N^p \end{bmatrix} \tag{B.3}$$

and

$$[{}^{\chi}\mathbf{N}] = \begin{bmatrix} {}^{\chi}N^1 & {}^{\chi}N^2 & {}^{\chi}N^3 & \dots & {}^{\chi}N^q. \end{bmatrix} \tag{B.4}$$

Accordingly, ${}^{u}B_{ij}^a$ and ${}^{\chi}B_i^a$ can also be written in matrix form denoted by $[{}^{\mathbf{u}}\mathbf{B}]$ and $[{}^{\chi}\mathbf{B}]$:

$$[{}^{\mathbf{u}}\mathbf{B}] = \begin{bmatrix} \frac{\partial {}^{u}N^1}{\partial X_1} & 0 & 0 & \cdots & \frac{\partial {}^{u}N^p}{\partial X_1} & 0 & 0 \\ 0 & \frac{\partial {}^{u}N^1}{\partial X_2} & 0 & \cdots & 0 & \frac{\partial {}^{u}N^p}{\partial X_2} & 0 \\ 0 & 0 & \frac{\partial {}^{u}N^1}{\partial X_3} & \cdots & 0 & 0 & \frac{\partial {}^{u}N^p}{\partial X_3} \\ \frac{\partial {}^{u}N^1}{\partial X_2} & 0 & 0 & \cdots & \frac{\partial {}^{u}N^p}{\partial X_2} & 0 & 0 \\ 0 & \frac{\partial {}^{u}N^1}{\partial X_3} & 0 & \cdots & 0 & \frac{\partial {}^{u}N^p}{\partial X_3} & 0 \\ 0 & 0 & \frac{\partial {}^{u}N^1}{\partial X_1} & \cdots & 0 & 0 & \frac{\partial {}^{u}N^p}{\partial X_1} \\ 0 & \frac{\partial {}^{u}N^1}{\partial X_1} & 0 & \cdots & 0 & \frac{\partial {}^{u}N^p}{\partial X_1} & 0 \\ 0 & 0 & \frac{\partial {}^{u}N^1}{\partial X_2} & \cdots & 0 & 0 & \frac{\partial {}^{u}N^p}{\partial X_2} \\ \frac{\partial {}^{u}N^1}{\partial X_3} & 0 & 0 & \cdots & \frac{\partial {}^{u}N^p}{\partial X_3} & 0 & 0 \end{bmatrix} \tag{B.5}$$

and

$$[{}^{\chi}\mathbf{B}] = \begin{bmatrix} \frac{\partial {}^{\chi}N^1}{\partial X_1} & \frac{\partial {}^{\chi}N^2}{\partial X_1} & \frac{\partial {}^{\chi}N^3}{\partial X_1} & \cdots & \frac{\partial {}^{\chi}N^q}{\partial X_1} \\ \frac{\partial {}^{\chi}N^1}{\partial X_2} & \frac{\partial {}^{\chi}N^2}{\partial X_2} & \frac{\partial {}^{\chi}N^3}{\partial X_2} & \cdots & \frac{\partial {}^{\chi}N^q}{\partial X_2} \\ \frac{\partial {}^{\chi}N^1}{\partial X_3} & \frac{\partial {}^{\chi}N^2}{\partial X_3} & \frac{\partial {}^{\chi}N^3}{\partial X_3} & \cdots & \frac{\partial {}^{\chi}N^q}{\partial X_3} \end{bmatrix} \tag{B.6}$$

The interpolation of increment of the displacements $\dot{u}_i$, microslip $\dot{\gamma}_\chi$ and Lagrange multiplier $\dot{\lambda}$ in one element thus write

$$\{\underline{\dot{\boldsymbol{u}}}\} = [{}^{\mathbf{u}}\mathbf{N}].\{\dot{\tilde{\mathbf{u}}}^e\} \qquad \{\dot{\boldsymbol{\gamma}}_{\boldsymbol{\chi}}\} = [{}^{\chi}\mathbf{N}].\{\dot{\tilde{\boldsymbol{\gamma}}}_{\boldsymbol{\chi}}^e\} \tag{B.7}$$

$$\{\dot{\boldsymbol{\lambda}}\} = [{}^{\chi}\mathbf{N}].\{\dot{\tilde{\boldsymbol{\lambda}}}^e\} \quad \text{thus} \quad \{\dot{\boldsymbol{\Delta}}_{\boldsymbol{\chi}}\} = [{}^{\chi}\mathbf{N}].\left[\{\dot{\tilde{\boldsymbol{\lambda}}}^e\} + \mu_\chi\{\dot{\tilde{\boldsymbol{\gamma}}}_{\boldsymbol{\chi}}^e\}\right] \tag{B.8}$$

and therefore it follows that

$$\{\dot{\underset{\sim}{\boldsymbol{F}}}\} = [{}^{\mathbf{u}}\mathbf{B}].\{\dot{\tilde{\mathbf{u}}}^e\} \qquad \{\underline{\dot{\boldsymbol{K}}}_{\boldsymbol{\chi}}\} = [{}^{\chi}\mathbf{B}].\{\dot{\tilde{\boldsymbol{\gamma}}}_{\boldsymbol{\chi}}^e\}. \tag{B.9}$$

With stress and strain variables expressed with Voigt's notation, Eqs. (57), (58), (59) and (60) follow

$$\{\mathbf{R}^e_{\text{int(u)}}\} = \int_{D^e_0} [{}^{\text{u}}\mathbf{B}]^T.\{\underset{\sim}{\boldsymbol{S}}\}\mathrm{d}V^e_0 \tag{B.10}$$

$$\{\mathbf{R}^e_{\text{int}(\gamma_\chi)}\} = \int_{D^e_0} A[{}^{\chi}\mathbf{B}]^T.[{}^{\chi}\mathbf{B}].\{\boldsymbol{\gamma}_{\boldsymbol{\chi}}\} + [{}^{\chi}\mathbf{N}]^T.\left(\{\boldsymbol{\Delta}_{\boldsymbol{\chi}}\} - \mu_\chi\{\boldsymbol{\gamma}_{\boldsymbol{M}}\}\right)\mathrm{d}V^e_0 \tag{B.11}$$

$$\{\mathbf{R}^e_{\text{int}(\lambda)}\} = \int_{D^e_0} [{}^{\chi}\mathbf{N}]^T.\left(\{\boldsymbol{\gamma}_{\boldsymbol{\chi}}\} - \{\boldsymbol{\gamma}_{\boldsymbol{M}}\}\right)\mathrm{d}V^e_0 \tag{B.12}$$

$$\{\mathbf{R}^e_{\text{ext(u)}}\} = \int_{\partial D^e_0} [{}^{\text{u}}\mathbf{N}]^T.\{\underline{\boldsymbol{T}}\}\mathrm{d}S^e_0 \tag{B.13}$$

$$\{\mathbf{R}^e_{\text{ext}(\gamma_\chi)}\} = \int_{\partial D^e_0} [{}^{\chi}\mathbf{N}]^T.\{\mathbf{M}\}\mathrm{d}S^e_0 \tag{B.14}$$

$$\{\mathbf{R}^e_{\text{ext}(\lambda)}\} = \{\mathbf{0}\} \tag{B.15}$$

where $[{}^{\text{u}}\mathbf{B}]^T$ is the transpose of the matrix $[{}^{\text{u}}\mathbf{B}]$ and the same notation is used for other matrices. In practice the integrals are approximated in each element by a Gaussian quadrature rule. The global finite element set of equations is obtained by applying an assembly operator $\mathcal{A}$ on internal reactions and external reactions:

$$\{\mathbf{R}_{\text{int(u)}}\} = \mathcal{A}(\{\mathbf{R}^e_{\text{int(u)}}\}) \qquad \{\mathbf{R}_{\text{int}(\gamma_\chi)}\} = \mathcal{A}(\{\mathbf{R}^e_{\text{int}(\gamma_\chi)}\}) \qquad \{\mathbf{R}_{\text{int}(\lambda)}\} = \mathcal{A}(\{\mathbf{R}^e_{\text{int}(\lambda)}\}) \tag{B.16}$$

$$\{\mathbf{R}_{\text{ext(u)}}\} = \mathcal{A}(\{\mathbf{R}^e_{\text{ext(u)}}\}) \qquad \{\mathbf{R}_{\text{ext}(\gamma_\chi)}\} = \mathcal{A}(\{\mathbf{R}^e_{\text{ext}(\gamma_\chi)}\}) \qquad \{\mathbf{R}_{\text{ext}(\lambda)}\} = \mathcal{A}(\{\mathbf{R}^e_{\text{ext}(\lambda)}\}) \tag{B.17}$$

The reader is referred to (Besson et al., 2009) for the description of the assembly procedure. Thus, the global finite element set of equations Eqs. (61), (62) and (63) to be solved can be written as

$$\begin{Bmatrix} \{\mathbf{R}_{\text{int(u)}}\} \\ \{\mathbf{R}_{\text{int}(\gamma_\chi)}\} \\ \{\mathbf{R}_{\text{int}(\lambda)}\} \end{Bmatrix} . \begin{Bmatrix} \{\dot{\tilde{\mathbf{u}}}\} \\ \{\dot{\tilde{\boldsymbol{\gamma}}}_{\boldsymbol{\chi}}\} \\ \{\dot{\tilde{\boldsymbol{\lambda}}}\} \end{Bmatrix} = \begin{Bmatrix} \{\mathbf{R}_{\text{ext(u)}}\} \\ \{\mathbf{R}_{\text{ext}(\gamma_\chi)}\} \\ \{\mathbf{R}_{\text{ext}(\lambda)}\} \end{Bmatrix} . \begin{Bmatrix} \{\dot{\tilde{\mathbf{u}}}\} \\ \{\dot{\tilde{\boldsymbol{\gamma}}}_{\boldsymbol{\chi}}\} \\ \{\dot{\tilde{\boldsymbol{\lambda}}}\} \end{Bmatrix} \tag{B.18}$$

Since the system is nonlinear, it can be solved by Newton's method which requires the calculation of the Jacobian matrix with respect to the internal reactions (Besson et al., 2009). The Jacobian matrix of an individual element, split into nine blocks, writes

$$\begin{bmatrix} [\mathbf{K}^e_{\text{(uu)}}] & [\mathbf{K}^e_{\text{(ug)}}] & [\mathbf{K}^e_{\text{(ul)}}] \\ [\mathbf{K}^e_{\text{(gu)}}] & [\mathbf{K}^e_{\text{(gg)}}] & [\mathbf{K}^e_{\text{(gl)}}] \\ [\mathbf{K}^e_{\text{(lu)}}] & [\mathbf{K}^e_{\text{(lg)}}] & [\mathbf{K}^e_{\text{(ll)}}] \end{bmatrix} = \begin{bmatrix} \left[\frac{\partial\{\mathbf{R}^e_{\text{int(u)}}\}}{\partial\{\tilde{\mathbf{u}}^e\}}\right] & \left[\frac{\partial\{\mathbf{R}^e_{\text{int(u)}}\}}{\partial\{\tilde{\boldsymbol{\gamma}}^e_{\boldsymbol{\chi}}\}}\right] & \left[\frac{\partial\{\mathbf{R}^e_{\text{int(u)}}\}}{\partial\{\tilde{\boldsymbol{\lambda}}^e\}}\right] \\ \left[\frac{\partial\{\mathbf{R}^e_{\text{int}(\gamma_\chi)}\}}{\partial\{\tilde{\mathbf{u}}^e\}}\right] & \left[\frac{\partial\{\mathbf{R}^e_{\text{int}(\gamma_\chi)}\}}{\partial\{\tilde{\boldsymbol{\gamma}}^e_{\boldsymbol{\chi}}\}}\right] & \left[\frac{\partial\{\mathbf{R}^e_{\text{int}(\gamma_\chi)}\}}{\partial\{\tilde{\boldsymbol{\lambda}}^e\}}\right] \\ \left[\frac{\partial\{\mathbf{R}^e_{\text{int}(\lambda)}\}}{\partial\{\tilde{\mathbf{u}}^e\}}\right] & \left[\frac{\partial\{\mathbf{R}^e_{\text{int}(\lambda)}\}}{\partial\{\tilde{\boldsymbol{\gamma}}^e_{\boldsymbol{\chi}}\}}\right] & \left[\frac{\partial\{\mathbf{R}^e_{\text{int}(\lambda)}\}}{\partial\{\tilde{\boldsymbol{\lambda}}^e\}}\right] \end{bmatrix} \tag{B.19}$$

Using the assembly operation $\mathcal{A}$, one can calculate the global Jacobian matrix $[\mathbf{K}]$

$$[\mathbf{K}] = \mathcal{A}\begin{bmatrix} [\mathbf{K}^e_{\text{(uu)}}] & [\mathbf{K}^e_{\text{(ug)}}] & [\mathbf{K}^e_{\text{(ul)}}] \\ [\mathbf{K}^e_{\text{(gu)}}] & [\mathbf{K}^e_{\text{(gg)}}] & [\mathbf{K}^e_{\text{(gl)}}] \\ [\mathbf{K}^e_{\text{(lu)}}] & [\mathbf{K}^e_{\text{(lg)}}] & [\mathbf{K}^e_{\text{(ll)}}] \end{bmatrix} \tag{B.20}$$

One calculates the blocks for an individual element and obtains the so-called element stiffness matrix:

$$[\mathbf{K}^e_{(\mathrm{uu})}] = \frac{\partial\{\mathbf{R}^e_{\mathrm{int(u)}}\}}{\partial\{\widetilde{\mathbf{u}}^e\}} = \int_{D^e_0} [{}^{\mathrm{u}}\mathbf{B}]^T . \frac{\partial\{\underset{\sim}{\boldsymbol{S}}\}}{\partial\{\underset{\sim}{\boldsymbol{F}}\}} . \frac{\partial\{\underset{\sim}{\boldsymbol{F}}\}}{\partial\{\widetilde{\mathbf{u}}^e\}} \,\mathrm{d}V^e_0$$
$$= \int_{D^e_0} [{}^{\mathrm{u}}\mathbf{B}]^T . \frac{\partial\{\underset{\sim}{\boldsymbol{S}}\}}{\partial\{\underset{\sim}{\boldsymbol{F}}\}} . [{}^{\mathrm{u}}\mathbf{B}] \,\mathrm{d}V^e_0 \tag{B.21}$$

$$[\mathbf{K}^e_{(\mathrm{ug})}] = \frac{\partial\{\mathbf{R}^e_{\mathrm{int(u)}}\}}{\partial\{\widetilde{\gamma}^e_{\boldsymbol{\chi}}\}} = \int_{D^e_0} \left([{}^{\mathrm{u}}\mathbf{B}]^T . \frac{\partial\{\underset{\sim}{\boldsymbol{S}}\}}{\partial\{\boldsymbol{\gamma}_{\boldsymbol{\chi}}\}} . \frac{\partial\{\boldsymbol{\gamma}_{\boldsymbol{\chi}}\}}{\partial\{\widetilde{\gamma}^e_{\boldsymbol{\chi}}\}} + [{}^{\mathrm{u}}\mathbf{B}]^T . \frac{\partial\{\underset{\sim}{\boldsymbol{S}}\}}{\partial\{\boldsymbol{\Delta}_{\boldsymbol{\chi}}\}} . \frac{\partial\{\boldsymbol{\Delta}_{\boldsymbol{\chi}}\}}{\partial\{\widetilde{\gamma}_{\boldsymbol{\chi}}\}} . \frac{\partial\{\widetilde{\gamma}_{\boldsymbol{\chi}}\}}{\partial\{\widetilde{\gamma}^e_{\boldsymbol{\chi}}\}} \right) \mathrm{d}V^e_0$$
$$= \int_{D^e_0} \left([{}^{\mathrm{u}}\mathbf{B}]^T . \frac{\partial\{\underset{\sim}{\boldsymbol{S}}\}}{\partial\{\boldsymbol{\gamma}_{\boldsymbol{\chi}}\}} . [{}^{\chi}\mathbf{N}] + \mu_\chi [{}^{\mathrm{u}}\mathbf{B}]^T . \frac{\partial\{\underset{\sim}{\boldsymbol{S}}\}}{\partial\{\boldsymbol{\lambda}\}} . [{}^{\chi}\mathbf{N}] \right) \mathrm{d}V^e_0 \tag{B.22}$$

$$[\mathbf{K}^e_{(\mathrm{ul})}] = \frac{\partial\{\mathbf{R}^e_{\mathrm{int(u)}}\}}{\partial\{\widetilde{\boldsymbol{\lambda}}^e\}} = \int_{D^e_0} \left([{}^{\mathrm{u}}\mathbf{B}]^T . \frac{\partial\{\underset{\sim}{\boldsymbol{S}}\}}{\partial\{\boldsymbol{\Delta}_{\boldsymbol{\chi}}\}} . \frac{\partial\{\boldsymbol{\Delta}_{\boldsymbol{\chi}}\}}{\partial\{\boldsymbol{\lambda}\}} . \frac{\partial\{\boldsymbol{\lambda}\}}{\partial\{\widetilde{\boldsymbol{\lambda}}^e\}} \right) \mathrm{d}V^e_0$$
$$= \int_{D^e_0} \left([{}^{\mathrm{u}}\mathbf{B}]^T . \frac{\partial\{\underset{\sim}{\boldsymbol{S}}\}}{\partial\{\boldsymbol{\Delta}_{\boldsymbol{\chi}}\}} . [{}^{\chi}\mathbf{N}] \right) \mathrm{d}V^e_0 \tag{B.23}$$

$$[\mathbf{K}^e_{(\mathrm{gu})}] = \frac{\partial\{\mathbf{R}^e_{\mathrm{int}(\gamma_\chi)}\}}{\partial\{\widetilde{\mathbf{u}}^e\}} = \int_{D^e_0} \left(-\mu_\chi [{}^{\chi}\mathbf{N}]^T . \frac{\partial\{\gamma_M\}}{\partial\{\underset{\sim}{\boldsymbol{F}}\}} . \frac{\partial\{\underset{\sim}{\boldsymbol{F}}\}}{\partial\{\widetilde{\mathbf{u}}^e\}} \right) \mathrm{d}V^e_0$$
$$= \int_{D^e_0} \left(-\mu_\chi [{}^{\chi}\mathbf{N}]^T . \frac{\partial\{\gamma_M\}}{\partial\{\underset{\sim}{\boldsymbol{F}}\}} . [{}^{\mathrm{u}}\mathbf{B}] \right) \mathrm{d}V^e_0 \tag{B.24}$$

$$[\mathbf{K}^e_{(\mathrm{gg})}] = \frac{\partial\{\mathbf{R}^e_{\mathrm{int}(\gamma_\chi)}\}}{\partial\{\widetilde{\gamma}^e_{\boldsymbol{\chi}}\}} = \int_{D^e_0} \left(A [{}^{\chi}\mathbf{B}]^T . [{}^{\chi}\mathbf{B}] . \frac{\partial\{\boldsymbol{\gamma}_{\boldsymbol{\chi}}\}}{\partial\{\widetilde{\gamma}^e_{\boldsymbol{\chi}}\}} + \mu_\chi [{}^{\chi}\mathbf{N}]^T . \frac{\partial\{\boldsymbol{\gamma}_{\boldsymbol{\chi}}\}}{\partial\{\widetilde{\gamma}^e_{\boldsymbol{\chi}}\}} - \mu_\chi [{}^{\chi}\mathbf{N}]^T . \frac{\partial\{\gamma_M\}}{\partial\{\boldsymbol{\Delta}_{\boldsymbol{\chi}}\}} . \frac{\partial\{\boldsymbol{\Delta}_{\boldsymbol{\chi}}\}}{\partial\{\widetilde{\gamma}_{\boldsymbol{\chi}}\}} . \frac{\partial\{\widetilde{\gamma}_{\boldsymbol{\chi}}\}}{\partial\{\widetilde{\gamma}^e_{\boldsymbol{\chi}}\}} \right) \mathrm{d}V^e_0$$
$$= \int_{D^e_0} \left(A [{}^{\chi}\mathbf{B}]^T . [{}^{\chi}\mathbf{B}] . [{}^{\chi}\mathbf{N}] + \mu_\chi [{}^{\chi}\mathbf{N}]^T . [{}^{\chi}\mathbf{N}] - \mu^2_\chi [{}^{\chi}\mathbf{N}]^T . \frac{\partial\{\gamma_M\}}{\partial\{\boldsymbol{\Delta}_{\boldsymbol{\chi}}\}} . [{}^{\chi}\mathbf{N}] \right) \mathrm{d}V^e_0 \tag{B.25}$$

$$[\mathbf{K}^e_{(\mathrm{gl})}] = \frac{\partial\{\mathbf{R}^e_{\mathrm{int}(\gamma_\chi)}\}}{\partial\{\widetilde{\boldsymbol{\lambda}}^e\}} = \int_{D^e_0} \left([{}^{\chi}\mathbf{N}]^T . \frac{\partial\{\boldsymbol{\lambda}\}}{\partial\{\widetilde{\boldsymbol{\lambda}}^e\}} - \mu_\chi [{}^{\chi}\mathbf{N}]^T . \frac{\partial\{\gamma_M\}}{\partial\{\boldsymbol{\Delta}_{\boldsymbol{\chi}}\}} . \frac{\partial\{\boldsymbol{\Delta}_{\boldsymbol{\chi}}\}}{\partial\{\boldsymbol{\lambda}\}} \frac{\partial\{\boldsymbol{\lambda}\}}{\partial\{\widetilde{\boldsymbol{\lambda}}^e\}} \right) \mathrm{d}V^e_0$$
$$= \int_{D^e_0} \left([{}^{\chi}\mathbf{N}]^T . [{}^{\chi}\mathbf{N}] - \mu_\chi [{}^{\chi}\mathbf{N}]^T . \frac{\partial\{\gamma_M\}}{\partial\{\boldsymbol{\Delta}_{\boldsymbol{\chi}}\}} . [{}^{\chi}\mathbf{N}] \right) \mathrm{d}V^e_0 \tag{B.26}$$

$$[\mathbf{K}^e_{(\mathrm{lu})}] = \frac{\partial\{\mathbf{R}^e_{\mathrm{int}(\lambda)}\}}{\partial\{\widetilde{\mathbf{u}}^e\}} = \int_{D^e_0} \left(-[{}^{\chi}\mathbf{N}]^T . \frac{\partial\{\gamma_M\}}{\partial\{\underset{\sim}{\boldsymbol{F}}\}} . \frac{\partial\{\underset{\sim}{\boldsymbol{F}}\}}{\partial\{\widetilde{\mathbf{u}}^e\}} \right) \mathrm{d}V^e_0$$
$$= \int_{D^e_0} \left(-[{}^{\chi}\mathbf{N}]^T . \frac{\partial\{\gamma_M\}}{\partial\{\underset{\sim}{\boldsymbol{F}}\}} . [{}^{\mathrm{u}}\mathbf{B}] \right) \mathrm{d}V^e_0 \tag{B.27}$$

$$[\mathbf{K}^e_{(\mathrm{lg})}] = \frac{\partial\{\mathbf{R}^e_{\mathrm{int}(\lambda)}\}}{\partial\{\widetilde{\gamma}^e_{\boldsymbol{\chi}}\}} = \int_{D^e_0} \left([{}^{\chi}\mathbf{N}]^T . \frac{\partial\{\boldsymbol{\gamma}_{\boldsymbol{\chi}}\}}{\partial\{\widetilde{\gamma}^e_{\boldsymbol{\chi}}\}} - [{}^{\chi}\mathbf{N}]^T . \frac{\partial\{\gamma_M\}}{\partial\{\boldsymbol{\Delta}_{\boldsymbol{\chi}}\}} . \frac{\partial\{\boldsymbol{\Delta}_{\boldsymbol{\chi}}\}}{\partial\{\boldsymbol{\gamma}_{\boldsymbol{\chi}}\}} . \frac{\partial\{\boldsymbol{\gamma}_{\boldsymbol{\chi}}\}}{\partial\{\widetilde{\gamma}^e_{\boldsymbol{\chi}}\}} \right) \mathrm{d}V^e_0$$
$$= \int_{D^e_0} \left([{}^{\chi}\mathbf{N}]^T . [{}^{\chi}\mathbf{N}] - \mu_\chi [{}^{\chi}\mathbf{N}]^T . \frac{\partial\{\gamma_M\}}{\partial\{\boldsymbol{\Delta}_{\boldsymbol{\chi}}\}} . [{}^{\chi}\mathbf{N}] \right) \mathrm{d}V^e_0 \tag{B.28}$$

$$[\mathbf{K}^e_{(\mathrm{ll})}] = \frac{\partial\{\mathbf{R}^e_{\mathrm{int}(\lambda)}\}}{\partial\{\widetilde{\boldsymbol{\lambda}}^e\}} = \int_{D^e_0} \left(-[{}^{\chi}\mathbf{N}]^T . \frac{\partial\{\gamma_M\}}{\partial\{\boldsymbol{\Delta}_{\boldsymbol{\chi}}\}} . \frac{\partial\{\boldsymbol{\Delta}_{\boldsymbol{\chi}}\}}{\partial\{\boldsymbol{\lambda}\}} . \frac{\partial\{\boldsymbol{\lambda}\}}{\partial\{\widetilde{\boldsymbol{\lambda}}^e\}} \right) \mathrm{d}V^e_0$$
$$= \int_{D^e_0} \left(-[{}^{\chi}\mathbf{N}]^T . \frac{\partial\{\gamma_M\}}{\partial\{\boldsymbol{\Delta}_{\boldsymbol{\chi}}\}} . [{}^{\chi}\mathbf{N}] \right) \mathrm{d}V^e_0 \tag{B.29}$$

In the element stiffness matrix, one can find four derivatives which will be evaluated by consistent tangent matrix $\{\mathbf{J}^*\}$ in the next section. The consistent tangent matrix $\{\mathbf{J}^*\}$ is defined as:

$$\mathbf{J}^* = \frac{\delta \Delta v_{\mathrm{OUT}}}{\delta \Delta v_{\mathrm{IN}}} \tag{B.30}$$

Appendix C. Details on the consistent tangent matrix

It is shown in (Ling et al., 2018) that the consistent tangent matrix is

$$\mathbf{J}^* = \left\{ \frac{\partial \Delta v_{\mathrm{OUT}}}{\partial \Delta v_{\mathrm{INT}}} \left[-\left(\frac{\partial \mathcal{R}}{\partial \Delta v_{\mathrm{INT}}} \right)^{-1} \frac{\partial \mathcal{R}}{\partial \Delta v_{\mathrm{IN}}} \right] + \frac{\partial \Delta v_{\mathrm{OUT}}}{\partial \Delta v_{\mathrm{IN}}} \right\} \tag{C.1}$$

which involves the inverse of the (local) Jacobian matrix $\mathcal{J} = \partial \mathcal{R} / \partial v_{\mathrm{INT}}$.

- $\frac{\partial \Delta v_{\mathrm{OUT}}}{\partial \Delta v_{\mathrm{INT}}}$

$$\frac{\partial \Delta \underset{\sim}{\boldsymbol{S}}}{\partial \Delta \underset{\sim}{\boldsymbol{E}}} = \frac{\partial \underset{\sim}{\boldsymbol{S}}}{\partial \underset{\sim}{\boldsymbol{E}}} = \frac{\partial \underset{\sim}{\boldsymbol{S}}}{\partial \underset{\sim}{\boldsymbol{\sigma}}} : \frac{\partial \underset{\sim}{\boldsymbol{\sigma}}}{\partial \underset{\sim}{\boldsymbol{E}}} \tag{C.2}$$

$$\frac{\partial \underset{\sim}{\boldsymbol{S}}}{\partial \underset{\sim}{\boldsymbol{\sigma}}} = J \underset{\sim}{\mathbf{1}} \underline{\otimes} \underset{\sim}{\boldsymbol{F}}^{-1} \tag{C.3}$$

$$\begin{aligned} \frac{\partial \underset{\sim}{\boldsymbol{\sigma}}}{\partial \underset{\sim}{\boldsymbol{E}}} &= -\frac{1}{J_e} (\underset{\sim}{\boldsymbol{E}} . \underset{\sim}{\boldsymbol{\Pi}}^e . \underset{\sim}{\boldsymbol{E}}^T) \otimes \underset{\sim}{\boldsymbol{E}}^{-T} + \frac{1}{J_e} \underset{\sim}{\mathbf{1}} \underline{\otimes} (\underset{\sim}{\boldsymbol{\Pi}}^e . \underset{\sim}{\boldsymbol{E}}^T)^T \\ &\quad + \frac{1}{J_e} (\underset{\sim}{\boldsymbol{E}} \underline{\otimes} \underset{\sim}{\boldsymbol{E}}) : \frac{\partial \underset{\sim}{\boldsymbol{\Pi}}^e}{\partial \underset{\sim}{\boldsymbol{E}}} + \frac{1}{J_e} \left[(\underset{\sim}{\boldsymbol{E}} . \underset{\sim}{\boldsymbol{\Pi}}^e) \underline{\otimes} \underset{\sim}{\mathbf{1}} \right] : (\underset{\sim}{\mathbf{1}} \overline{\otimes} \underset{\sim}{\mathbf{1}}) \end{aligned} \tag{C.4}$$

$$\frac{\partial \underset{\sim}{\boldsymbol{\Pi}}^e}{\partial \underset{\sim}{\boldsymbol{E}}} = \frac{\partial \underset{\sim}{\boldsymbol{\Pi}}^e}{\partial \underset{\sim}{\boldsymbol{E}}^e_{GL}} : \frac{\partial \underset{\sim}{\boldsymbol{E}}^e_{GL}}{\partial \underset{\sim}{\boldsymbol{E}}} \tag{C.5}$$

$$\frac{\partial \underset{\sim}{\boldsymbol{\Pi}}^e}{\partial \underset{\sim}{\boldsymbol{E}}^e_{GL}} = \underset{\approx}{\boldsymbol{C}} \tag{C.6}$$

$$\frac{\partial \underset{\sim}{\boldsymbol{E}}^e_{GL}}{\partial \underset{\sim}{\boldsymbol{E}}} = \frac{1}{2} (\underset{\sim}{\mathbf{1}} \overline{\otimes} \underset{\sim}{\boldsymbol{E}}^T + \underset{\sim}{\boldsymbol{E}}^T \underline{\otimes} \underset{\sim}{\mathbf{1}}) \tag{C.7}$$

$$\frac{\partial \Delta \underset{\sim}{\boldsymbol{S}}}{\partial \Delta \gamma^s} = 0 \qquad \frac{\partial \Delta \underset{\sim}{\boldsymbol{S}}}{\partial \Delta r^s} = 0 \qquad \frac{\partial \Delta \underset{\sim}{\boldsymbol{S}}}{\partial \Delta \gamma_{cum}} = 0 \tag{C.8}$$

$$\frac{\partial \Delta \gamma_M}{\partial \Delta \underset{\sim}{\boldsymbol{E}}} = 0 \qquad \frac{\partial \Delta \gamma_M}{\partial \Delta \gamma^s} = 0 \qquad \frac{\partial \Delta \gamma_M}{\partial \Delta r^s} = 0 \qquad \frac{\partial \Delta \gamma_M}{\partial \Delta \gamma_{cum}} = 1 \tag{C.9}$$

- $\frac{\partial \mathcal{R}}{\partial \Delta v_{\mathrm{IN}}}$

$$\frac{\partial R_{\underset{\sim}{\boldsymbol{E}}}}{\partial \Delta \Delta_\chi} = 0 \qquad \frac{\partial R_{\underset{\sim}{\boldsymbol{E}}}}{\partial \Delta \underset{\sim}{\boldsymbol{F}}} = -\frac{\partial (\Delta \underset{\sim}{\boldsymbol{F}} . \underset{\sim}{\boldsymbol{F}}^{-1} . \underset{\sim}{\boldsymbol{E}})}{\partial \Delta \underset{\sim}{\boldsymbol{F}}} \tag{C.10}$$

$$= -\underset{\sim}{\mathbf{1}} \underline{\otimes} \left(\underset{\sim}{\boldsymbol{F}}^{-1} . \underset{\sim}{\boldsymbol{E}} \right)^T - (\Delta \underset{\sim}{\boldsymbol{F}} \underline{\otimes} \underset{\sim}{\boldsymbol{E}}^T) : \frac{\partial \underset{\sim}{\boldsymbol{F}}^{-1}}{\partial \underset{\sim}{\boldsymbol{F}}} : \frac{\partial \underset{\sim}{\boldsymbol{F}}}{\partial \Delta \underset{\sim}{\boldsymbol{F}}} \tag{C.11}$$

$$= -\underset{\sim}{\mathbf{1}} \underline{\otimes} \left(\underset{\sim}{\boldsymbol{E}}^T . \underset{\sim}{\boldsymbol{F}}^{-T} \right)^T - (\Delta \underset{\sim}{\boldsymbol{F}} \underline{\otimes} \underset{\sim}{\boldsymbol{E}}^T) : (-\underset{\sim}{\boldsymbol{F}}^{-1} \underline{\otimes} \underset{\sim}{\boldsymbol{F}}^{-T}) : \underset{\approx}{\mathbf{1}} \tag{C.12}$$

$$= -\underset{\sim}{\mathbf{1}} \underline{\otimes} \left(\underset{\sim}{\boldsymbol{E}}^T . \underset{\sim}{\boldsymbol{F}}^{-T} \right) + (\Delta \underset{\sim}{\boldsymbol{F}} \underline{\otimes} \underset{\sim}{\boldsymbol{E}}^T) : (\underset{\sim}{\boldsymbol{F}}^{-1} \underline{\otimes} \underset{\sim}{\boldsymbol{F}}^{-T}) \tag{C.13}$$

For the rate-dependent formulation

$$\frac{\partial R_{\gamma^s}}{\partial \Delta \underset{\sim}{\boldsymbol{F}}} = 0 \tag{C.14}$$

For the rate-independent formulation

$$\frac{\partial R_{\gamma^s}}{\partial \Delta \underset{\sim}{\boldsymbol{F}}} = -\mathrm{sign}\,(\tau^s)\, \Phi^s \frac{\partial \Delta \varepsilon_{eq}}{\partial \Delta \underset{\sim}{\boldsymbol{F}}} \tag{C.15}$$

$$\frac{\partial \Delta\varepsilon_{eq}}{\partial \Delta \underset{\sim}{\boldsymbol{F}}} = \frac{\partial \Delta\varepsilon_{eq}}{\partial \Delta \underset{\sim}{\boldsymbol{D}}'} : \frac{\partial \Delta \underset{\sim}{\boldsymbol{D}}'}{\partial \Delta \underset{\sim}{\boldsymbol{D}}} : \frac{\partial \Delta \underset{\sim}{\boldsymbol{D}}}{\partial \Delta \underset{\sim}{\boldsymbol{L}}} : \frac{\partial \Delta \underset{\sim}{\boldsymbol{L}}}{\partial \Delta \underset{\sim}{\boldsymbol{F}}} \tag{C.16}$$

$$= \frac{2}{3} \frac{\Delta \underset{\sim}{\boldsymbol{D}}'}{\Delta\varepsilon_{eq}} : \frac{\partial (\Delta \underset{\sim}{\boldsymbol{F}} \underset{\sim}{\boldsymbol{F}}^{-1})}{\partial \Delta \underset{\sim}{\boldsymbol{F}}} \tag{C.17}$$

$$\frac{\partial (\Delta \underset{\sim}{\boldsymbol{F}}.\underset{\sim}{\boldsymbol{F}}^{-1})}{\partial \Delta \underset{\sim}{\boldsymbol{F}}} = \underset{\approx}{\mathbf{1}} \underline{\otimes} \underset{\sim}{\boldsymbol{F}}^{-T} + \Delta \underset{\sim}{\boldsymbol{F}} \frac{\partial \underset{\sim}{\boldsymbol{F}}^{-1}}{\partial \underset{\sim}{\boldsymbol{F}}} : \frac{\partial \underset{\sim}{\boldsymbol{F}}}{\partial \Delta \underset{\sim}{\boldsymbol{F}}} \tag{C.18}$$

$$= \underset{\approx}{\mathbf{1}} \underline{\otimes} \underset{\sim}{\boldsymbol{F}}^{-T} + (\Delta \underset{\sim}{\boldsymbol{F}} \underline{\otimes} \underset{\sim}{\mathbf{1}}) : (-\underset{\sim}{\boldsymbol{F}}^{-1} \underline{\otimes} \underset{\sim}{\boldsymbol{F}}^{-T}) : \underset{\approx}{\mathbf{1}} \tag{C.19}$$

$$\frac{\partial R_{\gamma^s}}{\partial \Delta \Delta_\chi} = -\text{sign}\,(\tau^s)\, \Delta\Gamma \frac{\partial \Phi^s}{\partial f^s} \frac{\partial f^s}{\partial \Delta \Delta_\chi} = -\text{sign}\,(\tau^s)\, \Delta\Gamma \Phi^{s'} \frac{\rho_\sharp}{\rho_0} \tag{C.20}$$

$$\frac{\partial R_{r^s}}{\partial \Delta \underset{\sim}{\boldsymbol{F}}} = 0 \qquad \frac{\partial R_{r^s}}{\partial \Delta \Delta_\chi} = 0 \tag{C.21}$$

$$\frac{\partial R_{\gamma_{cum}}}{\partial \Delta \underset{\sim}{\boldsymbol{F}}} = 0 \qquad \frac{\partial R_{\gamma_{cum}}}{\partial \Delta \Delta_\chi} = 0 \tag{C.22}$$

- $\frac{\partial \Delta v_{\text{OUT}}}{\partial \Delta v_{\text{IN}}}$

$$\frac{\partial \Delta \underset{\sim}{\boldsymbol{S}}}{\partial \Delta \underset{\sim}{\boldsymbol{F}}} = \frac{\partial \underset{\sim}{\boldsymbol{S}}}{\partial \underset{\sim}{\boldsymbol{F}}} = (\underset{\sim}{\boldsymbol{\sigma}}.\underset{\sim}{\boldsymbol{F}}^{-T}) \otimes \frac{\partial J}{\partial \underset{\sim}{\boldsymbol{F}}} + J \frac{\partial \underset{\sim}{\boldsymbol{\sigma}}.\underset{\sim}{\boldsymbol{F}}^{-T}}{\partial \underset{\sim}{\boldsymbol{F}}^{-T}} : \frac{\partial \underset{\sim}{\boldsymbol{F}}^{-T}}{\partial \underset{\sim}{\boldsymbol{F}}} \tag{C.23}$$

$$= J(\underset{\sim}{\boldsymbol{\sigma}}.\underset{\sim}{\boldsymbol{F}}^{-T}) \otimes \underset{\sim}{\boldsymbol{F}}^{-T} + J(\underset{\sim}{\boldsymbol{\sigma}} \underline{\otimes} \underset{\sim}{\mathbf{1}}) : (-\underset{\sim}{\boldsymbol{F}}^{-T} \overline{\otimes} \underset{\sim}{\boldsymbol{F}}^{-1}) \tag{C.24}$$

$$\frac{\partial \Delta \underset{\sim}{\boldsymbol{S}}}{\partial \Delta \Delta_\chi} = 0 \qquad \frac{\partial \Delta \gamma_M}{\partial \Delta \underset{\sim}{\boldsymbol{F}}} = 0 \qquad \frac{\partial \Delta \gamma_M}{\partial \Delta \Delta_\chi} = 0 \tag{C.25}$$

References

Acharya, A., Bassani, J., 2000. Lattice incompatibility and a gradient theory of crystal plasticity. Journal of the Mechanics and Physics of Solids 48, 1565–1595.

Aifantis, E.C., 1984. On the microstructural origin of certain inelastic models. Journal of Engineering Materials and technology 106, 326–330.

Anand, L., Aslan, O., Chester, S.A., 2012. A large-deformation gradient theory for elastic–plastic materials: Strain softening and regularization of shear bands. International Journal of Plasticity 30-31, 116 – 143.

Ashby, M.F., 1970. The deformation of plastically non-homogeneous materials. The Philosophical Magazine: A Journal of Theoretical Experimental and Applied Physics 21, 399–424.

Aslan, O., Cordero, N., Gaubert, A., Forest, S., 2011. Micromorphic approach to single crystal plasticity and damage. International Journal of Engineering Science 49, 1311 – 1325.

Bardella, L., 2006. A deformation theory of strain gradient crystal plasticity that accounts for geometrically necessary dislocations. Journal of the Mechanics and Physics of Solids 54, 128–160.

Bardella, L., Segurado, J., Panteghini, A., Llorca, J., 2013. Latent hardening size effect in small-scale plasticity. Modelling and Simulation in Materials Science and Engineering 21, 055009.

Bayerschen, E., 2016. Single-crystal gradient plasticity with an accumulated plastic slip: Theory and applications. Phd thesis. KIT, Karlsruhe, Germany.

Belytschko, T., Ong, J.S.J., Liu, W.K., Kennedy, J.M., 1984. Hourglass control in linear and nonlinear problems. Computer Methods in Applied Mechanics and Engineering 43, 251–276.

Besson, J., Cailletaud, G., Chaboche, J.L., Forest, S., 2009. Non-linear mechanics of materials. volume 167. Springer Science & Business Media.

Besson, J., Foerch, R., 1998. Object-oriented programming applied to the finite element method part I. general concepts. Revue Européenne des Eléments Finis 7, 535–566.

Borg, U., Niordson, C.F., Kysar, J.W., 2008a. Size effects on void growth in single crystals with distributed voids. International Journal of Plasticity 24, 688–701.

Borg, U., Niordson, C.F., Kysar, J.W., 2008b. Size effects on void growth in single crystals with distributed voids. International Journal of Plasticity 24, 688–701.

Brepols, T., Wulfinghoff, S., Reese, S., 2017. Gradient-extended two-surface damage-plasticity: Micromorphic formulation and numerical aspects. International Journal of Plasticity 97, 64 – 106.

Busso, E.P., Cailletaud, G., 2005. On the selection of active slip systems in crystal plasticity. International Journal of Plasticity 21, 2212–2231.

Cailletaud, G., Forest, S., Jeulin, D., Feyel, F., Galliet, I., Mounoury, V., Quilici, S., 2003. Some elements of microstructural mechanics. Computational Materials Science 27, 351–374.

Cockburn, B., Karniadakis, G.E., Shu, C.W., 2012. Discontinuous Galerkin methods: theory, computation and applications. volume 11. Springer Science & Business Media.

Cordero, N., Forest, S., Busso, E., Berbenni, S., Cherkaoui, M., 2012a. Grain size effects on plastic strain and dislocation density tensor fields in metal polycrystals. Computational Materials Science 52, 7 – 13.

Cordero, N., Gaubert, A., Forest, S., Busso, E.P., Gallerneau, F., Kruch, S., 2010. Size effects in generalised continuum crystal plasticity for two-phase laminates. Journal of the Mechanics and Physics of Solids 58, 1963–1994.

Cordero, N.M., Forest, S., Busso, E.P., 2012b. Generalised continuum modelling of grain size effects in polycrystals. Comptes Rendus Mécanique 340, 261–274.

Erdle, H., Böhlke, T., 2017. A gradient crystal plasticity theory for large deformations with a discontinuous accumulated plastic slip. Computational Mechanics 60, 923–942.

Eringen, A., Suhubi, E., 1964. Nonlinear theory of simple microelastic solids. Int. J. Engng Sci. 2, 189–203, 389–404.

Farooq, H., Cailletaud, G., Forest, S., Ryckelynck, D., 2020. Crystal plasticity modeling of the cyclic behavior of polycrystalline aggregates under non-symmetric uniaxial loading: Global and local analyses. International Journal of Plasticity 126, 102619.

Fleck, N., Hutchinson, J., 1997. Strain gradient plasticity. Advances in Applied Mechanics 33, 296–361.

Forest, S., 1998. Modeling slip, kink and shear banding in classical and generalized single crystal plasticity. Acta Materialia 46, 3265–3281.

Forest, S., 2009. Micromorphic approach for gradient elasticity, viscoplasticity, and damage. Journal of Engineering Mechanics 135, 117–131.

Forest, S., 2016. Nonlinear regularisation operators as derived from the micromorphic approach to gradient elasticity, viscoplasticity and damage. Proc. R. Soc. A 472, 20150755. doi:10.1098/rspa.2015.0755.

Forest, S., Bertram, A., 2011. Formulations of strain gradient plasticity, in: Mechanics of Generalized Continua. Springer, pp. 137–149.

Forest, S., Olschewski, J., Ziebs, J., Kühn, H.J., Meersmann, J., Frenz, H., 1996. The elastic/plastic deformation behaviour of various oriented SC16 single crystals under combined tension/torsion fatigue loading, in: Lütjering, G., Nowack, H. (Eds.), Sixth International Fatigue Congress, Pergamon. pp. 1087–1092.

Forest, S., Rubin, M., 2016. A rate-independent crystal plasticity model with a smooth elastic–plastic transition and no slip indeterminacy. European Journal of Mechanics-A/Solids 55, 278–288.

Fortin, M., Glowinski, R., 1983. Chapter III on decomposition-coordination methods using an augmented lagrangian, in: Studies in Mathematics and Its Applications. Elsevier. volume 15, pp. 97–146.

Gao, H., Huang, Y., 2001. Taylor-based nonlocal theory of plasticity. International Journal of Solids and Structures 38, 2615 – 2637.

Greer, J.R., Oliver, W.C., Nix, W.D., 2005. Size dependence of mechanical properties of gold at the micron scale in the absence of strain gradients. Acta Materialia 53, 1821 – 1830.

Guo, S., He, Y., Lei, J., Li, Z., Liu, D., 2017. Individual strain gradient effect on torsional strength of electropolished microscale copper wires. Scripta Materialia 130, 124 – 127.

Gurtin, M.E., 2000. On the plasticity of single crystals: free energy, microforces, plastic-strain gradients. Journal of the Mechanics and Physics of Solids 48, 989–1036.

Gurtin, M.E., 2002. A gradient theory of single-crystal viscoplasticity that accounts for geometrically necessary dislocations. Journal of the Mechanics and Physics of Solids 50, 5–32.

Gurtin, M.E., Anand, L., 2009. Thermodynamics applied to gradient theories involving the accumulated plastic strain: the theories of Aifantis and Fleck and Hutchinson and their generalization. Journal of the Mechanics and Physics of Solids 57, 405–421.

Haque, M., Saif, M., 2003. Strain gradient effect in nanoscale thin films. Acta Materialia 51, 3053 – 3061.

Hori, M., Nemat-Nasser, S., 1988a. Dynamic response of crystalline solids with microcavities. Journal of applied physics 64, 856–863.

Hori, M., Nemat-Nasser, S., 1988b. Mechanics of void growth and void collapse in crystals. Mechanics of Materials 7, 1–13.

Hughes, T.J., Scovazzi, G., Bochev, P.B., Buffa, A., 2006. A multiscale discontinuous galerkin method with the computational structure of a continuous galerkin method. Computer Methods in Applied Mechanics and Engineering 195, 2761–2787.

Hussein, M., Borg, U., Niordson, C.F., Deshpande, V., 2008. Plasticity size effects in voided crystals. Journal of the Mechanics and Physics of Solids 56, 114–131.

Kaiser, T., Menzel, A., 2019a. A dislocation density tensor-based crystal plasticity framework. Journal of the Mechanics and Physics of Solids 131, 276 – 302.

Kaiser, T., Menzel, A., 2019b. An incompatibility tensor-based gradient plasticity formulation-Theory and numerics. Computer Methods in Applied Mechanics and Engineering 345, 671 – 700.

Kocks, U., Mecking, H., 2003. Physics and phenomenology of strain hardening: the FCC case. Progress in Materials Science 48, 171 – 273.

Koplik, J., Needleman, A., 1988. Void growth and coalescence in porous plastic solids. International Journal of Solids and Structures 24, 835–853.

Kubin, L., Devincre, B., Hoc, T., 2008. Modeling dislocation storage rates and mean free paths in face-centered cubic crystals. Acta materialia 56, 6040–6049.

Lewandowski, M., Stupkiewicz, S., 2018. Size effects in wedge indentation predicted by a gradient-enhanced crystal-plasticity model. International Journal of Plasticity 109, 54–78.

Lindroos, M., Laukkanen, A., Andersson, T., Vaara, J., Mäntylä, A., Frondelius, T., 2019. Micromechanical modeling of short crack nucleation and growth in high cycle fatigue of martensitic microstructures. Computational Materials Science 170, 109185.

Ling, C., 2017. Modeling the intragranular ductile fracture of irradiated steels. Effects of crystal anisotropy and strain gradient. Theses. PSL Research University. URL: https://pastel.archives-ouvertes.fr/tel-01699226.

Ling, C., Besson, J., Forest, S., Tanguy, B., Latourte, F., Bosso, E., 2016. An elastoviscoplastic model for porous single crystals at finite strains and its assessment based on unit cell simulations. International Journal of Plasticity 84, 58–87.

Ling, C., Forest, S., Besson, J., Tanguy, B., Latourte, F., 2018. A reduced micromorphic single crystal plasticity model at finite deformations. Application to strain localization and void growth in ductile metals. International Journal of Solids and Structures 134, 43–69.

Liu, D., He, Y., Tang, X., Ding, H., Hu, P., Cao, P., 2012. Size effects in the torsion of microscale copper wires: Experiment and analysis. Scripta Materialia 66, 406 – 409.

Liu, Y., Ngan, A., 2001. Depth dependence of hardness in copper single crystals measured by nanoindentation. Scripta Materialia 44, 237–241.

Needleman, A., 1988. Material rate dependence and mesh sensitivity in localization problems. Computer Methods in Applied Mechanics and Engineering 67, 69 – 85.

Neff, P., Ghiba, I., Madeo, A., Placidi, L., Rosi, G., 2014. A unifying perspective: the relaxed linear micromorphic continuum. Continuum Mechanics and Thermodynamics 26, 639–681.

Nellemann, C., Niordson, C., Nielsen, K., 2017. An incremental flow theory for crystal plasticity incorporating strain gradient effects. International Journal of Solids and Structures 110-111, 239 – 250.

Nellemann, C., Niordson, C., Nielsen, K., 2018. Hardening and strengthening behavior in rate-independent strain gradient crystal plasticity. European Journal of Mechanics - A/Solids 67, 157 – 168.

Niordson, C.F., Kysar, J.W., 2014. Computational strain gradient crystal plasticity. Journal of the Mechanics and Physics of Solids 62, 31–47.

Nix, W.D., Gao, H., 1998. Indentation size effects in crystalline materials: A law for strain gradient plasticity. Journal of the Mechanics and Physics of Solids 46, 411 – 425.

Nouailhas, D., Cailletaud, G., 1995. Tension-torsion behavior of single-crystal superalloys - Experiment and finite-element analysis. Int. J. Plasticity 8, 451–470.

Panteghini, A., Bardella, L., 2016. On the finite element implementation of higher-order gradient plasticity, with focus on theories based on plastic distortion incompatibility. Computer Methods in Applied Mechanics and Engineering 310, 840–865.

Peerlings, R., de Borst, R., Brekelmans, W., Geers, M., 2002. Localisation issues in local and nonlocal continuum approaches to fracture. European Journal of Mechanics - A/Solids 21, 175 – 189.

Petryk, H., Stupkiewicz, S., 2016. A minimal gradient-enhancement of the classical continuum theory of crystal plasticity. part i: The hardening law. Archives of Mechanics 68, 459–485.

Quilici, S., Forest, S., Cailletaud, G., 1998. On size effects in torsion of multi- and polycrystalline specimens. Journal de Physique IV 8, Pr8–325–332.

Roters, F., Eisenlohr, P., Hantcherli, L., Tjahjanto, D., Bieler, T., Raabe, D., 2010. Overview of constitutive laws, kinematics, homogenization and multiscale methods in crystal plasticity finite-element modeling: Theory, experiments, applications. Acta Materialia 58, 1152 – 1211.

Ryś, M., Forest, S., Petryk, H., 2020. A micromorphic crystal plasticity model with the gradient-enhanced incremental hardening law. International Journal of Plasticity , 102655.

Scherer, J., Besson, J., Forest, S., Hure, J., Tanguy, B., 2019. Strain gradient crystal plasticity with evolving length scale: Application to voided irradiated materials. European Journal of Mechanics-A/Solids 77, 103768.

Selvarajou, B., Joshi, S.P., Benzerga, A.A., 2019. Void growth and coalescence in hexagonal close packed crystals. Journal of the Mechanics and Physics of Solids 125, 198–224.

Shu, J., 1998. Scale–dependent deformation of porous single crystals. International Journal of Plasticity 14, 1085–1107.

Stölken, J., Evans, A., 1998. A microbend test method for measuring the plasticity length scale. Acta Materialia 46, 5109 – 5115.

Uchic, M., Dimiduk, D., Florando, J., Nix, W., 2004. Sample dimensions influence strength and crystal plasticity. Science (New York, N.Y.) 305, 986–9.

Vignjevic, R., Djordjevic, N., Vuyst, T.D., Gemkow, S., 2018. Modelling of strain softening materials based on equivalent damage force. Computer Methods in Applied Mechanics and Engineering 335, 52 – 68.

Voyiadjis, G.Z., Al-Rub, R.K.A., 2005. Gradient plasticity theory with a variable length scale parameter. International Journal of Solids and Structures 42, 3998 – 4029.

Wulfinghoff, S., Bayerschen, E., Böhlke, T., 2013. A gradient plasticity grain boundary yield theory. International Journal of Plasticity 51, 33–46.

Wulfinghoff, S., Böhlke, T., 2012. Equivalent plastic strain gradient enhancement of single crystal plasticity: theory and numerics. Proc. R. Soc. A 468, 2682–2703.

Yalcinkaya, T., Brekelmans, W., Geers, M., 2012. Non-convex rate dependent strain gradient crystal plasticity and deformation patterning. International Journal of Solids and Structures 49, 2625–2636.

Z–set package, 2020. Non-linear material & structure analysis suite, www.zset-software.com.

Zhang, Y., Lorentz, E., Besson, J., 2018. Ductile damage modelling with locking-free regularised GTN model. International Journal for Numerical Methods in Engineering 113, 1871–1903.

Zhao, K., Chen, C., Shen, Y., Lu, T., 2009. Molecular dynamics study on the nano-void growth in face-centered cubic single crystal copper. Computational Materials Science 46, 749–754.